Study on spin-orbit torque effects in metallic bi-layer and single-layer systems

Motomi Aoki

Study on spin-orbit torque effects in metallic bi-layer and single-layer systems

A dissertation submitted to

Graduate School of Engineering

KYOTO UNIVERSITY

BY

Motomi Aoki

September 2023

Abstract of the dissertation

Study on spin-orbit torque effects in metallic bi-layer and single-layer systems

by

Motomi Aoki

Abstract

Computer architecture has been developed following Moore's law. However, it is reaching limitation and innovation in computer technology is required for persistent development. "Spintronics" has a great possibility as a candidate of "beyond Moore" technology. Electron possesses two degrees of freedom, "charge" and "spin". Whereas electronics uses only the charge degree of freedom, spintronics additionally uses the spin degree of freedom, expanding possibility and flexibility in device application. Given that the spin is a source of magnet, "spin current", enables us to manipulate magnetization of the magnetic material by being injected into the magnet, which is called the spin-orbit torque (SOT). SOT can be used for the writing process of the magnetoresistive random access memory (MRAM), where magnetization is used as a nonvolatile memory carrier. Since the MRAM utilizing spintronics technology is expected to possess a plenty of advantages such as nonvolatility, low-power consumption, and high durability, writing process by spin-current injection has been investigated intensively.

Strategy for improving efficiency of the writing process of the MRAM is to look for a novel material in which spin current is efficiently converted from the electric current. In this sense, for example, topological insulators have recorded gigantic charge-to-spin conversion efficiency. However, the record is reaching maximum and study from the viewpoint other than simple material search is needed. In addition, most SOT research use indirect method for estimating the SOT efficiency but not detecting the SOT-induced magnetization switching directly because the latter needs complicated fabrication procedure. It is known that the SOT efficiency estimated by indirect methods does not always have consistency between the current density required for SOT-induced switching. Therefore, development of the method for detecting SOT switching without complicated fabrication process is needed for agile and reliable estimation of the SOT switching efficiency.

In this study, first, the author developed a way for detecting SOT-induced magnetization switching without any complicated fabrication process. At the same time, the author found out a novel way for estimating the SOT efficiency indirectly. Then, the author carried out experiments aiming at improvement of efficiency in SOT switching by manipulating injected spin orientation and utilizing self-induced SOT (SI-SOT) in the ferromagnetic material (FM). Finally, the author investigated the anisotropic SI-SOT in a Weyl ferromagnet, Co_2MnGa (CMG).

In Chap. 1, basis of the spintronics is introduced. Then, the mechanism of the MRAM using the spin current

in the writing process and typical examples of widely used methods for estimating SOT are explained.

In Chap. 2, the author explains about development of the method for detecting SOT-induced magnetization switching. So far, to detect SOT magnetization switching of a FM with in-plane easy axis, researchers have generally used the tunnel magnetoresistance effect by fabricating magnetic tunnel junction (MTJ). Since fabricating MTJ requires difficult fabrication processes, this method cannot be used flexibly. On the other hand, the author focused on the rectification signal under irradiation of microwave in FM/nonmagnetic material (NM) bilayer structures. Using the significant enhancement of the hysteresis in the rectification signal around zero magnetic field due to the oscillation of the domain wall structure, magnetization switching of permalloy induced by the SOT originating from the spin Hall effect (SHE) in Pt was successfully detected.

In Chap. 3, the author focuses on the background (BG) signal coexisting with the rectification signal investigated in Chap. 2. The BG signal does not depend on the frequency nor magnetic-field amplitude. On the other hand, it was found that the polarity of the background signal changes depending on the sign of the spin Hall angle (SHA) of the NM layer. From the magnetic field angle, temperature, frequency, and current-amplitude dependences, the author concluded that the BG signal is induced by the spin-dependent unidirectional spin Hall magnetoresistance, the origin of which is the spin accumulation in the FM layer induced by the SHE in the NM layer and spin-dependent electron mobility. Using the numerical expression of the spin-dependent unidirectional spin Hall magnetoresistance, values of the SHA of Pt and Ta were estimated to be 0.052 and -0.084, respectively, both of which are similar to those estimated in previous research.

In Chap. 4, the author demonstrates SOT magnetization switching using two current pulses. A rectangular permalloy electrode was fabricated onto the Pt electrode shaped as a cross bar. By injecting two pulse currents in-plane along and perpendicular to the magnetization direction, respectively, polarization of spin injected into the permalloy was controlled. As a result, switching speed and power consumption in the writing process were enhanced by more than one order of magnitude compared to the conventional SOT switching using only one pulse current. In addition, the author demonstrated the analog operation of the magnetization, i.e., magnetization direction was controlled along any direction by manipulating sign and magnitude of two current pulses, which can be used for neuromorphic computing.

In Chap. 5, the author investigates current induced torque acting on the magnetization of the permalloy layer connected with the asymmetric electrodes. Since the inversion symmetry and current induced torque are strongly correlated with each other, in-plane asymmetry of the electric-current distribution induced by the asymmetric electrodes is expected to generate current-induced out-of-plane torque and enable field-free magnetization switching of a FM with out-of-plane magnetic anisotropy. From the spin-torque ferromagnetic resonance measurement of the asymmetric permalloy electrode, the author successfully observed current-induced out-of-plane torque. The author concluded that the current-indued out-of-plane torque observed in this study originates from the out-of-plane Oersted field induced by the nonuniform electric current and resulting

inductive effect because the out-of-plane torque was strongly modulated by changing the frequency of the microwave used in the spin-torque ferromagnetic resonance method. The author also demonstrated field-free switching of the magnetization of a FM with out-of-plane magnetic anisotropy by using micromagnetic simulation.

In Chap. 6, the author investigates the SI-SOT in a NM/FM bilayer structure, where the SHE of the FM gives torque on the magnetization of the FM itself. In a NM/FM bilayer structure, it has been assumed that the torque acting on magnetization is mainly caused by the charge-to-spin conversion in the NM layer. However, the author found that the SI-SOT is comparable to the conventional SOT originating from the NM layer, giving a new strategy for realization of efficient SOT generation in viewpoint of combination of the SOT and the SI-SOT. Moreover, the author claims that the SI-SOT becomes dominant especially when the conductivity of the NM layer is low based on spin-diffusion model. Since there has been a trend that a high resistive material shows large SHA, the author proposes that revisiting of the SOT research especially using high-resistive material might be needed with consideration of the SI-SOT.

In Chap. 7, the author investigates the SI-SOT in a Weyl ferromagnet, CMG, in which large SHE has been reported in previous works. Surprisingly, it was found that CMG shows large SI-SOT comparable to a heavy metal/FM bilayer structure even without any adjacent metal layer. Moreover, sign and magnitude of the SI-SOT were strongly dependent on the applied-current direction with respect to the crystal axis. The author measured the SI-SOT of CMG layers with changing thickness and capping material, as well as carried out structural analysis and investigated theoretically with help from theorists. As a result, the author concluded that the large SI-SOT and its significant anisotropy originate from the anisotropic distribution of the Weyl points and their strong modulation by external strain.

In Chap. 8, the author summarizes the study and gives outlook of the research.

Contents

Chapter 1. Introduction ---------- 1
1.1 Abstract ---------- 1
1.2 Spin current ---------- 1
1.3 Spin-orbit interaction ---------- 2
1.4 Charge-to-spin conversion ---------- 2
1.5 Spin torque ---------- 3
1.6 Magnetization dynamics ---------- 4
1.7 Magnetoresistive random access memory ---------- 5
1.8 How to measure spin-orbit torque ---------- 6
1.8.1 Current-induced magnetization switching ---------- 6
1.8.2 Spin-torque ferromagnetic resonance ---------- 6
1.8.3 Second harmonic Hall measurement ---------- 8
1.8.4 Detection of spin-orbit effective field ---------- 9
1.9 Research purpose and outline of this dissertation ---------- 9
Chapter 2. Detection of spin-orbit torque magnetization switching by low-frequency spin-torque ferromagnetic resonance ---------- 11
2.1 Abstract ---------- 11
2.2 Introduction and research purpose ---------- 12
2.3 Experimental setup ---------- 13
2.3.1 Sample fabrication ---------- 13
2.3.2 Measurement setup ---------- 13
2.4 Observation of the low-frequency spin-torque ferromagnetic resonance in Pt/permalloy bilayer system ---------- 14
2.4.1 Material characterization ---------- 14
2.4.2 Frequency dependence of the non-resonant spin-rectification effect ---------- 14
2.5 Analyzation of the low-frequency spin-torque ferromagnetic resonance ---------- 15
2.5.1 Low-frequency spin-torque ferromagnetic resonance in Pt/Co, Pt/Fe, and Pt/permalloy bilayers ---------- 15
2.5.2 Relationship between anisotropic magnetoresistance ---------- 16
2.5.3 Micromagnetic simulation ---------- 18
2.6 Detection of the spin-orbit torque magnetization switching ---------- 19
2.6.1 Experimental procedure ---------- 19
2.6.2 Microwave frequency and pulse width dependence ---------- 19
2.6.3 Downsizing of the ferromagnetic electrode ---------- 21
2.7 Summary ---------- 21
Chapter 3. Coexistence of the low-frequency spin-torque ferromagnetic resonance and unidirectional spin Hall magnetoresistance ---------- 23
3.1 Abstract ---------- 23
3.2 Introduction and research purpose ---------- 24
3.2.1 Background signal ---------- 24
3.2.2 Unidirectional spin Hall magnetoresistance ---------- 24
3.3 Experimental setup ---------- 26

3.3.1 Sample fabrication -- 26
3.3.2 Measurement setup--- 26
3.4 Investigation on the background signal--- 27
3.4.1 Microwave frequency dependence -- 27
3.4.2 Frequency, current, temperature, and magnetic-field angle dependences ---- 27
3.4.3 Contribution from the anomalous Nernst effect---------------------------------- 28
3.5 Utilization of the background signal -- 30
3.5.1 Estimation of the spin Hall angle --- 30
3.5.2 Detection of the spin-orbit torque magnetization switching--------------------- 30
3.6 Summary --- 31
Chapter 4. Spin-orbit torque magnetization switching using two current pulses 32
4.1 Abstract --- 32
4.2 Introduction and research purpose-- 33
4.2.1 In-plane and out-of-plane magnetoresistive random access memories--------- 33
4.2.2 Mechanism of two-pulse switching --- 33
4.3 Experimental setup --- 34
4.3.1 Sample fabrication -- 34
4.3.2 Measurement setup-- 34
4.4 Demonstration of two-pulse magnetization switching --------------------------------- 34
4.4.1 Interval and assist pulse dependences -- 34
4.4.2 Assist pulse width dependence -- 35
4.4.3 Comparison with one-pulse method --- 36
4.4.4 Micromagnetic simulation --- 37
4.5 Control of magnetization utilizing two-pulse method--------------------------------- 37
4.5.1 Analog rotation of magnetization--- 37
4.6 Summary --- 39
Chapter 5. Current-induced out-of-plane torque in a single permalloy layer controlled by electrode structure-- 40
5.1 Abstract --- 40
5.2 Introduction and research purpose-- 41
5.2.1 Symmetry and spin-orbit torque --- 41
5.2.2 Generation of out-of-plane torque-- 41
5.3 Experimental setup --- 41
5.3.1 Sample fabrication -- 41
5.3.2 Measurement setup-- 42
5.4 Out-of-plane torque induced by asymmetric electrode structure ------------------- 42
5.4.1 Estimation of in-plane and out-of-plane torques ------------------------------- 42
5.4.2 Controlling out-of-plane torques by electrode structure------------------------ 43
5.4.3 Origin of the out-of-plane torques-- 44
5.5 Application to the magnetoresistive random access memory ----------------------- 45
5.6 Summary --- 47
Chapter 6. Self-induced spin-orbit torque in nonmagnetic material/ferromagnetic material bilayer structures -- 48
6.1 Abstract --- 48

6.2 Introduction and research purpose ---- 49
6.2.1 Revisiting of the spin-orbit torque ---- 49
6.2.2 Mechanism of the self-induced spin-orbit torque ---- 49
6.3 Experimental setup ---- 49
6.3.1 Sample fabrication ---- 49
6.3.2 Measurement setup ---- 49
6.4 Sign reversal of the net of spin-orbit torque ---- 50
6.4.1 Spin-torque ferromagnetic resonance ---- 50
6.4.2 Control experiments by the second harmonic Hall method ---- 51
6.4.3 Control experiments using different materials ---- 52
6.5 Analysis based on the spin-diffusion model ---- 53
6.6 Influence on the estimation of the spin Hall angle ---- 55
6.7 Summary ---- 56
Chapter 7. Observation of giant self-induced spin-orbit torque and its anisotropy in $L2_1$ ordered Co_2MnGa single layer ---- 57
7.1 Abstract ---- 57
7.2 Introduction and research purpose ---- 58
7.2.1 Weyl ferromagnet Co_2MnGa ---- 58
7.2.2 Anisotropy in the spin Hall effect ---- 58
7.2.3 Spin-orbit torque in a single ferromagnet layer ---- 59
7.3 Experimental setup ---- 59
7.3.1 Sample fabrication ---- 59
7.3.2 Measurement setup ---- 59
7.4 Material characterization ---- 60
7.5 Spin-orbit torque in Co_2MnGa ---- 60
7.5.1 Anisotropy of the spin-orbit torque ---- 60
7.5.2 Capping material and thickness dependences ---- 61
7.6 Self-induced spin-orbit torque generated by nonuniform lattice distortion ---- 62
7.6.1 Verification of lattice distortion ---- 62
7.6.2 Calculation of spin diffusion equation ---- 63
7.7 First principles calculations ---- 64
7.7.1 Band structure and spin Hall conductivity ---- 64
7.7.2 Consistency with previous works ---- 65
7.7.3 Comparison with spin-orbit torque anisotropy of other materials ---- 66
7.8 Summary ---- 66
Chapter 8. Conclusion ---- 67
Appendix ---- 69
A. Details of the simulation of MuMax3 (Section 2.5.3) ---- 69
B. Frequency dependent power loss (Section 3.4.2) ---- 69
C. Estimation of inductive effect with different frequencies (Section 5.5) ---- 70
D. Influence of the spin pumping and anomalous Nernst effect (Section 6.4.1) ---- 70
E. Measurement of the shift of the magnetoresistance curve (Section 6.4.2) ---- 72
F. Calculation using spin-diffusion equation (Section 6.5) ---- 73
References ---- 75

Publication list--- 80
List of Abbreviations--- 84
Acknowledgement --- 86

Chapter 1. Introduction

1.1 Abstract

Since early 20th century, electronics, in which a flow of the charge of electron is utilized for memorizing, transporting, and reading information and/or energy, has been contributing innovation of industry. Especially, progress of computer architecture is remarkable. The fact that the performance of a current laptop far exceeds the combined performance of all computer systems used on the Apollo 11 lunar mission in 1969 is one of the examples of magnificent progress of electronics these days. Such development of the performance of computers has been following Moore's law [1], i.e., density of circuits becomes double per 24 months. However, sustainability of Moore's law is reaching physical limitation and innovation of computer architecture is required. One of the candidates for overcoming the Moore's law is "spintronics", in which spin degree of electron, classically explained by the rotation of the electron, is utilized in addition to the charge degree of freedom. In the following, the author introduces the basis of the spintronics and application of it for the novel device architecture.

1.2 Spin current

Electron possesses two degrees of freedom, charge and spin. The charge degree of freedom has been utilized in electronics as an electric current, where only charge is transported because orientation of spin is random. If electrons carrying electric current are spin-polarized along a specific orientation, not only charge but also spin can be transported. This kind of flow of electron is called "spin-polarized current", a typical example of which is an electric current in a ferromagnetic material (FM). Moreover, if there is a flow of electron where up- and down-spin electrons move opposite direction to each other, spin degree of freedom is transported without flow of charge. This is called "(pure) spin current" (Fig. 1-1). In the spin current, energy never dissipate because time reversal inversion symmetry is preserved. Therefore, spin current has been attracted great attention as a candidate of a next-generation information carrier.

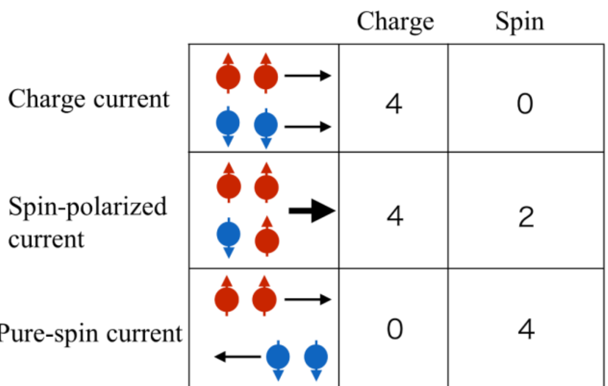

FIG. 1-1. Schematics of charge, spin-polarized, and pure-spin currents.

1.3 Spin-orbit interaction

Electron's motion and spin polarization are correlated by the spin-orbit interaction (SOI). Although the SOI is explained by the theory of relativity, classical explanation is given by the model where an electron is revolving around an atom. When a free electron is revolving anti-clockwise around an atom as shown in Fig. 1-2(a), a view from the electron is that the atom is revolving anti-clockwise around the electron as shown in Fig. 1-2(b). Since the atom possesses a positive charge, revolution of an atom corresponds to a circular electric current. As a result, electron feels virtual magnetic field due to this circular magnetic field $\boldsymbol{H}$, which is calculated by Biot-Savart law as,

$$\boldsymbol{H} = \frac{Ze(\boldsymbol{r} \times \dot{\boldsymbol{r}})}{r^3}, \tag{1-1}$$

where Z is the atomic number and e is the elementary charge. Magnetostatic energy, ε_{m}, between electron's spin, $\boldsymbol{\sigma}$, and $\boldsymbol{H}$ is given by [2],

$$\varepsilon_m = -2\boldsymbol{\sigma}\mu_B \cdot \boldsymbol{H} = \frac{e^2\hbar^2\mu_0}{m_e^2}\frac{Z}{r^3}\boldsymbol{l}\cdot\boldsymbol{\sigma} \tag{1-2}$$

where μ_{B} is Bohr magnetron, $\hbar$ is Dirac constant, μ_0 is vacuum permeability, $\boldsymbol{l}$ is orbital angular momentum, and $m_e = \hbar\boldsymbol{l}/(\boldsymbol{r} \times \dot{\boldsymbol{r}})$. Note that the CGS unit is used in Eq. (1-2). Given that ε_{m} is proportional to $\boldsymbol{l}\cdot\boldsymbol{\sigma}$, up- and down-spin prefers $\boldsymbol{l}$ with opposite signs to each other to minimize ε_{m}, called the SOI.

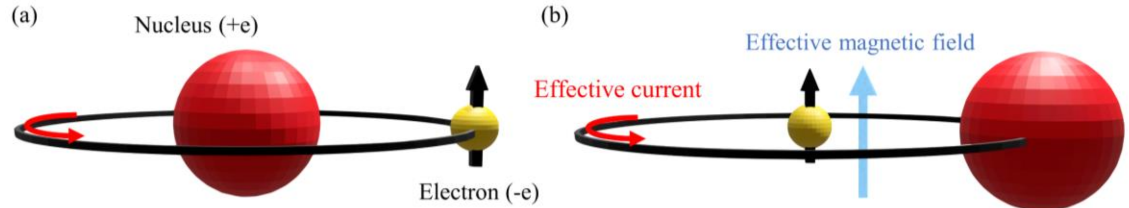

FIG. 1-2. (a) Schematics of an electron revolving around a nucleus and (b) a nucleus revolving around an electron.

1.4 Charge-to-spin conversion

When an external magnetic field, $\boldsymbol{H}_{\mathrm{ext}}$, is applied perpendicularly to a film of a nonmagnetic material (NM), electric current, $\boldsymbol{J}_{\mathrm{c}}$, flowing in-plane (IP) generates transverse electric field, $\boldsymbol{E}$, due to the Lorentz force, called

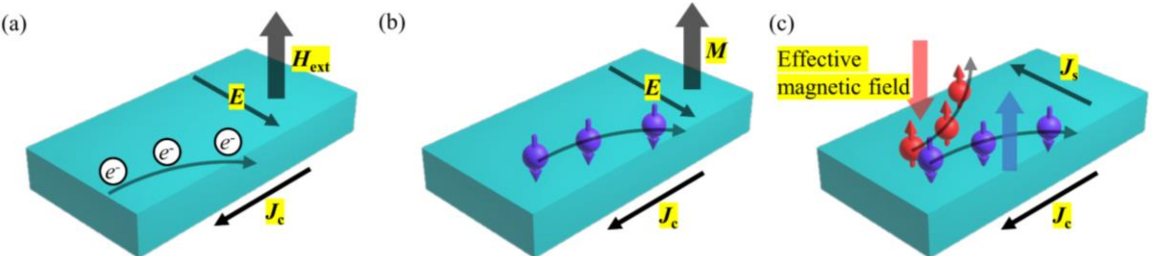

FIG. 1-3. Schematics of (a) the ordinary Hall effect, (b) the anomalous Hall effect, and (c) the spin Hall effect.

Hall effect [Fig. 1-3(a)]. Similarly, in a film of a FM with magnetization, $\boldsymbol{M}$, along out-of-plane (OOP) direction, $\boldsymbol{J}_\mathbf{c}$ along IP generates $\boldsymbol{E}$, called the anomalous Hall effect (AHE) [3] [Fig. 1-3(b)]. AHE seems to be just a counterpart of the Hall effect by replacing $\boldsymbol{H}_\mathbf{ext}$ to $\boldsymbol{M}$, however, origin of the AHE is known to be the SOI but not the Lorentz force. As mentioned in section 1.3, up- and down-spins are moved to opposite direction to each other owing to the SOI. Therefore, transverse current of majority spins does not cancel that of minority spin in a FM, resulting in $\boldsymbol{E}$ along transverse direction due to transverse spin-polarized current. On the other hand, if we consider the SOI in a NM, transverse charge current is completely canceled out because the number of up- and down- spin are the same. As a result, pure spin current, $\boldsymbol{J}_\mathbf{s}$, is generated along transverse direction to $\boldsymbol{J}_\mathbf{c}$, called the spin Hall effect (SHE) [4]. Here, magnitude of the SHE is defined as the spin Hall angle (SHA), $\theta_{SH} = J_s / J_c$.

In addition, there is a different type of the charge-to-spin conversion at the interface between two different materials as shown in Fig. 1-4. There is an internal electric field, $\boldsymbol{E}$, at the interface due to finite difference in work function. In other words, electrons are much accumulated in one layer compared to the other. If an electron moves forward at the interface with a momentum of $\boldsymbol{p}$, accumulated electrons move backward from the viewpoint of the moving electron, corresponding to a virtual electric current. The moving electron feels effective magnetic field along $\boldsymbol{E} \times \boldsymbol{p}$ due to this virtual electric current, resulting in spin polarization. This is called the Rashba-Edelstein effect (REE) [5].

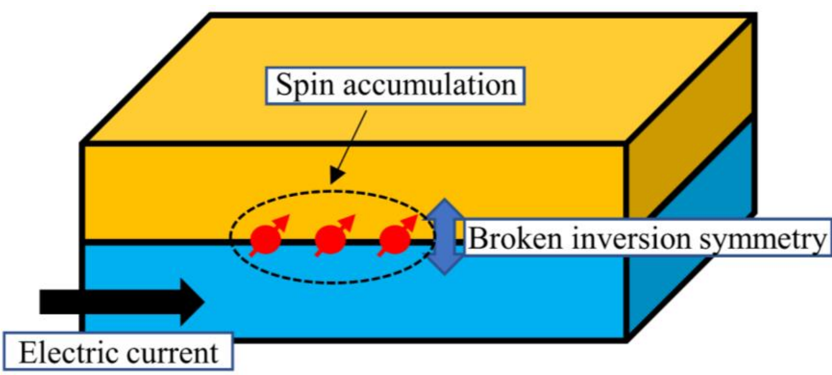

FIG. 1-4. A schematic of Rashba-Edelstein effect.

1.5 Spin torque

When a conduction spin that carries spin current is scattered by a localized spin, both spins are tilted along opposite direction to each other due to exchange of angular momentum (Fig. 1-5). In a different viewpoint, spin current changes angular momentum of the localized spin, called spin torque [6]. There are two types of spin

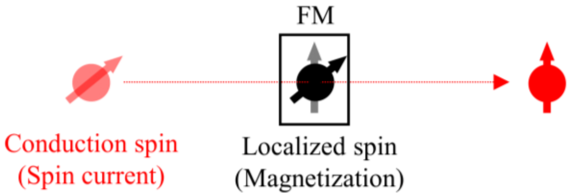

FIG. 1-5. A schematic of the spin torque.

torque as shown in Fig. 1-6, damping-like (DL) torque expressed as $\boldsymbol{\tau}_{\mathrm{DL}} \sim \boldsymbol{m} \times (\boldsymbol{m} \times \boldsymbol{\sigma})$ that tilts $\boldsymbol{m}$ to the direction of the magnetic momentum of the injected spin, and field-like (FL) torque expressed as $\boldsymbol{\tau}_{\mathrm{FL}} \sim \boldsymbol{m} \times \boldsymbol{\sigma}$ that induces precession of $\boldsymbol{m}$ around $\boldsymbol{\sigma}$, where $\boldsymbol{m}$ and $\boldsymbol{\sigma}$ are vector of localized magnetic momentum and injected spin angular momentum, respectively. When a NM with a large charge-to-spin conversion is attached to a FM, spin current is injected into the FM by applying electric current in the NM layer as shown in Fig. 1-6. In this case, spin torque is given to the magnetization of the FM layer, which is called the spin-orbit torque (SOT) [7,8].

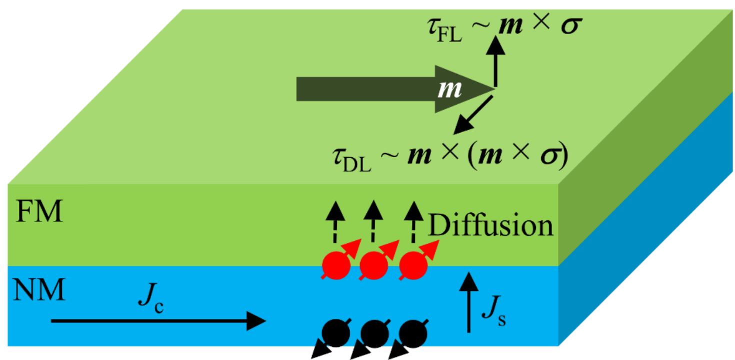

FIG. 1-6. A schematic of the spin-orbit torque in a NM/FM bilayer structure.

1.6 Magnetization dynamics

Dynamics of magnetization induced by an AC magnetic field and/or spin torque is described by the Landau-Lifshitz-Gilbert (LLG) equation as [9,10],

$$\frac{\mathrm{d}\boldsymbol{m}}{\mathrm{d}t} = -\gamma \boldsymbol{m} \times \boldsymbol{H} - \alpha \boldsymbol{m} \times \frac{\mathrm{d}\boldsymbol{m}}{\mathrm{d}t} + \tau_{\mathrm{DL}} \boldsymbol{m} \times (\boldsymbol{m} \times \boldsymbol{\sigma}) + \tau_{\mathrm{FL}} \boldsymbol{m} \times \boldsymbol{\sigma}, \tag{1-3}$$

where γ is gyromagnetic ratio, $\boldsymbol{H}$ is the magnetic field acting on the magnetization, and α is Gilbert damping coefficient. The first term in Eq. (1-3) corresponds to the precession of $\boldsymbol{m}$ with a precession axis along $\boldsymbol{H}$, whereas the second term describes relaxation of the magnetization precession, called magnetization damping. The third and fourth terms describe contribution from the DL and FL torques. Eq. (1-3) indicates that magnetization can be manipulated not only by magnetic field but also by DL and FL torques.

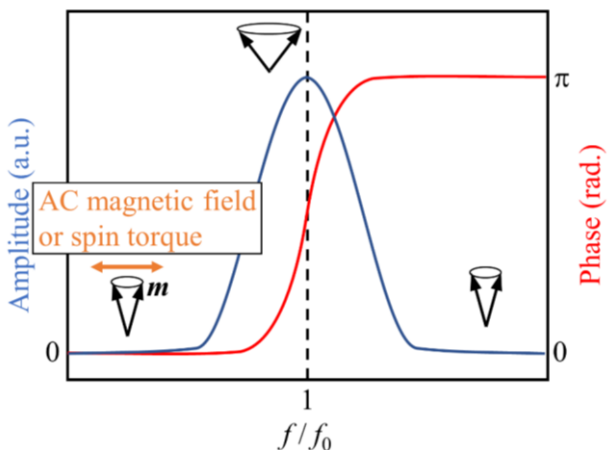

FIG. 1-7. A schematic of the ferromagnetic

When precession of $\boldsymbol{m}$ in the FM is induced by AC magnetic field and/or spin torque with a frequency of f under external DC magnetic field, H_{ext}, precession amplitude is enhanced and phase difference between AC magnetic field or spin torque and magnetization precession rapidly changes from zero to π as shown in Fig. 1-7 when f reaches the resonance frequency, f_0, that satisfies the Kittel's equation [11],

$$f_0 = \frac{\gamma}{2\pi}\sqrt{\left[\mu_0 H_{\text{ext}} + \left(N_x - N_y\right)\mu_0 M_s\right]\left[\mu_0 H_{\text{ext}} + \left(N_z - N_y\right)\mu_0 M_s\right]}, \tag{1-4}$$

where M_s is saturation magnetization. N is demagnetization factor along x, y, and z direction. Here, z is chosen along OOP orientation, and $\boldsymbol{H}_{\text{ext}}$ is pointing along the x-y plane. This phenomenon is called the ferromagnetic resonance (FMR).

1.7 Magnetoresistive random access memory

One of the most attractive devices in spintronics is magnetoresistive random access memory (MRAM) [12]. Here, the author introduces two kinds of MRAM with different writing processes, spin-transfer torque (STT)-MRAM and SOT-MRAM.

STT-MRAM [Fig. 1-8(a)] is composed of a free layer/tunnel layer/pin layer structure that is called magnetic tunnel junction (MTJ). By fixing coercivity of the pin layer to be much higher than that of the free layer, only the free layer becomes writable by external forces. When an electric current for writing, I_{write}, is applied perpendicularly in the MTJ, spin-polarized current is injected from the pin layer to the free layer via tunneling through the tunnel layer. Injected spins give torque on the magnetization of the free layer and reverse the magnetization. Since the resistance of the MTJ changes with respect to the relative orientation of the magnetization in the free layer to that of the pin layer (tunnel magnetoresistance, TMR) [13], magnetization orientation in the free layer can be extracted electrically by injecting a reading current, I_{read}, and correlated to a "bit" of information. Since the STT-MRAM stores information in the magnetization, it has been attracted as a nonvolatile memory device. However, STT-MRAM is less durable because I_{write} needs to flow through the tunnel layer at every writing process, which gradually destroy the tunnel layer and cause degradation.

On the other hand, SOT-MRAM [Figs. 1-8(b) and 1-8(c)] is composed of a MTJ on top of the SOT layer with a material that possesses large charge-to-spin conversion such as a heavy metal. When I_{write} is injected into the SOT layer, spin current is injected into the free layer via the charge-to-spin conversion, giving torque to the magnetization and inducing current-induced magnetization reversal. Magnetization direction in the free layer is read by the TMR in the same manner as the STT-MRAM. Advantage of the SOT-MRAM is that only a small reading current, I_{read}, is required to flow through the tunnel layer. Therefore, writing process is much more energy efficient and the device is much more durable compared to the STT-MRAM. However, SOT-MRAM using a FM with OOP magnetic anisotropy requires assist magnetic field for deterministic magnetization reversal. Although a FM with in-plane (IP) magnetic anisotropy can be switched without assist magnetic field, it requires large power consumption due to longer writing time.

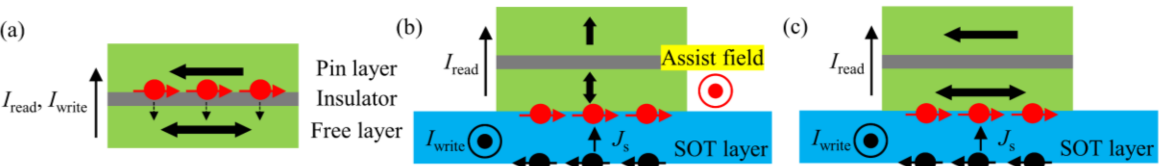

FIG. 1-8. Schematics of (a) the STT-MRAM, (b) the SOT-MRAM with OOP magnet, and (c) the SOT-MRAM with IP magnet.

1.8 How to measure spin-orbit torque

SOT has been investigated intensively aiming at low-power and field-free SOT switching. In this section, the author explains experimental ways for estimating the SOT efficiency, which is the indicator of the torque acting on the magnetization per unit current density.

1.8.1 Current-induced magnetization switching

One of the most direct ways is to detect reversal of the magnetization induced by the SOT. Threshold current density, J_{th}, of SOT switching for an OOP FM is correlated to the DL torque efficiency, ξ_{DL}, as [14],

$$J_{\mathrm{th}} = \frac{e\mu_0 M_{\mathrm{s}} t_{\mathrm{FM}} \left(H_{\mathrm{k(OOP)}} - \sqrt{2}|H_x|\right)}{\hbar \xi_{\mathrm{DL}}}, \tag{1-5}$$

and that for an IP FM as [15],

$$J_{\mathrm{th}} = \frac{\alpha}{\xi_{\mathrm{DL}}} \left(\frac{2e}{\hbar}\right) \left(t_{\mathrm{FM}} H_{\mathrm{k(IP)}} M_{\mathrm{s}}\right), \tag{1-6}$$

where t_{FM} is thickness of the ferromagnet, H_k is uniaxial magnetic anisotropy field along OOP or IP direction, and H_x is assist magnetic field for OOP switching. Note that Eq. (1-6) is written in the CGS unit.

If we fabricate a MTJ on top, magnetization reversal of both the IP and OOP FMs can be detected. However, fabricating MTJ requires growth of single-crystal tunnel barrier with high-quality interface, making investigation of novel materials more difficult [16,17]. Therefore, AHE [18] and magneto-optic Kerr effect microscope (MOKE) [19] are generally used for detecting SOT-induced magnetization reversal of a FM with OOP and IP magnetic anisotropy, respectively.

It has to be noted that the value of ξ_{DL} estimated from the SOT switching is sometimes deviated from the real value because SOT switching is affected by the Oersted field via the electric current in the NM layer and/or domain-wall nucleation in the FM layer [20]. Therefore, multiple methods are frequently used at the same time as detecting SOT switching to obtain a reliable value of the SOT efficiency.

1.8.2 Spin-torque ferromagnetic resonance

Spin-torque ferromagnetic resonance (ST-FMR) is one of the most common ways to estimate the SOT efficiency [21]. In this method, RF electric current, I_{rf}, with a frequency of f is applied to a NM/FM bilayer structure as shown in Fig. 1-9(a). Oersted field, H_{Oe}, and/or SOT excite magnetization oscillation and resulting oscillation of the resistance via anisotropic magnetoresistance (AMR) effect, in which resistance changes depending on the relative angle between electric current and magnetization, θ. As a result, DC voltage, V_{DC}, is observed via bias tee owing to the rectification caused by I_{rf} and oscillating resistance, which is especially enhanced around the FMR condition. When H_{ext} is swept with a fixed f, spectrum of V_{DC} is composed of symmetric and anti-symmetric Lorentzian functions as [21],

$$V_{\mathrm{DC}} = \frac{1}{4}\frac{\mathrm{d}R}{\mathrm{d}\theta} \frac{\gamma I_{\mathrm{rf}} \sin\theta}{2\pi\Gamma\left(\frac{\mathrm{d}f}{\mathrm{d}H_{\mathrm{ext}}}|_{H_{\mathrm{ext}}=H_0}\right)} \times \left(S\frac{\Gamma^2}{\Gamma^2 + (H_{\mathrm{ext}} - H_0)^2} + A\frac{\Gamma(H_{\mathrm{ext}} - H_0)}{\Gamma^2 + (H_{\mathrm{ext}} - H_0)^2}\right), \tag{1-7}$$

where R is resistance of the NM/FM bilayer, Γ is half-width at half-maximum, H_0 is magnetic field that satisfies the FMR condition, S and A are amplitudes of symmetric and anti-symmetric Lorentzian components,

respectively. A typical ST-FMR spectrum is shown in Fig. 1-9(b).

S and A are composed of four and three different θ dependences, respectively, as [22],

$$S = S_0\sin2\theta\cos\theta + S_1\sin2\theta\sin\theta + S_2\sin2\theta + S_3\sin\theta, \tag{1-8}$$

$$A = A_0\sin2\theta\cos\theta + A_1\sin2\theta\sin\theta + A_2\sin2\theta. \tag{1-9}$$

Tables 1-1 and 1-2 show origins of each θ dependence in S and A, respectively. θ dependence of A and S are needed to be measured to extract a specific contribution. For example, FMR torque efficiency, ξ_{FMR}, that is expected to show similar value to ξ_{DL} generated by the SHE in the NM layer, is calculated by taking the ratio between S_0 and A_0 as, [21]

$$\xi_{\mathrm{FMR}} = \frac{S_0}{A_0}\frac{e\mu_0 M_s t_{\mathrm{NM}} t_{\mathrm{FM}}}{\hbar}\sqrt{1+\frac{M_{\mathrm{eff}}}{H_0}}, \tag{1-10}$$

where t_{NM} is thickness of the NM layer and M_{eff} is the demagnetization field along OOP direction.

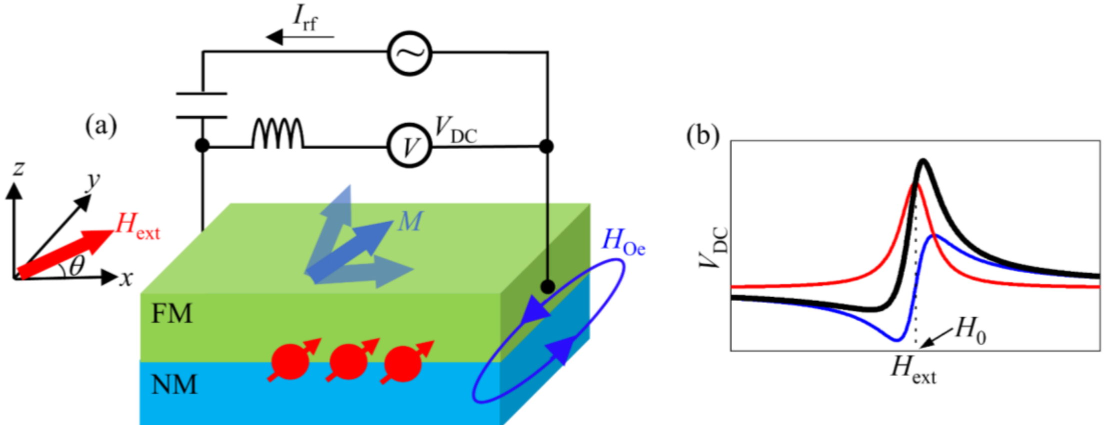

FIG. 1-9. (a) A schematic of the device structure and (b) a typical spectrum of the ST-FMR measurement. A black line indicates expected ST-FMR spectrum, and red and blue lines indicate symmetric and anti-symmetric Lorentzian component, respectively.

Table 1-1 Origin of the angular dependencies of the symmetric Lorentzian component, S.

θ dependence	$\sin2\theta\cos\theta$ (blue)	$\sin2\theta$ (green)	$\sin2\theta\sin\theta$ (purple)	$\sin\theta$ (brown)
Torque form	$\boldsymbol{M}\times(\boldsymbol{M}\times\boldsymbol{y})$	$\boldsymbol{M}\times\boldsymbol{z}$	$\boldsymbol{M}\times(\boldsymbol{M}\times\boldsymbol{x})$	
Origin	DL torque due to σ_y	FL torque due to σ_z	DL torque due to σ_x	
Oersted field		z		
Undesired effect	SP ISHE and ANE			SP ISHE and ANE

Table 1-2 Origin of the angular dependencies of the anti-symmetric Lorentzian component, A.

θ dependence	$\sin 2\theta \cos\theta$ (blue)	$\sin 2\theta$ (green)	$\sin 2\theta \sin\theta$ (purple)
Torque form	$\boldsymbol{M} \times \boldsymbol{y}$	$\boldsymbol{M} \times (\boldsymbol{M} \times \boldsymbol{z})$	$\boldsymbol{M} \times \boldsymbol{x}$
Origin	FL torque due to σ_y	DL torque due to σ_z	FL torque due to σ_x
Oersted field	$\boldsymbol{y}$		$\boldsymbol{x}$
Undesired effect			

σ_i: Spin polarization along the i direction

SP ISHE: Spin pumping and the inverse spin Hall effect

ANE: Anomalous Nernst effect

1.8.3 Second harmonic Hall measurement

Second harmonic Hall (SHH) measurement is another common way for estimating the SOT efficiency. In this method, AC electric current is applied to the NM/FM bilayer structure as shown in Fig. 1-10(a). Oersted field, DL-SOT, and/or FL-SOT oscillates magnetization of the FM layer. In this case, there is an additional term oscillating with f in the Hall resistance due to the AHE and planar Hall effect (PHE) because both depend on the direction of magnetization in the FM layer. Therefore, not only first harmonic but also second harmonic voltage is observed by lock-in-amplifier. Since the SHH voltage comes from the torques acting on the magnetization, SOT efficiency can be estimated by analyzing the SHH voltage [23]. Here, f is typically 10 ~1000 Hz, which is much smaller than that of ST-FMR. Therefore, oscillation of the magnetization is induced by the change of the magnetostatic energy and is not characterized by the LLG equation.

Here, the author briefly derives the SHH signal generated by the SOT. Magnetization is assumed to be aligned in the film plane by $\boldsymbol{H}_{\mathbf{ext}}$ as shown in Fig. 1-10(a). Time evolution of the Hall resistance, $R_{xy}(t)$, is written as,

$$R_{xy}(t) \approx R_{xy}(\boldsymbol{H}_{\mathbf{ext}}) + \frac{dR_{xy}}{d\boldsymbol{H}}|_{\boldsymbol{H}=\boldsymbol{H}_{\mathbf{ext}}} \cdot \boldsymbol{H}_{\boldsymbol{I}} \sin(2\pi f t), \tag{1-11}$$

where $\boldsymbol{H}_{\mathbf{I}} = \boldsymbol{H}_{\mathbf{DL}} + \boldsymbol{H}_{\mathbf{FL}} + \boldsymbol{H}_{\mathbf{Oe}}$ is the effective magnetic field due to DL-SOT, FL-SOT, and Oersted field. Amplitude of each field is expressed as,

$$H_{\mathrm{DL(FL)}} = \xi_{\mathrm{DL(FL)}} \frac{\hbar J_{\mathrm{c(NM)}}}{2e\mu_0 M_{\mathrm{s}} t_{\mathrm{FM}}}, \tag{1-12}$$

$$H_{\mathrm{Oe}} = \frac{1}{2} J_{\mathrm{c(NM)}} t_{\mathrm{NM}}. \tag{1-13}$$

By multiplying the AC electric current to Eq. (1-11) and taking time average, SHH resistance is given by $R_{xy}^{2\omega} = -\frac{1}{2}\frac{dR_{xy}}{d\boldsymbol{H}}|_{\boldsymbol{H}=\boldsymbol{H}_{\mathbf{ext}}} \cdot \boldsymbol{H}_{\boldsymbol{I}}$. Given that $\boldsymbol{H}_{\mathbf{DL}}$ and $\boldsymbol{H}_{\mathbf{FL}} + \boldsymbol{H}_{\mathbf{Oe}}$ are pointing along OOP and IP direction, respectively, the former oscillates AHE whereas the later oscillates PHE. Therefore, $R_{xy}^{2\omega}(\phi)$ [a typical example of the signal is shown in Fig. 1-10(b)] is composed of three different ϕ dependences as,

$$\begin{aligned} R_{xy}^{2\omega} &= -\frac{1}{2}\left(R_{\mathrm{AHE}} \frac{1}{H_{\mathrm{ext}} + H_{\mathrm{k}}} H_{\mathrm{DL}} + R_{\mathrm{PHE}} \frac{2\cos 2\varphi}{H_{\mathrm{ext}}} \cdot (H_{\mathrm{FL}} + H_{\mathrm{Oe}})\right)\cos\varphi + (R_{\mathrm{ANE}} + R_{\mathrm{ONE}} H_{\mathrm{ext}})\cos\varphi \\ &\quad + R_{\mathrm{PNE}} \sin 2\varphi \\ &= R_a \cos\varphi + R_{\mathrm{FL}}(2\cos^3\varphi - \cos\varphi) + R_{\mathrm{PNE}} \sin 2\varphi. \end{aligned} \tag{1-14}$$

Here, thermoelectric contributions such as the anomalous Nernst effect (ANE), ordinary Nernst effect (ONE), and planar Nernst effect (PNE) are included as R_{ANE}, R_{ONE}, and R_{PNE}, respectively [24]. R_{a} is composed of three different components as,

$$R_a = -\frac{R_{\mathrm{AHE}} H_{\mathrm{DL}}}{2(H_{\mathrm{ext}} + H_{\mathrm{k}})} + R_{\mathrm{ONE}} H_{\mathrm{ext}} + R_{\mathrm{ANE}}. \tag{1-15}$$

H_{DL} can be extracted from H_{ext} dependence of R_{a} as shown in Fig. 1-10(c), and ξ_{DL} can be estimated using Eq. (1-12).

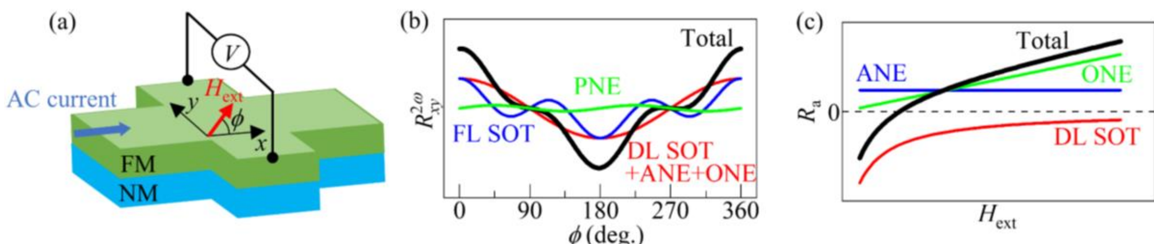

FIG. 1-10. (a) A schematic of the device structure. (b) Typical θ dependence and (c) H_{ext} dependence of the SHH resistance.

1.8.4 Detection of spin-orbit effective field

FL-SOT can be estimated from the shift of the magnetoresistance (MR) curve. When H_{ext} is swept along y direction with application of DC electric current, I_{DC}, along x direction as shown in Fig. 1-11(a), magnetization feels not only H_{ext} but also $H_{\mathrm{FL}} + H_{\mathrm{Oe}}$. Since only the latter one is proportional to I_{DC}, shift of the MR curve induced by I_{DC} simply corresponds to $H_{\mathrm{FL}} + H_{\mathrm{Oe}}$ as shown in Fig. 1-11(b) [25]. By subtracting contribution from H_{Oe} using Eq. (1-13), FL-SOT can be estimated. In this case, however, we need to keep in mind that Joule heating also modulates the shape of the MR.

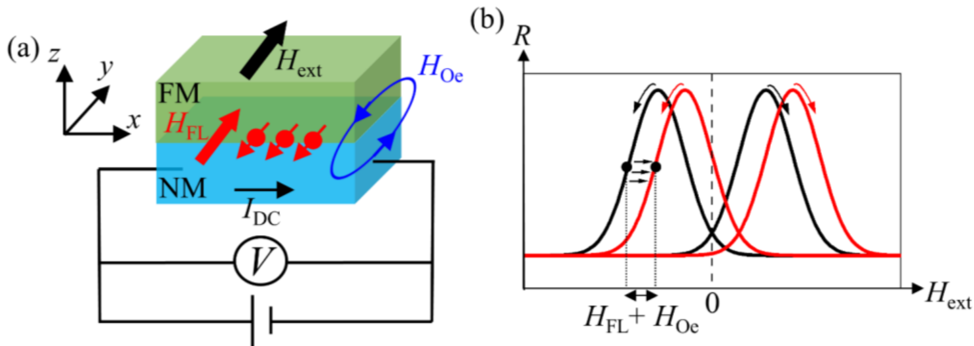

FIG. 1-11. (a) A schematic of the device structure and (b) a typical signal of the measurement of the shift of the MR curve. Red and black lines are the MR curve detected with and without application of I_{DC}.

1.9 Research purpose and outline of this dissertation

In this dissertation, the author investigates SOT in metallic bi-layer and single-layer structures aiming at realization of efficient SOT switching for application to the writing process of SOT-MRAM.

First, the author established a novel method for detecting SOT-induced magnetization switching without any

complicated fabrication processes. As discussed in section 1.8.1, fabrication of MTJ is usually required to detect SOT switching of a FM with IP magnetic anisotropy. In this case, not only additional electrical circuit but also complicated fabrication process is needed as shown in Fig. 1-12(a). For agile investigation of SOT switching using various materials, circuits, and/or device structures, the author developed a novel method for detecting SOT switching without fabricating MTJ as shown in Fig. 1-12(b) (Chap. 2). In addition, the author found that the background signal coexisting with the ST-FMR spectrum enables estimation of the SHA of the NM layer, realizing more reliable estimation of the SHA (Chap. 3). Next, the author demonstrated ultrafast and low-power consumption SOT switching by applying two current pulses, which is detected using the method established in Chap. 2. At the same time, analog control of magnetization for neuromorphic computing was demonstrated (Chap. 4). Then, the author found that current-induced OOP torque is generated by the asymmetry of the electrode connected to the FM layer. Micromagnetic simulation showed the OOP torque enables field-free switching of a FM with OOP magnetic anisotropy (Chap. 5). Next, SOT generated by the SHE in a FM in a NM/FM bilayer structure, called the self-induced SOT (SI-SOT), was investigated. It was found that proper selection of the FM layer can enhance the SOT in the NM/FM bilayer structure. Moreover, SI-SOT was found to influence significantly on the estimation of the SOT efficiency especially when a low-conductive NM layer is used (Chap. 6). Following this work, SI-SOT in a Weyl ferromagnet Co_2MnGa (CMG) was investigated. SOT efficiency was comparable to that of a heavy metal/FM bilayer structure even without adjacent metal layer. Moreover, sign and magnitude of the SI-SOT were strongly dependent on the applied-current direction with respect to the crystal axis of the CMG film. These findings stem from the topology in band structure and its modulation by external strain (Chap. 7). Finally, the author summarizes this doctoral thesis (Chap. 8).

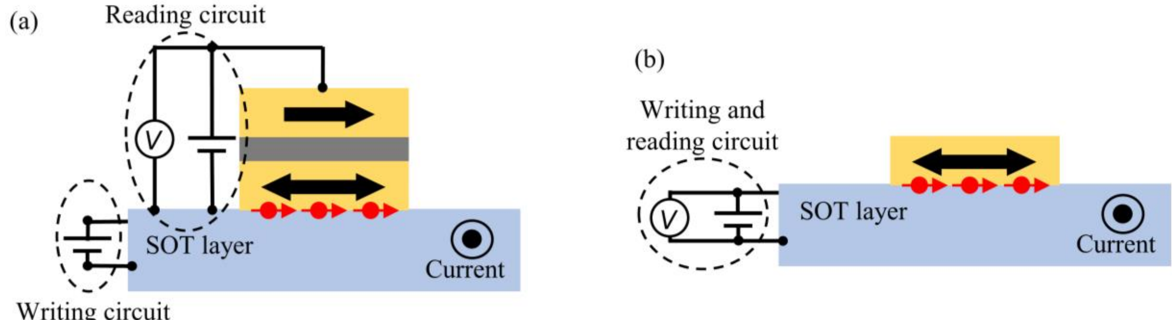

FIG. 1-12. Schematics of the device structure for measuring SOT-induced magnetization switching with (a) three and (b) two electrodes.

Chapter 2. Detection of spin-orbit torque magnetization switching by low-frequency spin-torque ferromagnetic resonance

2.1 Abstract

Spin-orbit torque has been investigated intensively aiming at application to the magnetoresistive random access memory. A variety of materials such as heavy metals [21,26,27], topological insulators [19,28,29], and Van der Waals materials [30,31] have been found to possess significant charge-to-spin conversion and resulting spin-orbit torque generation in the previous works. However, in most cases, the spin-orbit torque efficiency is detected with "indirect" measurement but not a demonstration of spin-orbit torque magnetization switching, especially when a ferromagnet with in-plane magnetic anisotropy that shows field-free spin-orbit torque switching is used. This is because measuring magnetization switching of an in-plane ferromagnet usually requires fabrication of magnetic tunnel junction [26,27], which means complicated fabrication process is needed. It is known that correlation between spin-orbit torque efficiency estimated from the indirect method and the actual current density required for switching is weak [20], indicating importance of demonstrating spin-orbit torque switching in the phase of developing material, structure, and/or circuit.

In this study, the author established a novel method to detect spin-orbit torque magnetization switching of an in-plane ferromagnet using the spin rectification effect. It was found that the rectification signal measured by irradiating microwave current to a nonmagnet/ferromagnet bilayer system shows hysteresis behavior corresponding to the hysteresis of the magnetization around zero magnetic field. Moreover, the author found that the hysteresis is significantly enhanced as decreasing microwave frequency. Using this feature, the author successfully detected spin-orbit torque magnetization switching of a permalloy electrode as small as 100 nm using the spin Hall effect of Pt. Since this method does not require any complicated fabrication process, *i.e.*, simply composed of a nonmagnet/ferromagnet channel and two electrodes, this method will enable agile spin-orbit torque research.

Results presented in this chapter were published in the papers:

M. Aoki, E. Shigematsu, M. Matsushima, R. Ohshima, S. Honda, T. Shinjo, M. Shiraishi, and Y. Ando, "In-plane spin-orbit torque magnetization switching and its detection using the spin rectification effect at subgigahertz frequencies", Physical Review B **102**, 174442 (2020).

M. Aoki, E. Shigematsu, M. Matsushima, R. Ohshima, S. Honda, T. Shinjo, M. Shiraishi, and Y. Ando, "Enhancement of low-frequency spin-orbit-torque ferromagnetic resonance signals by frequency tuning observed in Pt/Py, Pt/Co, and Pt/Fe", AIP Advances **11**, 025206 (2021).

2.2 Introduction and research purpose

Spin-rectification effect (SRE), in which non-zero DC voltage is generated under irradiation of microwave current owing to oscillation of resistance originating from magnetization precession, is generally utilized to observe the FMR such as the ST-FMR method (see 1.8.2) [32]. On the other hand, the SRE is also observed at around zero magnetic field, which is called the non-resonant SRE (nr-SRE) [33]. Origin of the nr-SRE is oscillation of the resistance induced by modulation of magnetic-domain states due to Oersted field and/or SOT. Figure 2-1(a) shows a typical MR curve of a NM/FM bilayer system with IP magnetic anisotropy. Resistance, R, of a typical FM such as Co, Fe, and Ni, increases around zero magnetic field due to domain-wall nucleation and AMR. When a RF current, I_{rf}, is applied, Oersted field, H_{Oe}, is generated, which is converted into oscillation of the resistance, R_{ac}. Since both I_{rf} and R_{ac} are oscillating with the same frequency, non-zero DC voltage, V_{DC}, is generated due to rectification effect. Characteristic of the nr-SRE is the hysteresis behavior corresponding to direction of magnetization because the sign of the slope in the MR curve changes with respect to the sign of M as shown in Fig. 2-1(b). Therefore, one might expect that magnetization reversal of a FM with IP magnetic anisotropy can be detected using the nr-SRE. However, signal amplitude of the nr-SRE is much smaller than that of the ST-FMR, limiting sensitivity for detecting magnetization reversal [33]. If signal amplitude of the nr-SRE can be significantly enhanced, magnetization switching of a small FM will be detected, which is a great advantage in sense of search of novel materials for SOT-MRAM application compared to MTJ method because the device structure for measuring nr-SRE is simply composed of a NM/FM bilayer and two electrodes. In addition, this method might be used for a small FM that is not applicable to the MOKE method because nr-SRE is not limited by the resolution of light.

The purpose of this research is to establish a way for detecting SOT magnetization reversal by enhancing the amplitude of nr-SRE.

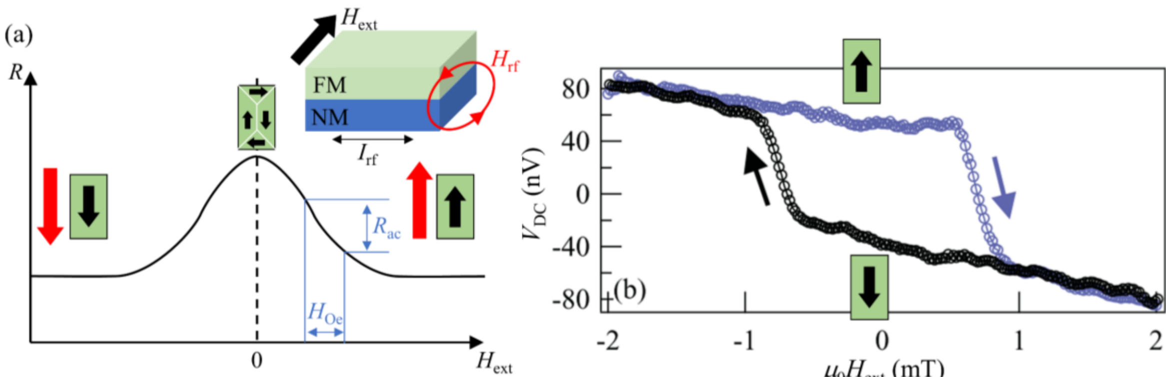

FIG. 2-1. (a) A typical MR curve and schematics of magnetic-domain structures of a NM/FM bilayer structure with IP magnetic anisotropy. AC Oersted field, H_{Oe}, is converted into the oscillating resistance, R_{ac}. (b) A typical spectrum of the nr-SRE adapted from: X. F. Zhu *et al.*, Phys. Rev. B **83**, 140402(R) (2011) [33].

2.3 Experimental setup

2.3.1 Sample fabrication

First, rectangular-shaped Pt (15 nm)/FM (4 nm)/MgO (2 nm) structure was fabricated on a MgO (001) substrate by using electron-beam (EB) lithography and EB deposition technique. Then the sample was immediately moved into DC magnetron sputtering system to fabricate capping layer of SiO_2 (7 nm) [Figs. 2-2(a) and 2-2(b)]. Pt is chosen as the NM layer because it possesses high SHA and is expected to realize SOT magnetization switching owing to spin-current injection into adjacent FM [18,21]. Permalloy ($Ni_{81}Fe_{19}$, Py), Co, and Fe are used as the FM layer. After fabrication of Pt/FM/MgO/SiO_2 multilayer, size of the FM layer was downsized using rectangular masks made of negative resist and Ar+ ion milling [Figs. 2-2(c) and 2-2(d)]. Then, coplanar waveguide made of Ti(3 nm)/Au(100 nm) was fabricated using EB lithography and EB evaporation after etching of surface oxidation layers using Ar+ ion milling [Fig. 2-2(e)] without breaking vacuum.

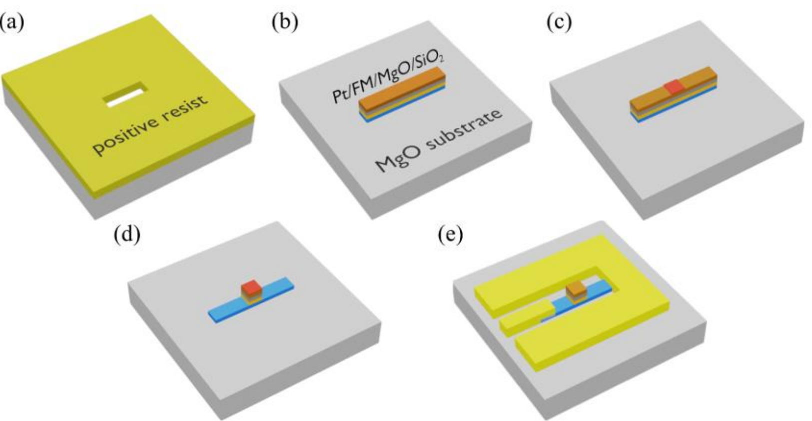

FIG. 2-2. Schematics of the device after (a) development of positive resist, (b) fabrication of channels, (c) development of negative resist, (d) Ar ion milling, and (e) fabrication of electrode.

2.3.2 Measurement setup

Figures 2-3(a) and 2-3(b) show schematics of the device structure and measurement circuit, respectively. Microwave current, I_{rf}, with a frequency, f, and power, P, was irradiated using a commercial signal generator (KEYSIGHT N5173B EXG). Rectification voltage, V_{DC}, is measured using a nanovoltmeter (Keithley Nanovoltmeter 2182 A) via a vias tee. A pulse current for inducing SOT magnetization switching was injected

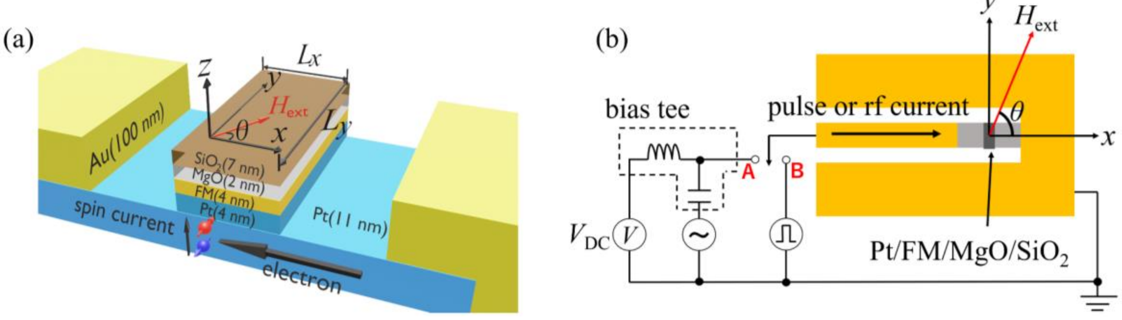

FIG. 2-3. (a) Schematics of the device structure and (b) electrical circuit used in this study.

using a function generator (Agilent 33622A). Magnetic field, H_{ext}, was applied along IP direction. Relative angle between H_{ext} and I_{rf} is defined as θ. V_{DC} is measured by connecting the circuit with "A", whereas pulse current for SOT switching was injected by connecting the circuit with "B" as shown in Fig. 2-3(b).

2.4 Observation of the low-frequency spin-torque ferromagnetic resonance in Pt/permalloy bilayer system

2.4.1 Material characterization

First, ST-FMR measurement was carried out for the Pt/Py/MgO/SiO_2 device under an irradiation of high-frequency microwave. θ and P were fixed to be 45° and 10 dBm, respectively. Figure 2-4(a) shows the ST-FMR spectra with different f for the device with L_x = 500 nm and L_y = 20 μm. From the fitting to the measured ST-FMR spectra using Eq. (1-7) [solid lines in Fig. 2-4(a)], FMR magnetic field, H_0, and FMR line width, Γ, were obtained. f-μ_0H_0 plot was fitted by using Eq. (1-4) as shown in Fig. 2-4(b). $\mu_0\Gamma$-f plot was fitted by the linear function,

$$\Gamma = \frac{2\pi f}{\gamma}(\alpha + \alpha_0), \tag{2-1}$$

where α_0 is inhomogeneous damping as shown in Fig. 2-4(c). Both plots were fitted well, indicating successful observation of the FMR. From the fittings in Figs. 2-4(b) and 2-4(c), μ_0M_{eff} and α were estimated to be 0.58 T and 0.046, respectively, which is consistent with reported values for Pt/Py system [21].

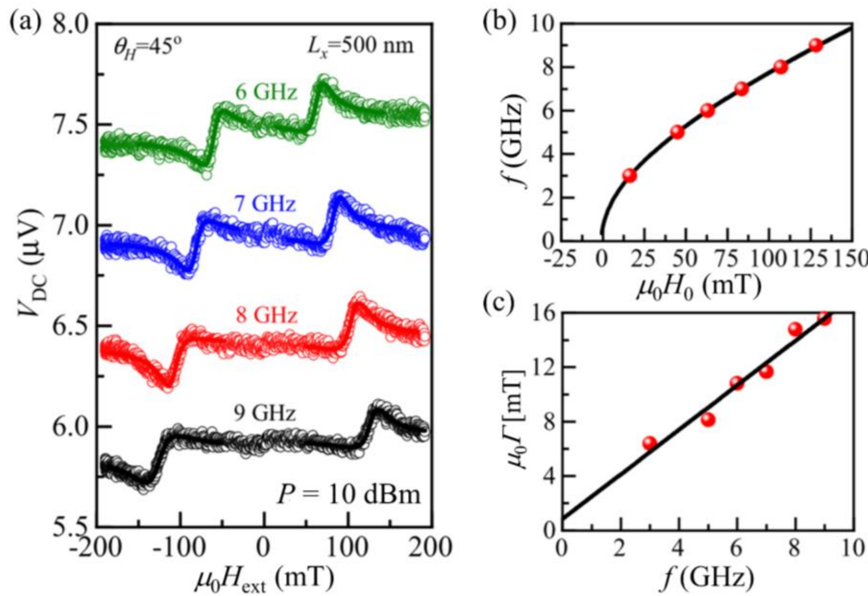

FIG. 2-4. (a) ST-FMR spectra for the Pt/Py/MgO/SiO_2 device with different f. (b) f as a function of μ_0H_0 fitted by Eq. (4). (c) $\mu_0\Gamma$ as a function of f fitted by the linear function.

2.4.2 Frequency dependence of the non-resonant spin-rectification effect

In this section, we focus on nr-SRE observed around zero magnetic field. Figure 2-5 shows V_{DC} as a function of μ_0H_{ext} with various f for the Pt/Py/MgO/SiO_2 with L_x = 500 nm and L_y = 20 μm, where θ = 0° and P = 10

dBm. When f is higher than 2 GHz, nr-SRE is negligibly small as shown in Figs. 2-5(a). However, as decreasing f, nr-SRE signal is significantly enhanced (here we call this as the LFST-FMR). The fact that the LFST-FMR is observed even when $\theta = 90°$ means that the origin of the LFST-FMR is different from that of the ST-FMR. Figures 2-5(b)-2-5(g) show the LFST-FMR signals shown in Fig. 2-5(a) enlarged around zero magnetic field. Small nr-SRE was observed at 3 GHz and 5 GHz. However, magnitude of the hysteresis of the signal, ΔV_0, is too small to detect magnetization direction. On the other hand, as decreasing f, ΔV_0 was obviously enhanced.

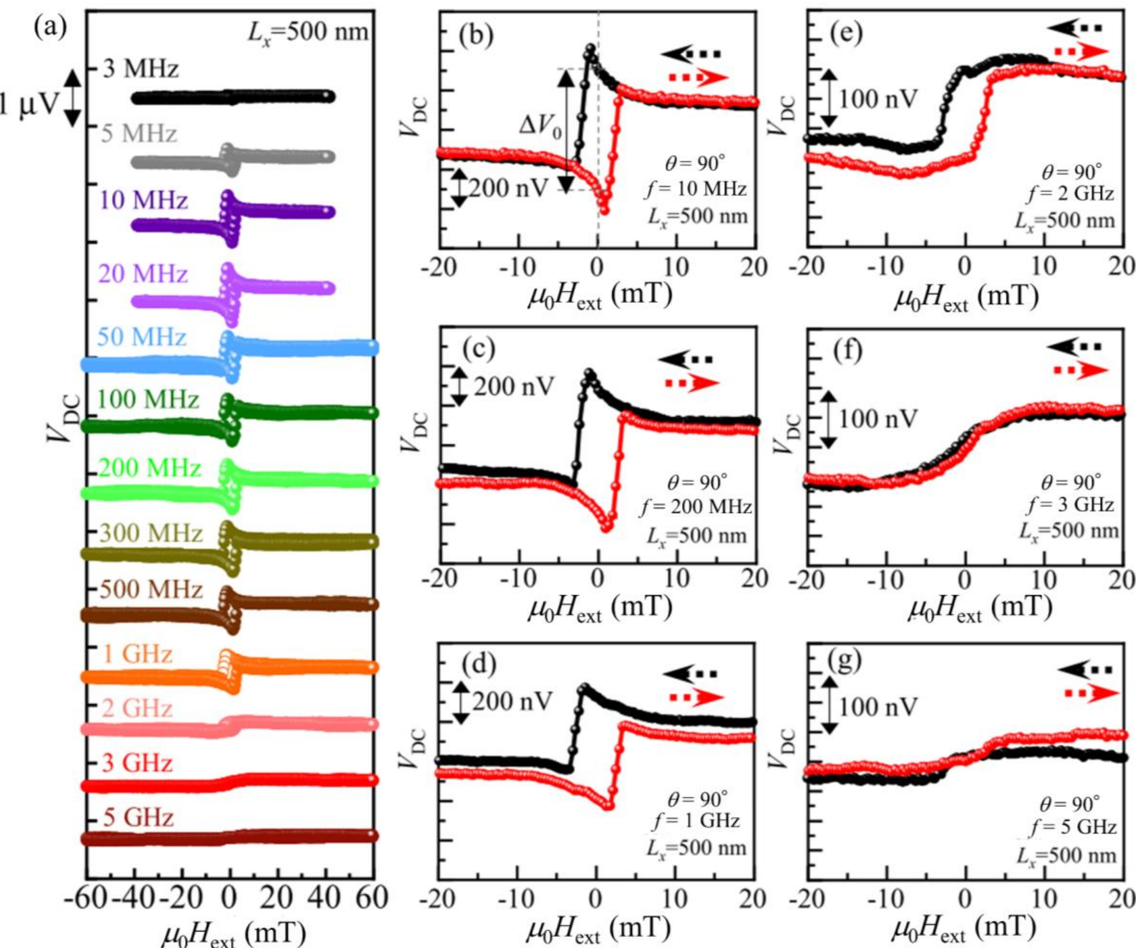

FIG. 2-5. (a) V_{DC} as a function of $\mu_0 H_{ext}$ measured with $\theta = 90°$. (b-g) Enlarged signals with f = (b) 10 MHz, (c) 200 MHz, (d) 1 GHz, (e) 2 GHz, (f) 3 GHz, and (g) 5 GHz are also shown.

2.5 Analyzation of the low-frequency spin-torque ferromagnetic resonance

2.5.1 Low-frequency spin-torque ferromagnetic resonance in Pt/Co, Pt/Fe, and Pt/permalloy bilayers

To investigate the origin of the LFST-FMR, the author additionally fabricated Pt/Co/MgO/SiO_2, Pt/Fe/MgO/SiO_2, and Pt/Py/MgO/SiO_2 structures with L_x = 500 nm and L_y = 2 μm, and compared f dependence of the nr-SRE as shown in Figs. 2-6(a)-2-6(c). In all devices, LFST-FMR was observed at lower f. However, threshold value of f depends on FM. For example, LFST-FMR in the Py device starts to be visible below f = 2

GHz whereas that of Co and Fe starts to be visible below $f = 7$ and 5 GHz, respectively. Here the author focuses on the fact that FMR frequency at zero magnetic field depends on M_s and magnetic anisotropy of the FM. According to Eq. (1-4), FM with larger M_s shows FMR at larger f. Given that M_s of Fe and Co are larger than that of Py, LFST-FMR seems to appear when f is below the FMR frequency at zero magnetic field. Susceptibility of the magnetization becomes non-zero when f is below the FMR condition, which enhances oscillation of domain-wall state and resistance via the MR effect. On the other hand, susceptibility becomes zero when f is above the FMR condition because magnetization motion cannot follow the external forces.

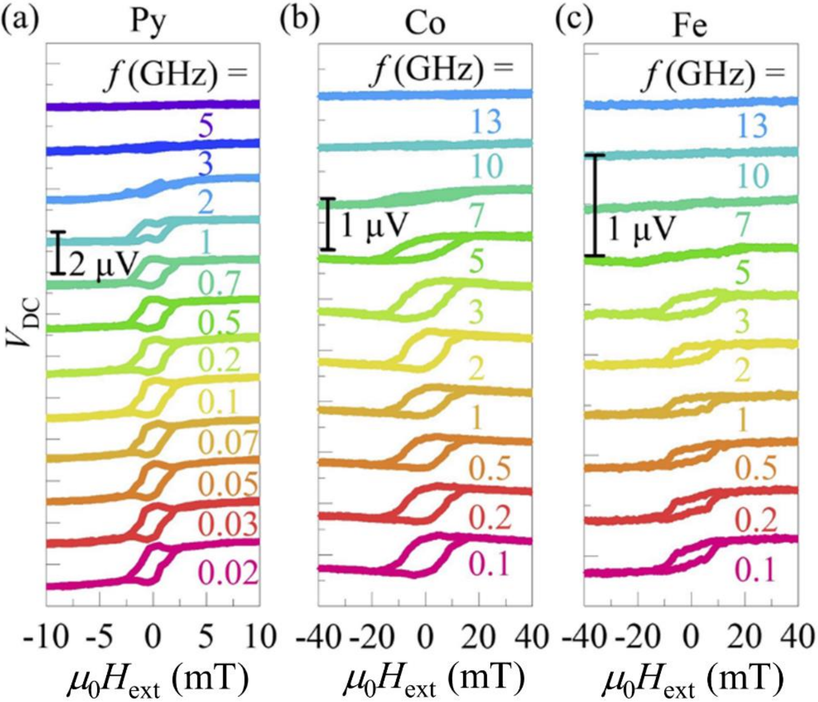

FIG. 2-6. V_{DC} as a function of $\mu_0 H_{ext}$ with different f for (a) Pt/Py, (b) Pt/Co, and (c) Pt/Fe bilayers. P and θ were fixed to be 5 dBm and 90°, respectively.

2.5.2 Relationship between anisotropic magnetoresistance

To verify that LFST-FMR is induced by oscillation of the domain-wall state and MR effect, resistance of the multilayer, R, was measured with changing H_{ext} along y axis as shown in Fig. 2-7. Peaks in resistance such as a schematic shown in Fig. 2-1(a) were observed, indicating that domain-wall state pointing along x direction were nucleated in all devices. In this case, RF Oersted field coming from I_{rf} in Pt causes oscillation of R as shown in Fig. 2-1(a). Therefore, amplitude of the LFST-FMR, ΔV_0, is expressed as,

$$\Delta V_0 = 2\chi \langle I_{rf(0)} \sin(2\pi f t) H_{Oe} \frac{\mathrm{d}R}{\mathrm{d}H_{ext}} \sin(2\pi f t - \varphi) \rangle, \qquad (2\text{–}1)$$

where <> means time average, χ is normalized magnetic susceptibility (~ 1 at low-frequency limit), $I_{rf(0)}$ is the amplitude of I_{rf}, H_{Oe} is Oersted field acting on magnetization of the FM, and φ is the phase shift between magnetization precession and the RF current (~ 0° at low-frequency limit, ~ 180° at high-frequency limit). Since the peak position of up- and down-sweep signals are different due to small in-plane magnetic anisotropy

originating from the shape of the FM electrode, slope of the resistance is opposite to each other with respect to the sweep direction in all devices as shown in insets of Fig. 2-7, resulting in voltage level depending on the direction of magnetization in V_{DC}. Fig. 2-8 shows ΔV_0 as a function of f for three different Pt/FM/MgO/SiO_2 structures. Magnitude of ΔV_0 was strongly dependent on the material used as the FM electrode. Since ΔV_0 is proportional to the slope of the MR curve, positive correlation between ΔV_0 and the slope of the MR curve is expected. Table 2-1 shows the comparison of the magnitude of LFST-FMR at f = 100 MHz and the slope of the magnetoresistance curve, as well as the resistivity of the FM, ρ,

I_{rf}, and H_{Oe}. All values except for ρ are normalized by those of Pt/Py/MgO/SiO_2 devices. Positive correlation between the LFST-FMR and the slope of the magnetoresistance was found, which is consistent with the expectation.

TABLE 2-1. Comparison of the amplitude of MR and LFST-FMR.

FM	ΔV_0	ρ (μΩ • cm)	I_{rf}	H_{Oe}	$\frac{dR}{dH_{ext}}$
Py	1	55	1	1	1
Co	0.41	72	1.01	1.03	0.75
Fe	0.09	58	0.99	0.99	0.13

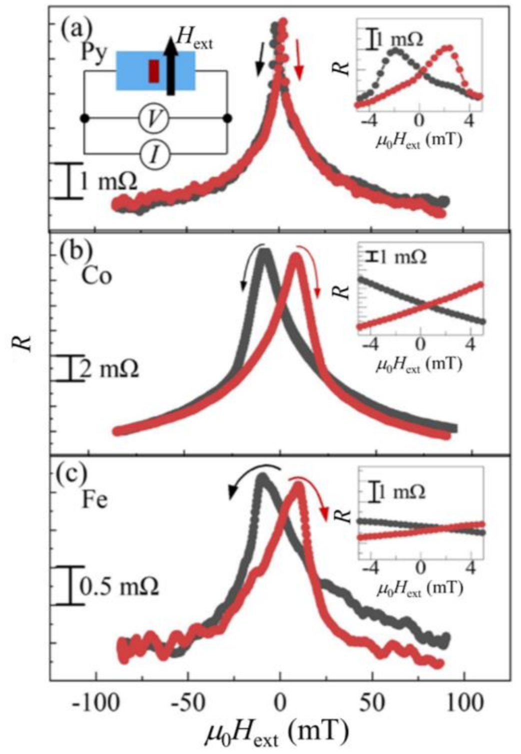

FIG. 2-7. MR curve for (a) Pt/Py/MgO/SiO_2, (b) Pt/Co/MgO/SiO_2, and (c) Pt/Fe/MgO/SiO_2 layers. Insets show the signal enlarged around zero magnetic field.

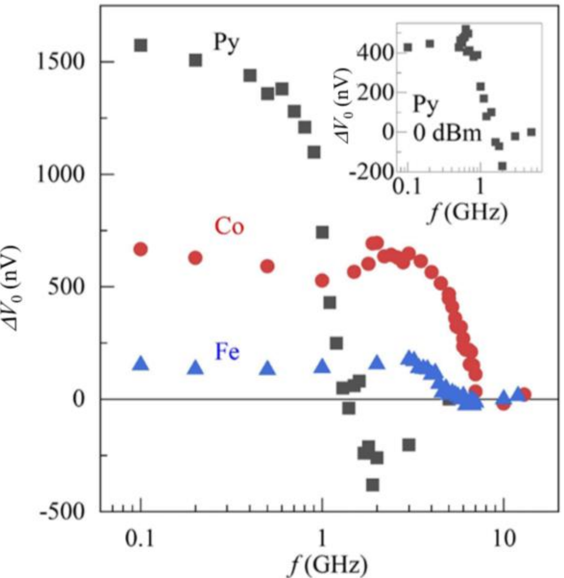

FIG. 2-8. ΔV_0 as a function of f with a microwave power of 5 dBm. Inset shows ΔV_0 as a function of f with a microwave power of 0 dBm for Pt/Py/MgO/SiO_2 bilayer.

2.5.3 Micromagnetic simulation

To further confirm the expectation that the LFST-FMR comes from oscillation of the magnetic-domain states due to the Oersted field, micromagnetic simulation using MuMax3 [34] was carried out (see Appendix Section A for details of calculation). Parameters used in the simulation are shown in Table 2-2. Figures 2-9(a) - 2-9(c) show χ and $\chi\langle\sin(2\pi f t)\sin(2\pi f t-\varphi)\rangle$ as a function of *f*. The former is obtained by normalize oscillation amplitude by that in the low-frequency limit. The latter corresponds to the normalized amplitude of the LFST-FMR. Peak in χ owing to FMR was reproduced in all cases. Indeed, $\chi\langle\sin(2\pi f t)\sin(2\pi f t-\varphi)\rangle$ is enhanced as increasing f and shows sign inversion when f becomes higher than the FMR condition. Then, $\chi\langle\sin(2\pi f t)\sin(2\pi f t-\varphi)\rangle$ becomes zero at high-frequency limit. This trend qualitatively corresponds to experimental result shown in Fig. 2-8. Therefore, the author concluded that (1) LFST-FMR is generated due to the oscillation of the domain-wall state induced by the Oersted field and (2) LFST-FMR appears with frequencies lower than the FMR condition because magnetic susceptibility becomes nonzero.

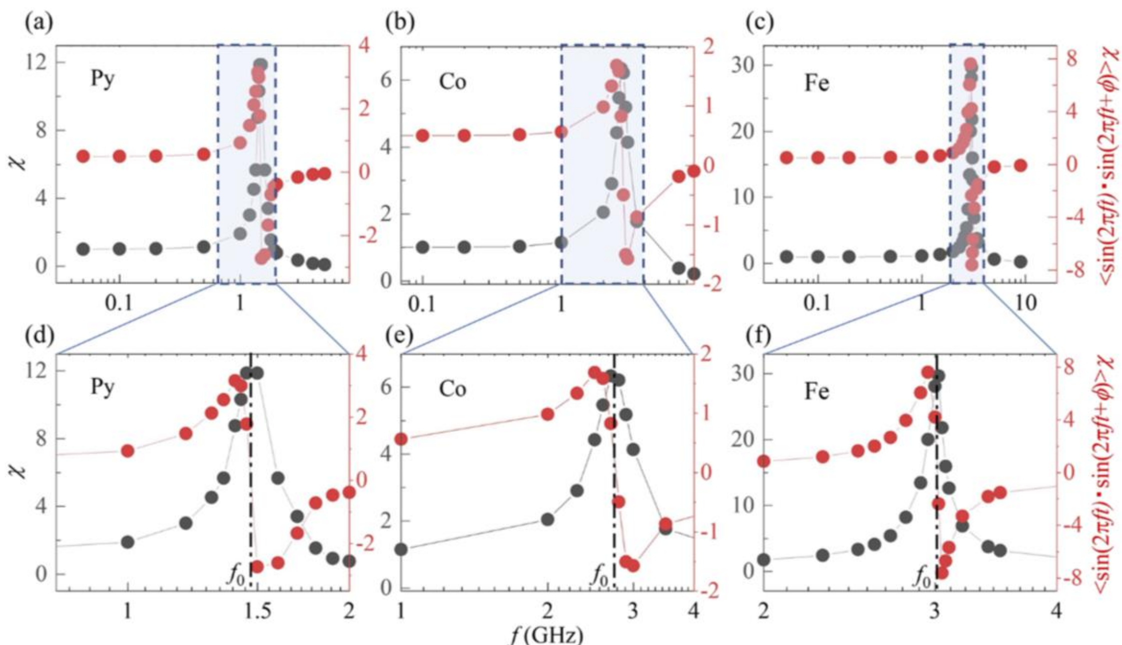

FIG. 2-9. Frequency evolution of χ and $\chi\langle\sin(2\pi f t)\sin(2\pi f t-\varphi)\rangle$ for (a) Pt/Py/MgO/SiO_2,(b) Pt/Co/MgO/SiO_2, and (c) Pt/Fe/MgO/SiO_2 bilayers calculated by MuMax3. Signals enlarged around zero magnetic field are also shown in (d-f).

TABLE 2-2. Parameters used in the micromagnetic simulation.

FM	M_s (MA/m)	α	A_{ex} (pJ/m)	f_0 (GHz)
Py	0.46 [34]	0.008 [35]	13 [34]	1.43
Co	1.15 [36]	0.011 [35]	19 [37]	2.8
Fe	1.36 [38]	0.0019 [35]	19 [39]	3

2.6 Detection of the spin-orbit torque magnetization switching

2.6.1 Experimental procedure

In this section, the author demonstrates detection of the SOT-induced magnetization switching by the LFST-FMR. Figure 2-10(a) shows the procedure for measuring SOT magnetization switching. First, magnetization is initialized by applying large positive magnetic field, H_{set}. After setting magnetic field to H_{PLS} (0 mT unless otherwise noted), LFST-FMR is measured with an irradiation of low-frequency microwave. In this case, voltage level of V_{DC} corresponds to the voltage level of the LFST-FMR swept from the positive magnetic field [A blue dot in Fig. 2-10(c)]. Then, microwave irradiation is stopped and pulse current for SOT magnetization switching is injected. Finally, microwave is irradiated and V_{DC} is measured again. If the applied pulse-current density, J_{PLS}, is large enough, magnetization is successfully switched from positive to negative and the voltage level of V_{DC} also switches to that of the LFST-FMR swept from the negative magnetic field [A red dot in Fig. 2-10(c)]. When the difference between V_{DC} measured before and after application of pulse current, ΔV, is plotted as a function of J_{PLS}, signal shown in Fig. 2-10(b) is expected to be measured. In the demonstration of SOT switching, L_x, L_y, f, P, and pulse width, W_{PLS}, were fixed to be 500 nm, 20 μm, 200 MHz, 10 dBm, and 1 μs, respectively.

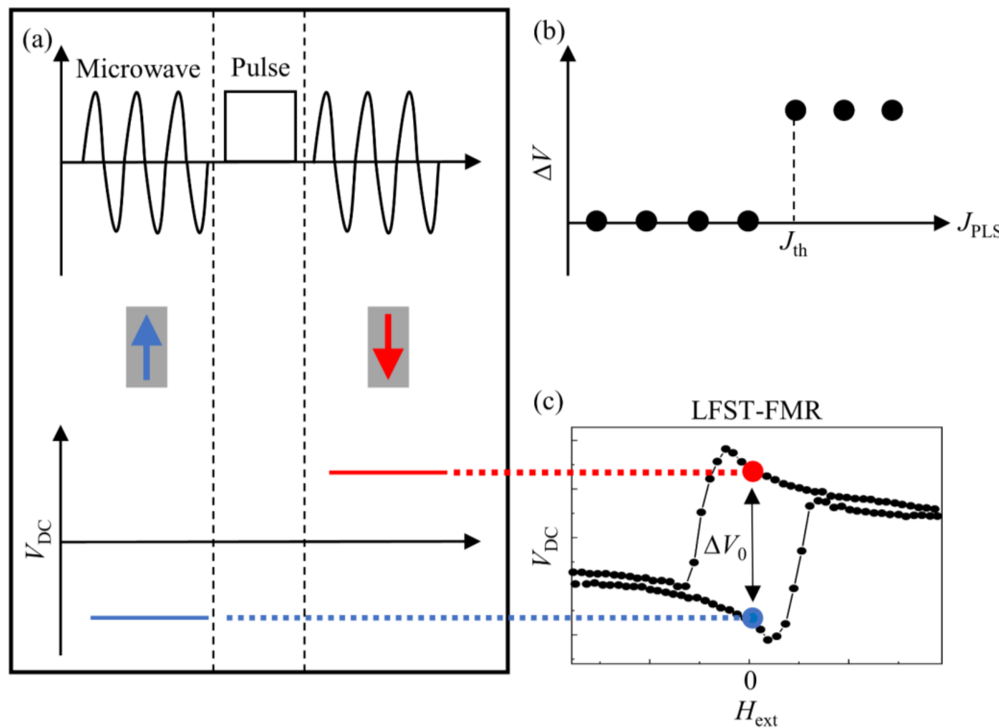

FIG. 2-10. (a) A schematic of measurement procedure for detecting SOT-induced magnetization switching. (b) A typical switching signal with a threshold current density of J_{th} and (c) hysteresis in the LFST-FMR spectrum.

2.6.2 Microwave frequency and pulse width dependence

Figure 2-11(a) shows ΔV as a function of J_{PLS} detected with different frequencies of microwave for the Pt/Py/MgO/SiO_2 device. Nonzero ΔV due to SOT switching is observed above J_{PLS} = 10 MA/cm^2 only when

low-frequency microwave is used, which is consistent with the frequency dependence of the LFST-FMR, in which ΔV_0 is negligibly small above 2 GHz (see Fig. 2-5). Figure 2-11(b) shows the SOT switching signal for Pt/Py/MgO/SiO_2 devices with different L_x. ΔV-J_{PLS} plot became steeper in narrower devices because of suppression of domain-wall nucleation and resulting macro-spin-like switching. Figure 2-11(c) shows the SOT switching signal by applying pulse currents with different W_{PLS}. Threshold value of J_{PLS} increases as W_{PLS} decreases. This is because the switching process is dominated by domain-wall motion when relatively large FM electrode is used. Domain-wall motion becomes faster as J_{PLS} becomes higher, resulting in larger J_{PLS} that is needed for SOT switching as W_{PLS} became shorter [40]. Composing up- and down-sweep signals after changing the offsets, hysteresis behavior of ΔV as a function of J_{PLS} was clearly obtained as shown in Fig. 2-11(d). Since all these characteristics are consistent with the behavior expected for in-plane magnetization switching of Py, the author insists that LFST-FMR can be a powerful tool for detecting SOT magnetization switching of FM with IP magnetic anisotropy.

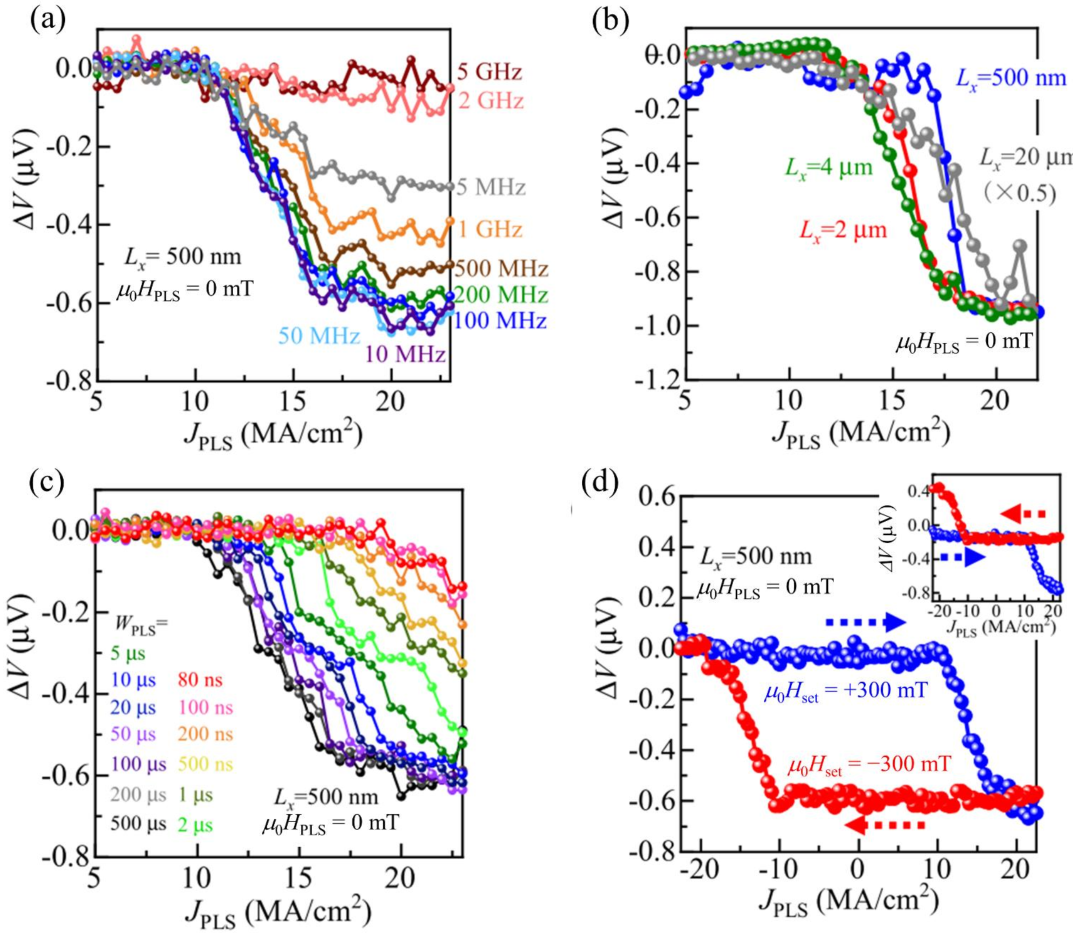

FIG. 2-11. (a) SOT-induced magnetization switching detected with different microwave frequencies, (b) channel length, and (c) pulse width. (d) Full switching signal obtained by sweeping J_{PLS} upwards and downwards. Inset shows the signal before adjusting the offset value. Note that signals shown in (b) is normalized for comparing devices with different size of FM electrode.

2.6.3 Downsizing of the ferromagnetic electrode

To demonstrate high sensitivity of the LFST-FMR method, size of the FM electrode was downsized to L_x = 100 nm and L_y = 1000 nm. Length of the FM channel, which determines the signal amplitude of the LFST-FMR, is as small as the size of the practical MRAM cell. Indeed, there has been no way other than fabricating MTJ to detect magnetization reversal of such a small FM electrode, because it is much less than the resolution of MOKE microscope. Surprisingly, clear LFST-FMR and SOT switching signal were successfully observed as shown in Figs. 2-12(a) and 2-12(b), respectively, indicating high-sensitivity of the LFST-FMR method. The author notes that using small FM electrode in the study on SOT switching is preferable because the mechanism of magnetization switching differs depending on the size of the FM electrode, *i.e.*, domain-wall nucleation is dominant for a large FM electrode whereas macro-spin motion is dominant for a FM electrode as small as 100 nm (a size of practical MRAM cell). Therefore, J_{th} of a small FM measured by the LFST-FMR method is more reliable when evaluating characteristics for device application compared to J_{th} of a large FM measured by the MOKE microscope.

Finally, one might think that the magnetization switching of Py discussed so far is caused by H_{Oe} induced by the electric current flowing in Pt but not by the SOT. To eliminate contribution of H_{Oe}, the author set H_{PLS} to be nonzero to cancel the contribution of H_{Oe} during pulse injection. The maximum value of $\mu_0 H_{Oe}$ is expected to be ~ − 2 mT within the range of J_{PLS} in Fig. 2-12(b). Even when $\mu_0 H_{PLS}$ = + 2 mT, magnetization switching was still observed as shown in Fig. 2-12(b). Therefore, the author concluded that the dominant contributor to the current-induced magnetization switching in our experiment is the SOT but not the Oersted field.

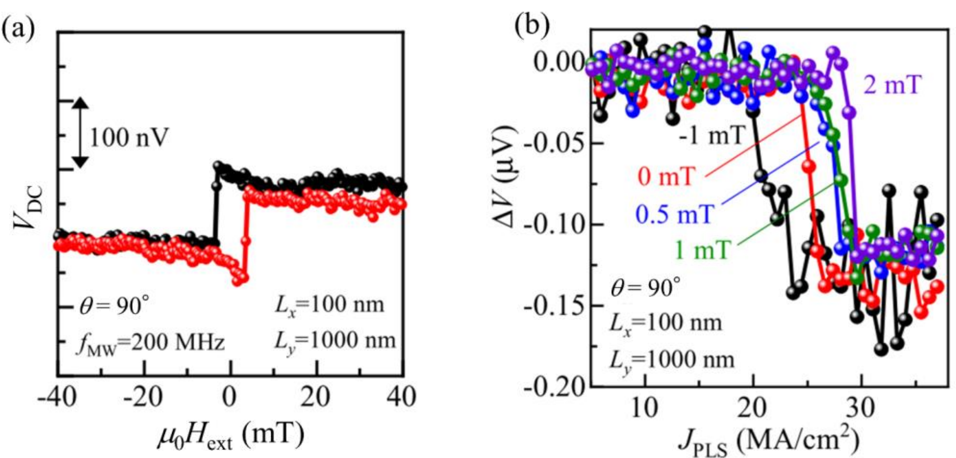

FIG. 2-12. (a) LFST-FMR spectrum and (b) SOT-induced switching signal measured in a Pt/Py/MgO/SiO_2 multilayer with a channel width of 100 nm with different values of H_{PLS}.

2.7 Summary

To summarize, the author established a novel way for detecting spin-orbit torque magnetization switching by using enhancement of the non-resonant spin-rectification effect, named as the low-frequency spin-torque

ferromagnetic resonance. Origin of the low-frequency spin-torque ferromagnetic resonance is an oscillation of the domain-wall state induced by the Oersted field and resulting oscillation of the resistance. The low-frequency spin-torque ferromagnetic resonance method does not require magnetic tunnel junction and is sensitive enough to detect magnetization switching of a ferromagnetic electrode as small as 100 nm. Therefore, the low-frequency spin-torque ferromagnetic resonance method is easily applicable to a wide variety of systems composed of novel materials and enables agile investigation on spin-orbit torque switching aiming at realization of low-power-consumption magnetoresistive random access memory.

Chapter 3. Coexistence of the low-frequency spin-torque ferromagnetic resonance and unidirectional spin Hall magnetoresistance

3.1 Abstract

In Chap. 2, the author developed a novel way for detecting spin-orbit torque magnetization switching, called the low-frequency spin-torque ferromagnetic resonance method. Following this study, the author applied the low-frequency spin-torque ferromagnetic resonance method to a Ta/Co bilayer system. In this case, however, large background signal, polarity of which depends on the magnetization direction, was dominant over the low-frequency spin-torque ferromagnetic resonance signal. Although small background signal was observed in Pt/Co bilayer, polarity was opposite to that of the Ta/Co bilayer structure. Since the sign of the spin Hall angle of Ta and Pt are opposite to each other, the author expected that the background signal is induced by the nonreciprocal charge transport induced by the spin Hall effect, *i.e.*, unidirectional spin Hall magnetoresistance.

In this chapter, the author investigates the background signal with changing various parameters: microwave power, frequency, magnetic field angle, amplitude, and temperature. As a result, the author verified that the background signal originates from the spin-dependent unidirectional spin Hall magnetoresistance. Given that the spin-dependent unidirectional spin Hall magnetoresistance is numerically calculated using spin-diffusion model, the spin Hall angle of Pt and Ta were estimated to be 0.052 and −0.084 from the value of the background signal, respectively. In addition, detection of spin-orbit torque magnetization switching of W/Co bilayer system was demonstrated using the hysteresis behavior of the background signal. Considering that the background signal also coexists with the spin-torque ferromagnetic resonance spectrum, the author proposed that crosscheck using the spin-torque ferromagnetic resonance and the background signal enables more reliable estimation of the spin Hall angle. This research provides a plenty of physics and utilities of the background signal that has been neglected for a long time.

Results presented in this chapter were published in the paper:

M. Aoki, E. Shigematsu, R. Ohshima, T. Shinjo, M. Shiraishi, and Y. Ando, "Coexistence of low-frequency spin-torque ferromagnetic resonance and unidirectional spin Hall magnetoresistance", Physical Review B **104**, 094401 (2021).

3.2 Introduction and research purpose

3.2.1 Background signal

During investigation of the LFST-FMR using various kinds of NM/FM bilayer structures, the author found that the BG signal, whose polarity changes depending on the magnetization orientation, is coexisting with the LFST-FMR signal. Figure 3-1 shows MR (top panels), differential of the MR (middle panels), and V_{DC} as a function of μ_0H_{ext} (bottom panels) measured in Sample A [Pt(15)/Co(3)/SiO_2(7)] and Sample C [Ta(15)/Co(3)/SiO_2(7)] (number in bracket is the thickness in nanometer). Details of the Samples A and C are summarized in Section 3.3.1. Given that the LFST-FMR is proportional to the differential of the MR curves, V_{DC} as a function of μ_0H_{ext} should show similar behavior in both the Samples A and C based on the study of Chap. 2. However, V_{DC} shows apparently different characteristics as shown in Figs. 3-1(e) and 3-1(f). V_{DC} shows peak around zero magnetic field in the Sample A, which is similar to the shape of the differential of the MR curve shown in Fig. 3-1(c). On the other hand, large BG signal was dominant for the Sample C as shown in Fig. 3-1(f). Although small BG signal is observed in the Sample A, it shows different sign compared to that of the Sample C, indicating that the BG signal could be related to the SHA in the NM layer, because sign of the SHA of Ta is opposite to that of Pt. The purpose of this research is to investigate the origin of the BG signal.

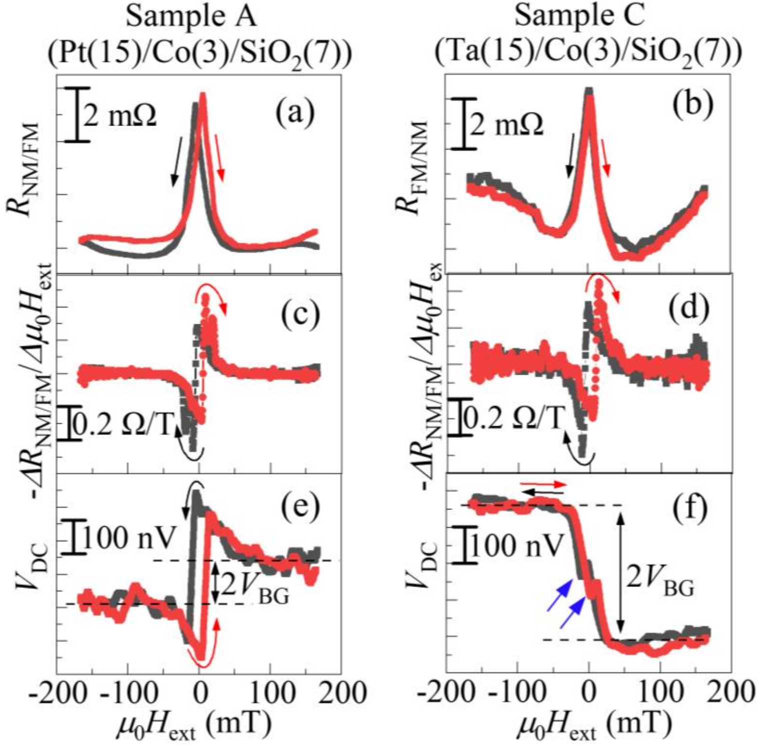

FIG. 3-1. (a)[(b)] MR curve with H_{ext} perpendicular to the electric current, (c)[(d)] differential of the MR curve, and (e)[(f)] measured DC voltage with a frequency of 100 MHz for Pt/Co (Ta/Co) bilayers. Microwave power was fixed to 5 dBm and magnetic field was applied perpendicular to the electric current.

3.2.2 Unidirectional spin Hall magnetoresistance

Possible origin of the BG signal is the USMR, in which resistance of a NM/FM bilayer, $R_{NM/FM}$, changes

depending on applied-current and magnetization directions [41]. There are two kinds of USMR, SD-USMR and spin-flip USMR (SF-USMR) [42]. The former originates from the fluctuation of the up- and down-spin populations in the FM due to the spin current injected from the NM, whereas the latter originates from electron-magnon scattering at the NM/FM interface. Given that the BG signal is independent of the magnitude of H_{ext}, SD-USMR is the most plausible origin because magnon population is suppressed as increasing H_{ext} [43].

Now, the author explains the mechanism of the SD-USMR in detail. For example, the author assumes the systems shown in Fig. 3-2(b): when electric current is applied along x direction in a NM/FM bilayer structure, spin current is generated along z direction, resulting in injection of $-y$-polarized spin (corresponding to majority-spin injection into the FM layer when the magnetization of the FM layer is along y). In this case, contribution of the majority-spin band to the electrical transport becomes enhanced. In this case, when electric current is along $-x$, contribution of the minority-spin band becomes dominant as shown in Fig. 3-2(c). Since the mobility of majority-spin electron is different from that of minority-spin electron as shown in Fig. 3-2(a), enhancement of majority-spin contribution results in, *e.g.*, larger $R_{\mathrm{NM/FM}}$, whereas enhancement of minority-spin contribution results in smaller $R_{\mathrm{NM/FM}}$ because of the difference in mobility between majority and minority spins. As a result, $R_{\mathrm{NM/FM}}$ changes depending on the polarity of the applied electric current and magnetization directions. When an AC electric current, $I_{\mathrm{rf}} = I_0 \sin 2\pi f t$, is injected, $R_{\mathrm{NM/FM}}$ is expressed as $R_{\mathrm{NM/FM}} = R_{\mathrm{NM/FM(0)}} + R_{\mathrm{USMR}} \sin 2\pi f t$, resulting in DC output voltage, $V_{\mathrm{DC}} = I_0 R_{\mathrm{USMR}}/2$, which is given by time averaging of the product of I_{rf} and $R_{\mathrm{NM/FM}}$. Since R_{USMR} depends on polarity but not on magnitude of H_{ext}, SD-USMR can be the origin of the BG signal. In the following, BG signal is measured with changing various parameters to conclude that the origin is the SD-USMR.

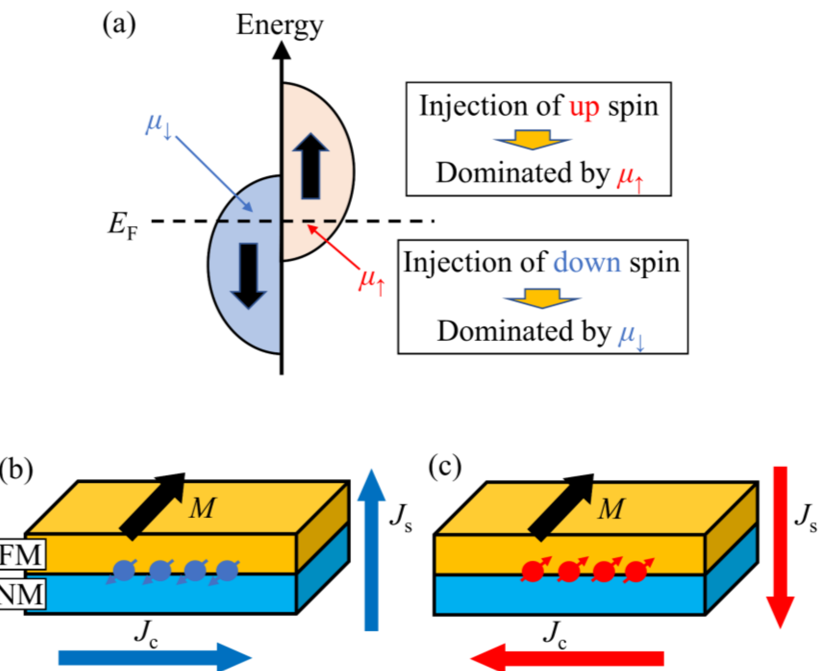

FIG. 3-2. (a) Density of states in a FM. (b, c) A NM/FM bilayer structure when electric current is applied in-plane. Sign of spin current injected into the FM layer depends on the polarity of the electric current.

3.3 Experimental setup

3.3.1 Sample fabrication

Figure 3-3 shows a schematic of the device structure. Rectangular-shaped NM (t_N nm)/Co (t_F nm)/SiO_2 (t_{cap} nm) multilayer was fabricated using EB lithography and DC magnetron sputtering. Then, Co/cap bilayer was shaped into smaller rectangular with a width, w, and length, l, by using EB lithography and Ar ion milling. After removing surface oxide layer on top of the NM layer by additional Ar ion milling, Ti (3 nm)/Au (70 nm) electrode was deposited without breaking vacuum by using EB evaporation. Six samples labeled as Sample A-F were used in this study as summarized in Table 3-1.

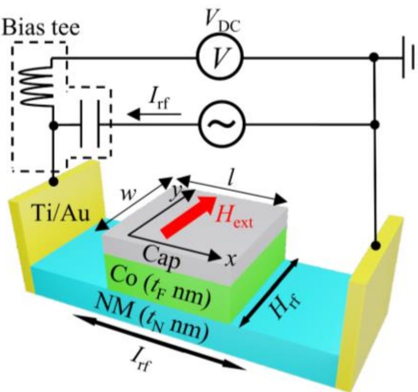

FIG. 3-3. A schematic of device structure used in this study.

Table 3-1. Summary of the device geometry of the samples used in this study.

Sample	NM	t_N (nm)	t_F (nm)	t_{cap} (nm)	w (μm)	l (μm)
A	Pt	15	3	7	5	0.8
B	Pt	15	3	7	40	40
C	Ta	15	3	7	5	1
D	Ta	15	8	7	10	1.3
E	Ta	15	3	7	40	40
F	W	6	1	3	5	5

3.3.2 Measurement setup

Microwave radiation with a power, P, was applied using a commercial signal generator (Keysight N5173B EXG) and V_{DC} was measured by a voltmeter (Keithley Nanovoltmeter 2182A). Magnetic field, H_{ext}, is applied perpendicularly to the electric current unless otherwise indicated. For demonstrating SOT-induced magnetization switching, pulse current with a width of 1 μm was injected using a function generator (Keysight 33622A). Temperature and magnetic-field angle dependences were measured in physical property measurement system (Quantum Design PPMS). In the measurement using PPMS, V_{DC} was measured using the same voltmeter as mentioned above but microwave was applied using a function generator (Keysight 33622A) with a frequency of 0.1 GHz and a voltage amplitude for generating microwave current, V_{MW}, was fixed to be 2 V peak-to-peak.

3.4 Investigation on the background signal

3.4.1 Microwave frequency dependence

Figure 3-4 shows V_{DC} as a function of $\mu_0 H_{ext}$ measured in Sample C with different microwave frequencies. When magnetic field is small, V_{DC} is significantly modulated by frequency tuning as shown in enlarged signal [Fig. 3-4(b)]. This is because of the competition between the BG signal (independent of f) and the LFST-FMR (dependent of f). Indeed, when magnetic field is large, only the BG signal survives, resulting in less modulation of V_{DC} by changing f. This trend is more clearly seen in Sample D with thicker Co thickness as shown in Fig. 3-4(c). In this case, the LFST-FMR is larger compared to Sample C and shows sign reversal of the hysteresis as decreasing microwave frequency [see Fig. 3-4(d)]. The fact that LFST-FMR and the BG signal shows different dependences on t_F indicates that the BG signal originates from the different physics other than that of the LFST-FMR.

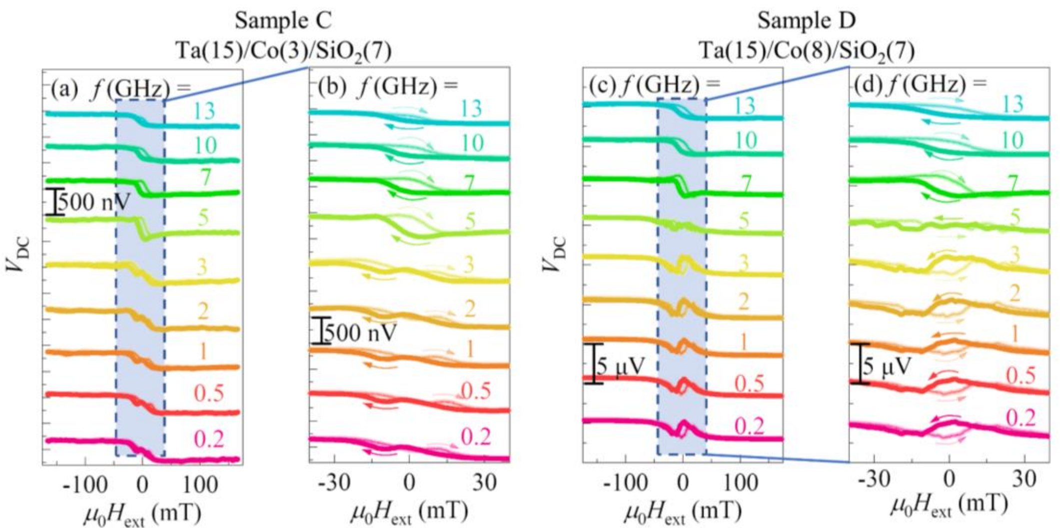

FIG. 3-4. V_{DC} as a function of H_{ext} with different frequencies of microwave for (a) Sample C and (c) Sample D. Signals enlarged around zero magnetic field are also shown in (b) and (d), respectively. P was fixed to be 5 and 10 dBm in the measurement of Sample C and D, respectively.

3.4.2 Frequency, current, temperature, and magnetic-field angle dependences

Figure 3-5(a) shows the frequency dependence of the BG signal for Sample C obtained from the spectra shown in Fig. 3-4(c). Definition of V_{BG} is shown in Figs. 3-1(e) and 3-1(f). Here, V_{BG} is normalized by the square of I_0 to consider the frequency-dependent power loss in the cable (see Appendix Section B for estimation of the frequency-dependent power loss in the cable). BG signal is found to be independent of f, which is consistent with the SD-USMR. To further verify that the origin of the BG signal is the SD-USMR, amplitude of I_0, temperature, and magnetic-field angle dependences were investigated. Figure 3-5(b) shows I_0 dependence of the BG signal for Sample C. V_{BG} was proportional to the square of I_0, which is consistent with the characteristics of the rectification signals. The author also measured the temperature dependence of the BG signal because the SD-USMR shows weaker temperature dependence than the SF-USMR [42]. Red circles in

Fig. 3-5(c) shows temperature dependence of V_{BG} measured for Sample E. Although slight enhancement of V_{BG} was observed at lower temperatures, modulation was much less than that of the SF-USMR shown in ref. [42]. Finally, the author investigated magnetic-field angle dependence of the BG signal because SD-USMR is proportional to the *y* component of the magnetization. Magnetic field was rotated in *xy*, *zx*, and *yz* scans as shown in Fig. 3-5(d). In this case, V_{BG} is expected to depend only on α and γ. Figure 3-5(e) shows V_{BG} as functions of α, β, and γ for Sample E. Black lines indicate expected angular dependences of the *y* component of the magnetization. The black line is simply a sine function in case of *xy* scan. On the other hand, it was calculated by MuMax3 in case of *yz* scan to consider large IP magnetic anisotropy. Measured signals well correspond to the black lines, indicating the BG signal is proportional to the *y* component of the magnetization. All these results are consistent with the scenario that the BG signal is generated by the SD-USMR.

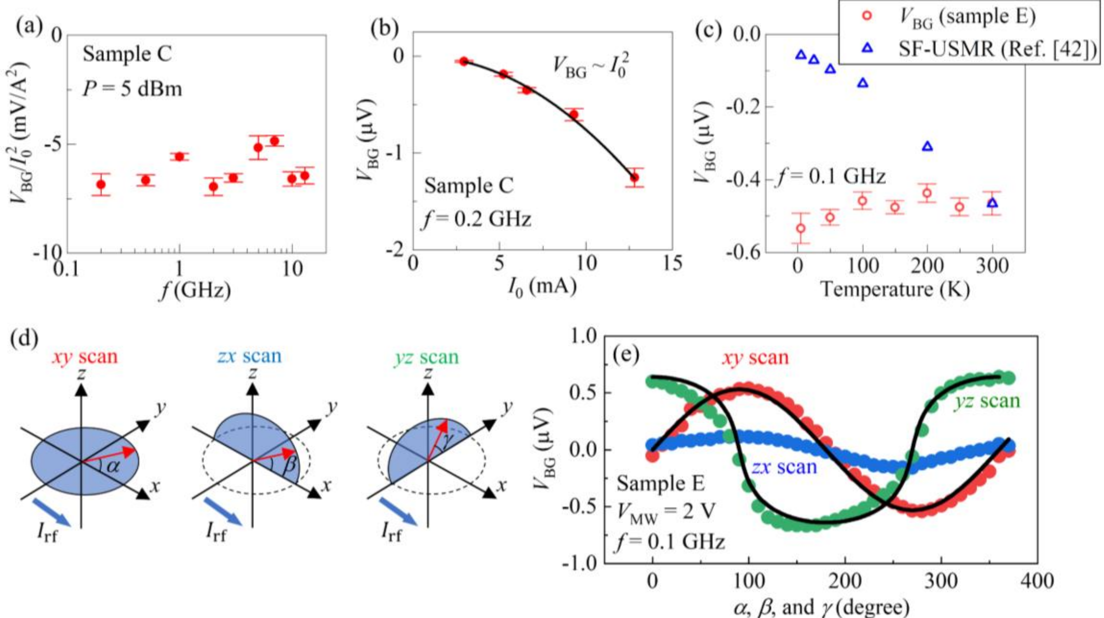

FIG. 3-5. (a) Microwave frequency and (b) electric current dependence of the BG signal for sample C. (c) Temperature dependence of the BG signal for Sample E compared with that of the SF-USMR. (d) Schematics of the measurement of magnetic-field angle dependence and (e) signal observed in each scan for Sample E.

3.4.3 Contribution from the anomalous Nernst effect

One might think that the ANE [24] induced by OOP thermal gradient might cause V_{BG} [23]. As for sign reversal of the BG signal between Ta/Co/SiO_2 and Pt/Co/SiO_2, large difference in resistivity between Ta and Pt might cause different distribution of electric current and sign reversal of the thermal gradient. Therefore, the author measured the BG signal of Cu/Co/SiO_2. Since the resistivity of Cu is much smaller than Ta and even smaller than Pt, and SHE is negligibly small, BG signal in this Cu/Co/SiO_2 should show the same sign as that of Pt/Co/SiO_2 based on the ANE scenario. However, sign of the BG signal is the same as that of Ta/Co/SiO_2 as shown in Fig. 3-6, where f = 200 MHz, P = 5 dBm, l = 800 nm, and w = 5 μm. Therefore, ANE cannot explain

the sign reversal of the BG signal between Pt/Co/SiO_2 and Ta/Co/SiO_2. The author also simulated thermal gradient induced by Joule heating using COMSOL Multiphysics [44,45]. Figure 3-7(a) shows a schematic of the simulation. Electric current was applied in NM/FM/SiO_2 multilayers on the MgO substrate along IP direction and thermal gradient is produced along z direction due to Joule heating. Parameters used in simulation are shown in Table 3-1. Figures 3-7(b)-3-7(d) show temperature as a function of z when Ta, Pt, or Cu is used as a NM layer, respectively. Temperature at the top interface of Co is higher than that at the bottom interface for all devices, meaning that sign of ANE signal does not change depending on NM materials. Temperature difference between top and bottom interface of Co is 0.06 mK, 0.11 mK, and 0.03 mK for Ta, Pt, or Cu, respectively. Using ANE coefficient of Co, $a_N = -1.7 \times 10^8$ A/(m$^2 \cdot$ K) [46], BG signal generated by the SD-USMR in Samples B and E are estimated to be 118 % (72 %) of the measured BG signal. Although contribution from the ANE is not negligible, SD-USMR is the dominant contributor to the BG signal in Pt/Co/SiO_2 and Ta/Co/SiO_2.

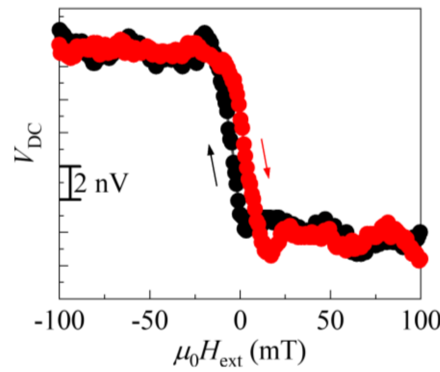

FIG. 3-6. V_{DC} as a function of $\mu_0 H_{ext}$ for Cu/Co/SiO2 structure.

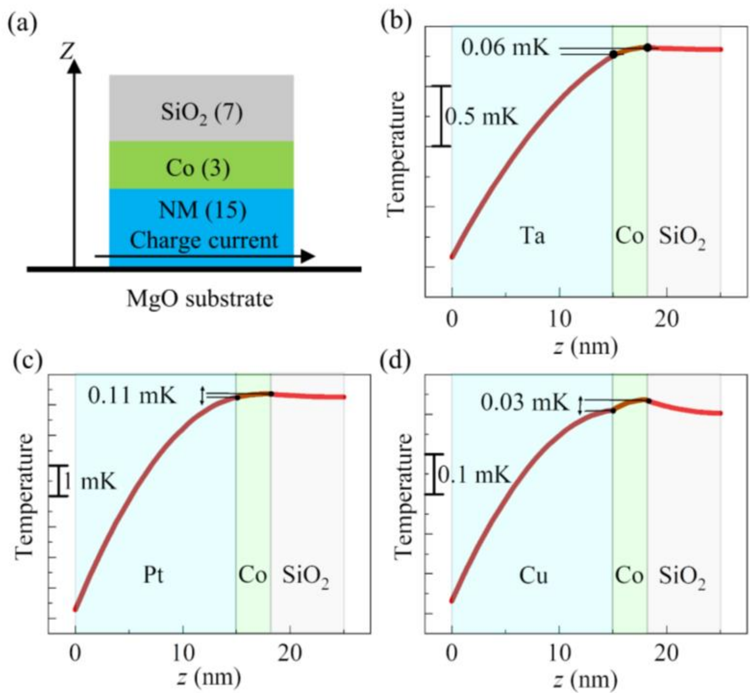

FIG. 3-7. (a) A schematic of the simulation for calculating temperature distribution induced by Joule heating. (b) Calculated temperature distribution for Ta/Co/SiO_2, (c) Pt/Co/SiO_2, and (d) Cu/Co/SiO_2 samples.

Table 3-1. Parameters used in the simulation of temperature gradient.

Material	Resistivity $(\Omega \cdot \mathrm{m})$	Density $(\times 10^3 \mathrm{kg/m^3})$	Specific heat capacity $(\mathrm{J/(kg \cdot K)})$	Thermal conductivity $(\mathrm{W/(m \cdot K)})$
MgO	1.00×10^{20}	1.77	1000	50
SiO_2	1.00×10^{10}	2.33	1052	1.4
Co	9.82×10^{-7}	8.90	420	70
Pt	5.15×10^{-7}	21.09	133	72
Ta	2.32×10^{-6}	16.65	140	57
Cu	2.40×10^{-7}	8.94	379	401

3.5 Utilization of the background signal

3.5.1 Estimation of the spin Hall angle

Given that the SD-USMR is produced by the SHE in the NM layer, SHA of the NM layer can be estimated from the value of the BG signal. According to Zhang and Vignale [47], magnetoresistance induced by the SD-USMR, R_{USMR}, is derived from the spin diffusion model as,

$$R_{\mathrm{USMR}} = 3\left(\frac{\sigma_{\mathrm{F}} L_{\mathrm{F}}}{\sigma_{\mathrm{N}} t_{\mathrm{N}} + \sigma_{\mathrm{F}} t_{\mathrm{F}}}\right) \times \frac{(p_\sigma - p_{\mathrm{N}})\left[\left(\frac{\theta_{\mathrm{SH}} L_{\mathrm{N}}}{\varepsilon_{\mathrm{F}}}\right)\tanh\left(\frac{t_{\mathrm{N}}}{2L_{\mathrm{N}}}\right)\tanh\left(\frac{t_{\mathrm{F}}}{L_{\mathrm{F}}}\right)\right]}{1 + (1 - p_\sigma^2)\left(\frac{\sigma_{\mathrm{F}} L_{\mathrm{N}}}{\sigma_{\mathrm{N}} L_{\mathrm{F}}}\right)\tanh\left(\frac{t_{\mathrm{F}}}{L_{\mathrm{F}}}\right)\coth\left(\frac{t_{\mathrm{N}}}{L_{\mathrm{N}}}\right)} \frac{I R_{\mathrm{NM/FM}}}{l}, \quad (3\text{-}1)$$

where σ_{F} (σ_{N}) and L_{F} (L_{N}) are conductivity and spin-diffusion length of the FM (NM), p_σ is conductivity spin asymmetry, p_{N} is the difference in density of states at the Fermi energy between up and down spins, ε_{F} is the Fermi energy of the FM, and θ_{SH} is the SHA of the NM layer. When $I_{\mathrm{rf}} = I_0 \sin 2\pi f t$ is applied, BG signal generated by the SD-USMR is given by,

$$V_{\mathrm{USMR}} = V_{\mathrm{BG}} - V_{\mathrm{ANE}} = \frac{3R_{\mathrm{NM/FM}}^2}{2l}\left(\frac{\sigma_{\mathrm{F}} L_{\mathrm{F}}}{\sigma_{\mathrm{N}} t_{\mathrm{N}} + \sigma_{\mathrm{F}} t_{\mathrm{F}}}\right) \times \frac{(p_\sigma - p_{\mathrm{N}})\left[\left(\frac{\theta_{\mathrm{SH}} L_{\mathrm{N}}}{\varepsilon_{\mathrm{F}}}\right)\tanh\left(\frac{t_{\mathrm{N}}}{2L_{\mathrm{N}}}\right)\tanh\left(\frac{t_{\mathrm{F}}}{L_{\mathrm{F}}}\right)\right]}{1 + (1 - p_\sigma^2)\left(\frac{\sigma_{\mathrm{F}} L_{\mathrm{N}}}{\sigma_{\mathrm{N}} L_{\mathrm{F}}}\right)\tanh\left(\frac{t_{\mathrm{F}}}{L_{\mathrm{F}}}\right)\coth\left(\frac{t_{\mathrm{N}}}{L_{\mathrm{N}}}\right)} I_0^2. \quad (3\text{-}2)$$

The values of V_{BG} measured in Samples B and E were 67 ± 15 nV and − 460 ± 70 nV, respectively. Substituting the value of the BG signal after eliminating the ANE voltage, V_{ANE} (see Section 3.4.3 for detail), θ_{SH} of Ta and Pt were estimated to be −0.084 and 0.052, respectively, both of which are consistent with precious research. Given that the BG signal coexists with the ST-FMR signal that is widely used for estimating the SHA, BG signal can be used as an effective crosscheck of the ST-FMR method and enable more reliable estimation of the SHA. Values used for this estimation are shown as following: $\sigma_{\mathrm{F}} = 1.01 \times 10^6\ (\Omega \cdot \mathrm{m})^{-1}$ (measured), $\sigma_{\mathrm{Pt}} = 1.94 \times 10^6\ (\Omega \cdot \mathrm{m})^{-1}$ (measured), $\sigma_{\mathrm{Ta}} = 4.32 \times 10^5\ (\Omega \cdot \mathrm{m})^{-1}$ (measured), $L_{\mathrm{F}} = 40$ nm [48], $L_{\mathrm{Pt}} = 14$ nm [49], $L_{\mathrm{Ta}} = 1.8$ nm [49], $p_\sigma - p_{\mathrm{N}} = 0.5$ [47], and $\varepsilon_{\mathrm{F}} = 5$ eV [47].

3.5.2 Detection of the spin-orbit torque magnetization switching

In this section, detection of SOT-induced switching is demonstrated in the same manner as shown in Fig. 2-

10 but using the BG signal instead of the LFST-FMR. W (6 nm)/Co (1 nm)/SiO_2 (3 nm) multilayer (Sample F) was used in this experiment. Large negative SHE in W is expected to realize pure-SOT switching because the switching direction due to SOT and Oersted field is opposite to each other in this geometry [27]. Figure 3-8(a) shows schematics of the device structure and measurement circuit. Left panels of Figs. 3-8(b) and 3-8(c) show V_{DC} as a function of $\mu_0 H_{ext}$ with a microwave frequency of 0.2 GHz and 13 GHz, respectively. Offset voltage with a polarity depending on direction of H_{ext} was observed even at 13 GHz, indicating existence of the BG signal. The right panels of Figs. 3-7(b) and 3-7(c) show SOT switching signal detected using the BG signal when $f = 0.2$ and 13 GHz, respectively. Switching signals as large as that of the hysteresis of the BG signal were successfully obtained in both cases. In addition, threshold current density, 3×10^7 A/cm^2, is consistent with the previous research [27]. From these results, the author proposes that the BG signal can be used for probing the SOT-induced switching in the same manner as that using the LFST-FMR.

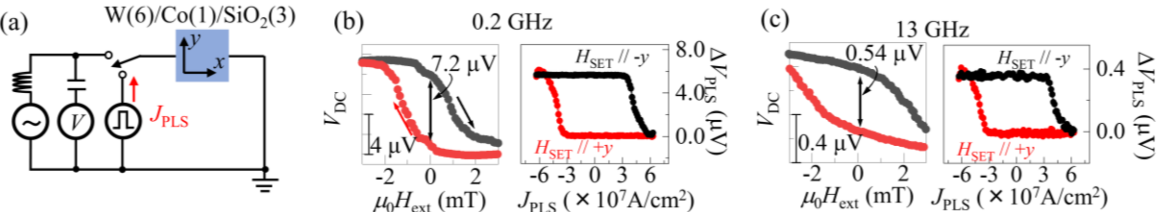

FIG. 3-8. (a) A schematic of the device structure for demonstration of SOT-induced magnetization switching. (b, c) (left panel) V_{DC} as a function of $\mu_0 H_{ext}$ and (right panel) SOT-induced switching detected by using the BG signal with a microwave frequency of (b) 0.2 GHz and (c) 13 GHz.

3.6 Summary

To summarize, the author verified that the origin of the background signal coexisting with the spin-torque ferromagnetic resonance and low-frequency spin-torque ferromagnetic resonance is spin-dependent unidirectional spin Hall magnetoresistance by measuring nonmagnetic material, frequency, current, magnetic-field angle, and temperature dependences. By using the background signal, estimation of the spin Hall angle and detection of spin-orbit torque magnetization switching were demonstrated. To note is that the background signal coexists with the spin-torque ferromagnetic resonance spectrum, which has been widely used for estimating the spin Hall angle since 2011 [21]. Despite the fact, the background signal has been neglected for a long time, *i.e.*, the background signal has simply been considered as an offset voltage in the spin-torque ferromagnetic resonance. The importance of this work is to find out a plenty of physics and utilities in such a simple offset signal.

Chapter 4. Spin-orbit torque magnetization switching using two current pulses

4.1 Abstract

Spin-orbit torque magnetoresistive random access memory is classified into two in viewpoint of the magnetic anisotropy of the ferromagnet layer, in-plane and out-of-plane magnetic anisotropies. Spin-orbit torque magnetoresistive random access memory with an out-of-plane ferromagnet has advantage of device integration. However, external magnetic field is required to realize deterministic magnetization switching. Spin-orbit torque magnetoresistive random access memory with an in-plane ferromagnet does not require external magnetic field in the switching process. However, switching speed is much longer than the one using out-of-plane ferromagnet. For realization of the spin-orbit torque magnetoresistive random access memory, either field-free switching of the out-of-plane ferromagnet or fast switching of the in-plane ferromagnet is needed to be realized.

In this chapter, the author demonstrates ultrafast spin-orbit torque switching of the in-plane ferromagnet by using two current pulses applied perpendicularly to each other. Switching speed was reduced from 10 ns to 300 ps by using the two-pulse method. Moreover, power consumption in the writing process was also found to be quite low. In addition, the author demonstrated analog control of the magnetization by controlling the vector of the spin polarization injected into the ferromagnet layer using two-pulse injection, which can realize neuromorphic computer using spintronics technology. This research shows a great potential of the two-pulse method for ultrafast spin-orbit torque magnetoresistive random access memory and a novel device such as a neuromorphic computing. Therefore, two-pulse method will contribute to the development of computer industry using spintronics.

4.2 Introduction and research purpose

4.2.1 In-plane and out-of-plane magnetoresistive random access memories

SOT-MRAM is classified into two in viewpoint of anisotropy of the FM electrode [50]. One uses a FM electrode with OOP magnetic anisotropy as shown in Fig. 4-1(a) [18]. Since the DL-SOT, τ_{DL}, is given by $\boldsymbol{M} \times (\boldsymbol{m} \times \boldsymbol{M})$, spin current generated by the SHE efficiently gives torque on the magnetization because $\boldsymbol{m} \times \boldsymbol{M}$ is always non-zero. Here, $\boldsymbol{M}$ and $\boldsymbol{m}$ are magnetization of the FM and magnetic momentum of injected spin, respectively. However, external magnetic field is needed for deterministic switching from $+z$ to $-z$ or $-z$ to $+z$, which is a serious disadvantage for practical application. The other type of SOT MRAM uses a FM electrode with IP magnetic anisotropy as shown in Fig. 4-1(b) [8], as is used in Sections 2 and 3. Since $\boldsymbol{m} \times \boldsymbol{M}$ is, in principle, zero in the beginning of the switching process, it takes much longer time. However, external magnetic field is not needed because injected spin is parallel or antiparallel to the magnetization axis.

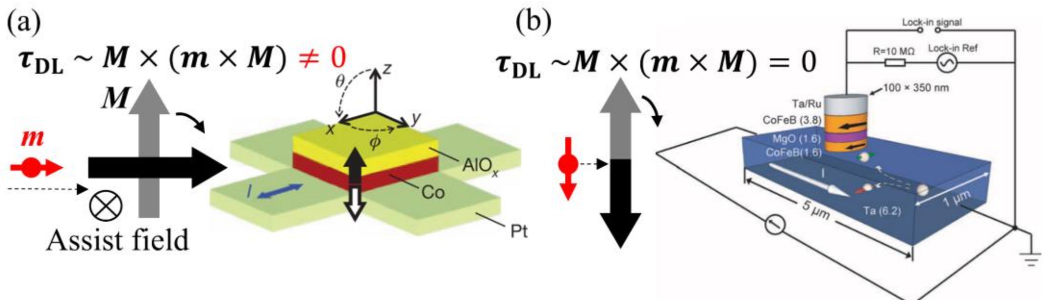

FIG. 4-1. (a) Schematics of the device structure and SOT acting on magnetization for OOP MRAM and (b) IP MRAM. **Schematics of the device structure are adapted from:** I. M. Miron *et al.*, Nature **476**, 189 (2011) [18] and L. Liu *et al.*, Science **336**, 555 (2012) [8], respectively.

4.2.2 Mechanism of two-pulse switching

To overcome the difficulty of the SOT switching of the IP FM, *i.e.*, low switching speed, the author suggested to use two different spin currents as shown in Fig. 4-2. First, spin current with a magnetic momentum of spin, $\boldsymbol{m}$, is injected. The first spin current gives torque on the magnetization efficiently and tilts magnetization from $\boldsymbol{M}$ to $\boldsymbol{M'}$. Then, spin current with a magnetic momentum of spin, $\boldsymbol{m'}$, is injected and efficiently rotates magnetization to the final state. Since τ_{DL} always acts on magnetization efficiently, ultrafast SOT switching can be realized. The purpose of this research is to realize both field-free and fast magnetization switching by using the two-pulse method.

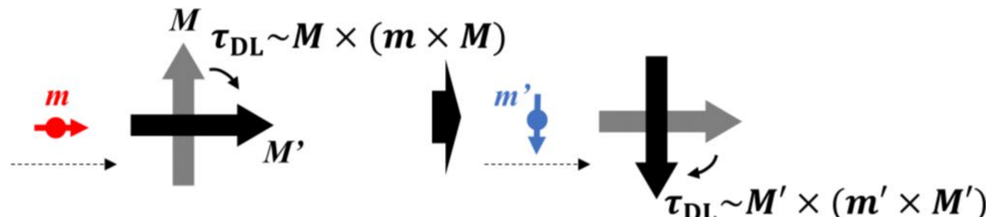

FIG. 4-2. A schematic of magnetization reversal using two current pulses.

4.3 Experimental setup

4.3.1 Sample fabrication

Figure 4-3 shows device structure and measurement circuit used in this study. A crossbar made of Ti (2 nm)/Pt (15 nm)/Py (4 nm)/MgO (2 nm) multilayer was fabricated using EB lithography and EB evaporation. Then SiO_2 capping layer was deposited by DC magnetron sputtering. FM electrode with a size of 500 nm × 2 μm was fabricated using EB lithography and Ar ion milling. Finally, coplanar wave guide composed of Ti (3 nm)/Au (70 nm) was fabricated using EB lithography and EB evaporation.

4.3.2 Measurement setup

SOT-induced switching was measured using the LFST-FMR method, which is shown in Chap. 2. Microwave with a frequency of 100 MHz and amplitude of 1 V peak-to-peak was applied using a function generator (Agilent 33622A). LFST-FMR signal was detected using a nanovoltmeter (Keithley Nanovoltmeter 2182A). A pulse generator (Active Technologies PG1072) was used to inject ultrafast pulse currents. Two pulse currents, assist pulse (width: w_a, amplitude: V_a) and main pulse (width: w_m, amplitude: V_m), were injected from channel 1 and channel 2, respectively. Interval between two pulse currents was also changed.

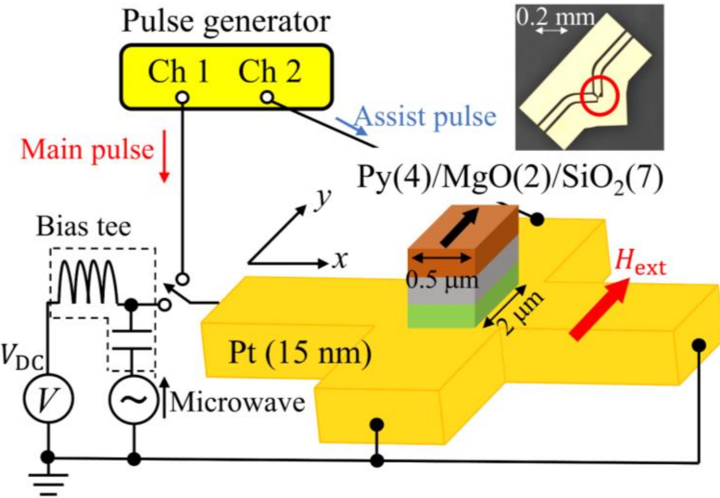

FIG. 4-3. Schematics of the device structure and measurement circuit. Picture of the device is also shown in the inset.

4.4 Demonstration of two-pulse magnetization switching

4.4.1 Interval and assist pulse dependences

Figure 4-4(a) shows colormap obtained from the SOT switching measurement, where both V_m and interval were swept. Here, w_a and w_m were fixed to be 1 ns and V_a was fixed to be 2 V. Red area means finite difference between the value of V_{DC} via the LFST-FMR before and after injecting pulse currents, *i.e.*, successful SOT switching. It was found that the threshold value of V_m was lowest when interval is zero. Also, SOT switching was successfully observed even when w_a and w_m were reduced to 300 ps as shown in Fig. 4-4(b). Figure 4-5

shows colormap obtained from the SOT-switching measurement, where both V_m and V_a were swept. Here, w_a and w_m were fixed to be 1 ns and interval was fixed to be 0 ns. There is a relationship between threshold value of V_m, $V_{m(th)}$, and V_a as $V_a = -0.7V_{m(th)} + 2.7$. Using this relationship, power consumption in the SOT switching was found to be lowest when (V_m, V_a) = (1.3 V, 1.8 V).

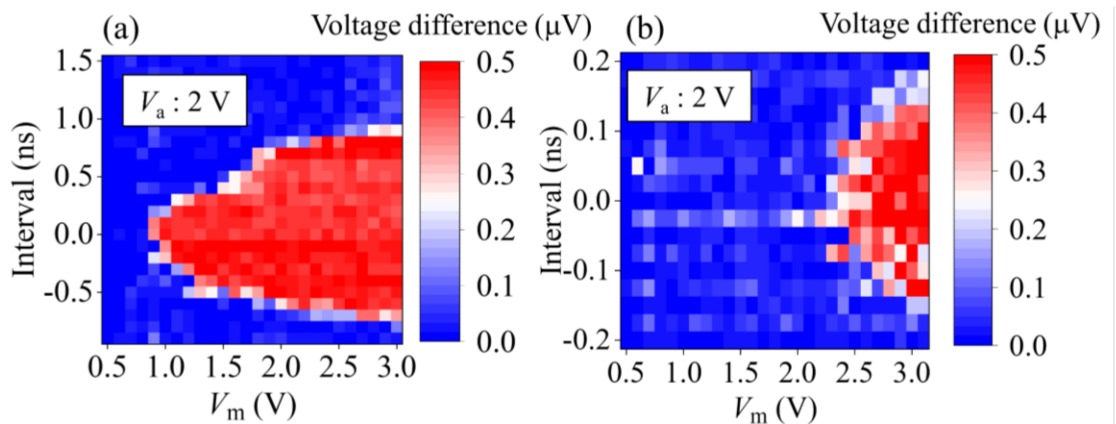

FIG. 4-4. (a) Switching signal as functions of V_m and interval when $w_a = w_m = 1$ ns and (b) 300 ps. Red region represents successful magnetization switching.

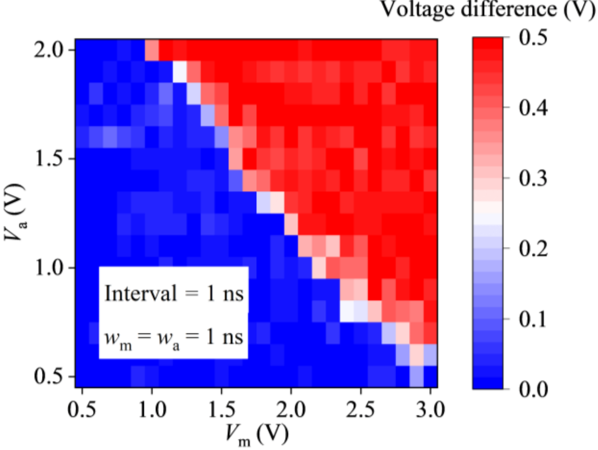

FIG. 4-5. Switching signal as functions of V_a and V_m. Red region represents successful magnetization switching.

4.4.2 Assist pulse width dependence

In Section 4.4.1, the author found that SOT switching becomes most efficient when two pulse currents are injected at the same time. Given that the role of assist pulse is to tilt magnetization from the initial state but not complete magnetization switching, it is expected that threshold value of V_m does not change even when w_a is shortened. Figure 4-5(a) shows colormap obtained from the SOT switching measurement, where both V_m and w_a were swept. Interval, w_m, and V_a were fixed to be 0 ns, 1 ns, and 2 V, respectively. Threshold value of V_m does not change even when w_a is reduced to 0.5 ns. Figure 4-5(b) shows colormap of the y component of the magnetization as functions of w_a and current density of the main pulse, j_x, calculated by Assoc. Prof. Syuta

Honda at Kansai University. Current density of the assist pulse, j_y, interval, and w_m were fixed to be 16 MA/cm^2, 0 ns, and 1 ns, respectively. Threshold value of j_x does not change even if w_a is reduced to 0.5 ns, which is consistent with the experiment. Threshold value of j_x increases with decreasing w_a below 0.5 ns, however, it is clearly reduced at around w_a = 0.2 ns. Although this behavior could not be observed due to experimental limitation, simulated result indicates that w_a can be further reduced to a few tens of picoseconds and power consumption can be reduced by minimizing w_a. In this sense, two-pulse method has advantage of lower power consumption over type X switching with tilted easy axis [51].

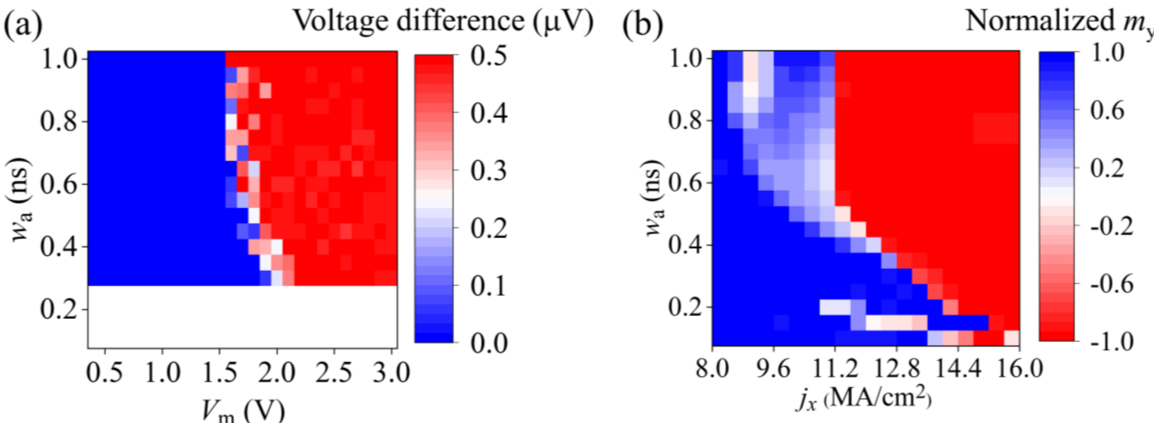

FIG. 4-5. (a) Switching signal as functions of w_a and V_m. Red region represents successful magnetization switching. (b) Calculation of magnetization switching using two-pulse method. w_a and j_x were swept, whereas j_y, interval, and w_m were fixed to be 16 MA/cm^2, 0 ns, and 1 ns, respectively.

4.4.3 Comparison with one-pulse method

As discussed above, the switching speed of two-pulse method is much faster than that of conventional one-pulse method only using the main pulse. Figure 4-6 shows comparison of the SOT switching measured by the LFST-FMR method between one-pulse method with w_m = 10 ns or 1 ns, and two-pulse method with $w_a = w_m$ = 1 ns, interval = 0 ns, and V_a = 2 V. In one-pulse method, SOT switching was realized when w_m = 10 ns. However, no switching signal was observed when w_m = 1 ns. On the other hand, SOT switching was realized with smaller threshold value of V_m even when $w_a = w_m$ = 1 ns. Power consumption of one-pulse method (w_m = 10 ns) needed for SOT switching was calculated to be 755 pJ. On the other hand, that of two-pulse method ($w_a = w_m$ = 300 ps) was calculated to be 51 pJ, which is smaller than one-pulse method by more than an order of magnitude. If we assume practical MRAM device with a typical cell size of 100 nm^2, power consumption of two-pulse method is estimated to be 2.71 fJ/bit. This value is as

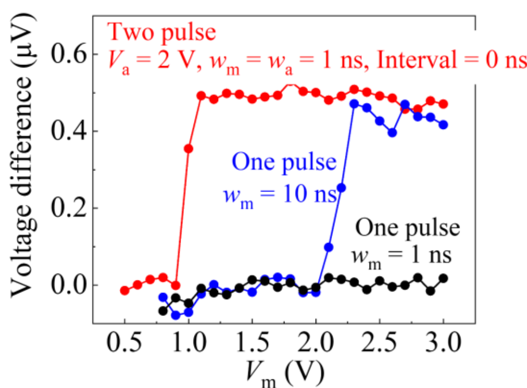

FIG. 4-6. Switching signals observed in two- and one-pulse methods as a function of V_m.

small as that of dynamic random access memory [52], which is widely used as a main memory of computer. Therefore, the author suggests that two-pulse method can be a possible candidate for an energy-efficient writing process of SOT-MRAM.

4.4.4 Micromagnetic simulation

To unveil the origin of ultrafast switching, micromagnetic simulation was carried out in collaboration with Assoc. Prof. Syuta Honda at Kansai University. In the simulation, spin current with a current density of 12 MA/cm^2 was injected into a FM electrode with the same geometry as the experiment. Damping coefficient, exchange stiffness, spin diffusion length, and saturation magnetization of the FM layer is set to be 0.02, 13 pJ/m, 2 nm, and 0.46 MA/m, respectively. Figs. 4-7(a) and 4-7(b) show time evolution of the y component of the magnetization for one-pulse and two-pulse methods, respectively. Switching process takes 7 ns for one-pulse method, whereas switching is completed within 2 ns in two-pulse method. Figures 4-7(c) and 4-7(d) show time evolution of the magnetic momentum during the switching for one-pulse and two-pulse methods, respectively. Arrows in color indicate the vector of the magnetic moment. As usually seen in the IP magnetization switching process, domain wall was nucleated in one-pulse method. On the other hand, magnetization motion during switching is much more uniform in two-pulse method. Such macro-spin-like behavior in two-pulse method enables ultrafast SOT switching.

4.5 Control of magnetization utilizing two-pulse method

4.5.1 Analog rotation of magnetization

In Section 4.4, uniaxial magnetic anisotropy was introduced in the FM electrode by shaping it into a rectangular. Since spin polarized along "any" direction can be injected by using the two-pulse method, direction of magnetization can be switched along any direction if the uniaxial magnetic anisotropy of the FM electrode is removed. To demonstrate such analog writing process, FM electrode was shaped into snow-crystal structure and injected-spin direction was controlled by two-pulse method as shown in Fig. 4-8(a). Figures 4-8(b) and 4-8(c) show V_{DC} generated by the LFST-FMR signals as a function of the angle between x and vector sum of electric current, θ, detected by applying microwave along x and y directions, respectively. Magnitude of pulse voltage, $\sqrt{V_a^2 + V_m^2}$, is fixed to be 3 V and pulse width was fixed to be 20 ns. When V_{DC} was detected by microwave along x and y, cosine-like and sine-like signals were observed. This is because the former and latter corresponds to y and x component of the magnetization of the FM layer and spin current with a magnetic momentum of spin along $\theta - 90°$ is injected when vector sum of electric current is along θ. Therefore, clear sine-like and cosine-like signals indicate magnetization can be controlled along any direction. Based on these results, the author proposes that two-pulse method can also be used as novel SOT devices utilizing analog manipulation of magnetization such as a neuromorphic computing.

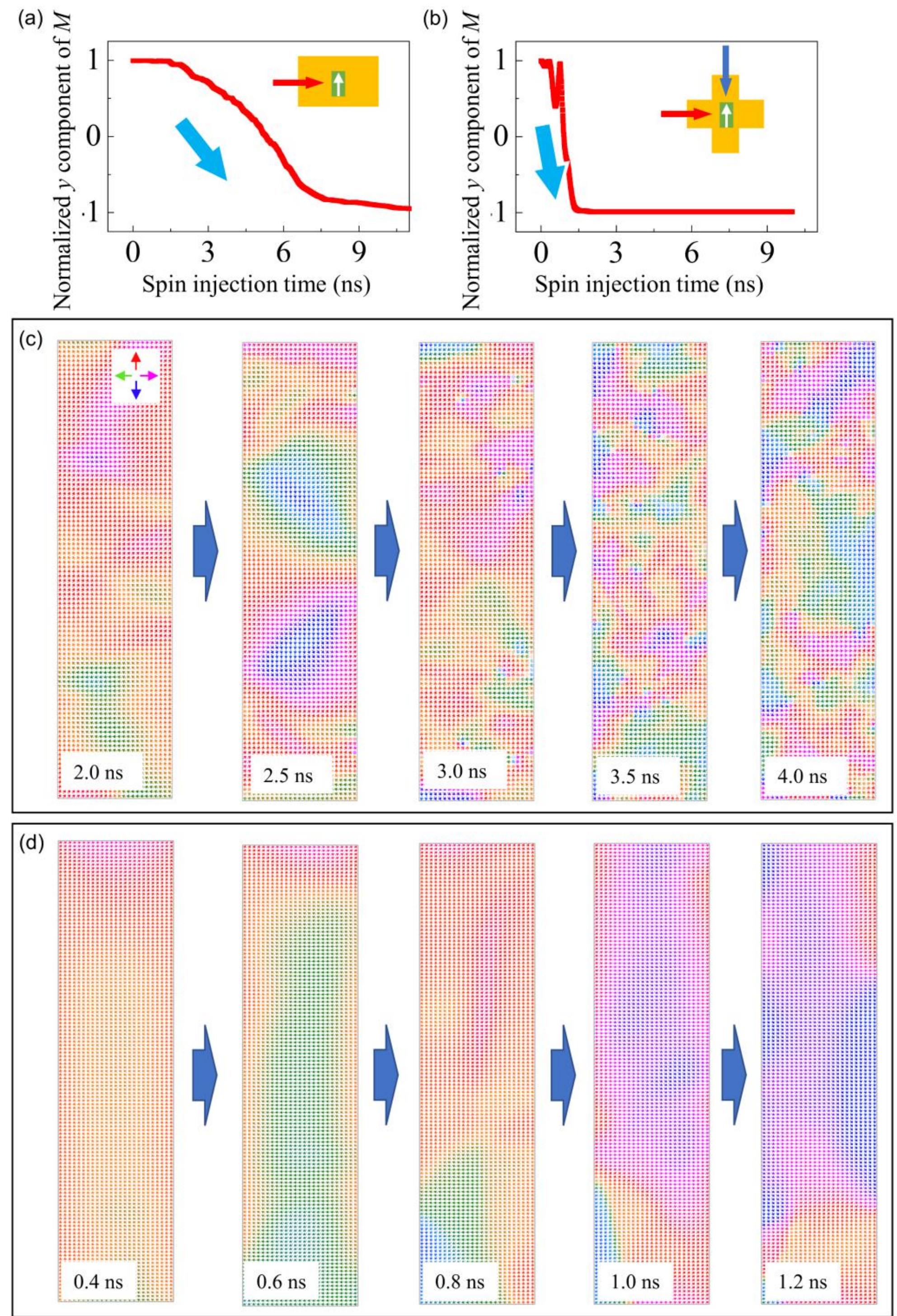

FIG. 4-7. (a) Time evolution of the *y* component of the magnetization in one-pulse method and (b) two-pulse method. (c) Spatial decomposition of the switching process in one-pulse method and (d) two-pulse method.

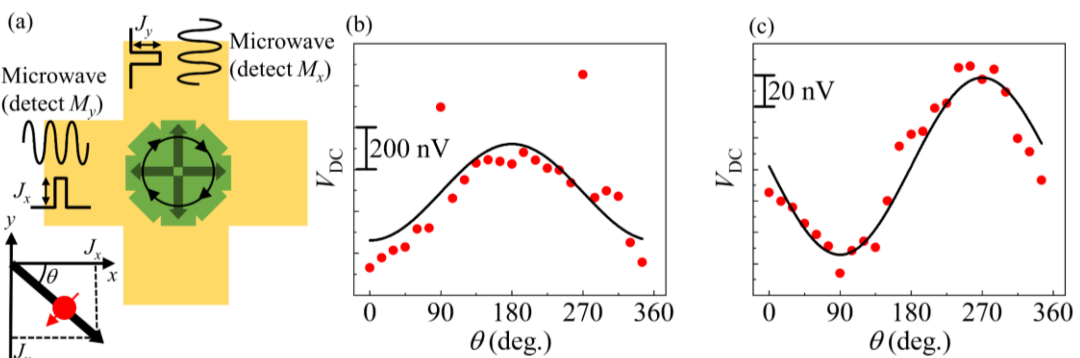

FIG. 4-8. (a) A schematic of the analog switching using two-current pulses. (b,c) V_{DC} detected along (b) x axis (indicating M_y) and (c) y axis (indicating M_x).

4.6 Summary

The author demonstrated ultrafast spin-orbit torque magnetization switching by using two-pulse method. Magnetization of permalloy was successfully switched even within 300 ps. Power consumption for writing process of spin-orbit torque magnetoresistive random access memory was significantly reduced by more than one order of magnitude. In addition, analog control of magnetization orientation was realized by controlling vector of the electric current and resulting injected-spin polarization, which will contribute to the progress of neuromorphic computing using magnetization of ferromagnet.

Chapter 5. Current-induced out-of-plane torque in a single permalloy layer controlled by electrode structure

5.1 Abstract

Spin-orbit torque magentoresistive random access memory using a ferromagnetic layer with out-of-plane magnetic anisotropy has advantage of device integration. However, in addition to spin-orbit torque, external magnetic field is needed for deterministic switching, which is a serious disadvantage for practical applications. For realizing deterministic switching of the out-of-plane ferromagnet, inversion symmetry breaking along in-plane direction has been focused on these days because this causes current-induced out-of-plane spin generation in a similar manner as the Rashba-Edelstein effect and switches magnetization of the out-of-plane ferromagnet deterministically. So far, material with broken inversion symmetry [30,53,54], interlayer with a thickness gradient [55], and lateral gate application [56] have been proposed. However, applying above methods to a practical device with a size of less than 100 nm is challenging.

In this chapter, the author investigates the torque acting on the magnetization when the electric current is nonuniform due to asymmetric electrode structure. Surprisingly, current-induced torque with the same symmetry as the spin-orbit torque generated by the out-of-plane spin injection was observed. From the frequency dependence, the current-induced out-of-plane torque observed in this experiment was found to be due to the out-of-plane inductive field. The author demonstrated that such "pseudo" out-of-plane torque can realize field-free switching of the ferromagnet with out-of-plane magnetic anisotropy using micromagnetic simulation. Since fabricating asymmetric electrode is versatile, this method can easily be applicable even to practical devices.

Results presented in this chapter were published in the paper:

M. Aoki, E. Shigematsu, R. Ohshima, T. Shinjo, M. Shiraishi, and Y. Ando, "Current-induced out-of-plane torques in a single permalloy layer with lateral structural asymmetry", Physical Review B **105**, 144407 (2022).

5.2 Introduction and research purpose

5.2.1 Symmetry and spin-orbit torque

Inversion symmetry plays an important role in charge-to-spin conversion. One typical example is the REE [5], schematic of which is shown in Fig. 1-4. In a system with a broken inversion symmetry like interface between two different materials, electromotive force exists due to the difference in work functions. This corresponds to accumulations of negative or positive charge at one side of the interface. When an electron flows IP at the interface, it feels that accumulated charge at the interfaces is flowing back, *i.e.*, effective electric current. Qualitatively, charge-to-spin conversion is explained by the spin polarization owing to the magnetostatic energy caused by an effective Oersted field generated by the effective electric current.

5.2.2 Generation of out-of-plane torque

Mechanism of the REE is applicable to the system where IP inversion symmetry is broken. In this case, charge-to-spin conversion produces OOP spin polarization, which enables field-free magnetization switching of a FM with OOP magnetic anisotropy. Therefore, tremendous efforts have been made to realize efficient OOP spin generation by introducing broken IP inversion symmetry such as wedge structure [Fig. 5-2(a)] [55] and/or transition metal dichalcogenide (TMD) [Fig. 5-2(b)] [30].

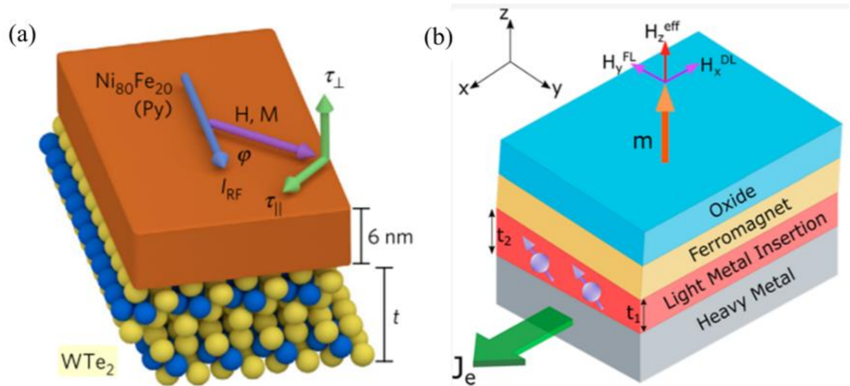

FIG. 5-1. Schematics of the structure enabling current-induced out-of-plane spin generation. (a) Application of material with broken inversion symmetry. (b) Insertion of intermediate layer with a thickness gradient. **Schematics of the device structure are adapted from:** D. MacNeill *et al.*, Nat. Phys. **13**, 300 (2017) [30] and A. Razavi *et al.*, Nano Lett. **20**, 3703 (2020) [55], respectively.

5.3 Experimental setup

5.3.1 Sample fabrication

Motivated by previous research on the OOP spin generation by breaking IP inversion symmetry, the author fabricated Py (5.5 nm)/AlO_x (t nm) layers connected with asymmetric electrodes. Figures 5-2(a) and 5-2(b) show side and top views of the device structure used in this study. Py/AlO_x layer deposited by EB deposition was shaped into a rectangular. IP inversion symmetry was intentionally broken by making the distance between

two Ti (3 nm)/Au (50 nm) electrodes (fabricated by EB deposition) at one side different from that at the other side. Here, distance between two electrodes at sides of the Py/AlO_x channel is defined as l_1 and l_2, and parameter indicating electrode's asymmetry is defined as $\Delta l = l_2 - l_1$ as shown in Fig. 5-2(b). Since the flow of electric current is asymmetric, OOP spin polarization and resulting OOP DL torque might be observed.

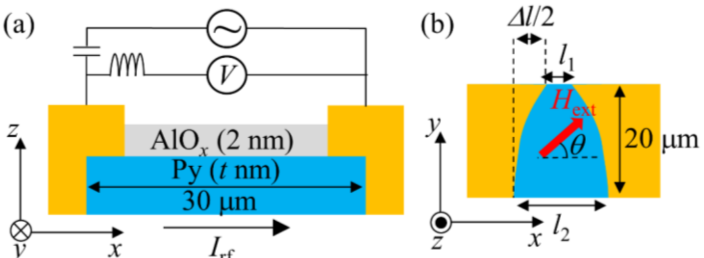

FIG. 5-2. (a) Top and (b) side views of the device structure.

5.3.2 Measurement setup

ST-FMR method was used in this study to observe the OOP DL torque. Microwave was irradiated using an analog commercial generator (Keysight N5173B EXG). Rectified DC voltage, V_{DC}, was measured using a nanovoltmeter (Keithley Nanovoltmeter 2182A) via bias tee. External magnetic field, H_{ext}, was applied with an angle, θ, as shown in Fig 5-2(b). Microwave power was fixed to be 5 dBm and all measurements were carried out at room temperature. θ was fixed to be 45° unless otherwise indicated.

5.4 Out-of-plane torque induced by asymmetric electrode structure

5.4.1 Estimation of in-plane and out-of-plane torques

Figure 5-3(a) shows ST-FMR spectrum obtained from the device with Δl = 0 μm. Signals were well fitted using Eq. (1-7). Symmetric (antisymmetric) component obtained from the fitting is indicated as red (blue) curves. Inset shows microwave frequency, f, as a function of FMR field, $\mu_0 H_0$. Plots were well fitted using the Kittel formula [Eq. (1-4)], indicating successful observation of the FMR. The same measurement was carried out for the device with $\Delta l = -20$ μm as shown in Fig. 5-3(b). Although signals were well fitted using Eq. (1-7),

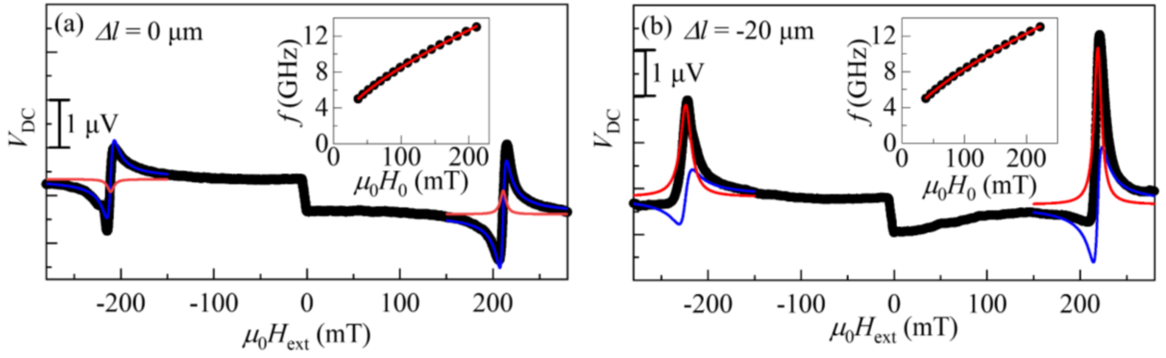

FIG. 5-3. ST-FMR spectra for devices with (a) Δl = 0 μm and (b) −20 μm at θ = 45°. Blue and red curves show anti-symmetric and symmetric component obtained from the fitting using Eq. (1-7). Insets show microwave frequency as a function of H_0 with the fitting curve using Eq. (1-4).

both the amplitudes of A and S were obviously different depending on the polarity of H_{ext}. Note that f- $\mu_0 H_0$ plot was fitted using Kittel formula, indicating uniform FMR excitation even if electrode structure is asymmetric. To further investigate the origin of the asymmetry in the amplitude of FMR spectra when Δl = −20 μm, θ dependences of A and S were measured. Figures 5-4(a) - 5-4(f) show A and S as a function of θ when Δl = 0 μm, Δl = 20 μm, and Δl = −20 μm, where lines in color indicate fitting (red), $\sin 2\theta \cos\theta$ (blue), $\sin 2\theta \sin\theta$ (purple), $\sin 2\theta$ (green), and $\sin\theta$ (brown) components obtained by Eq. (1-8) and Eq. (1-9). Origins of each angular dependence are shown in Table 1-1 and Table 1-2 in Chap. 1. To note is that $\sin 2\theta$ components in A and S corresponding to OOP DL and FL torques, respectively, were significantly enhanced when Δl = ±20 μm compared to Δl = 0 μm and sign of them changed depending on the sign of Δl, indicating that the OOP DL and FL torques are generated by introducing asymmetry to the electrode structure.

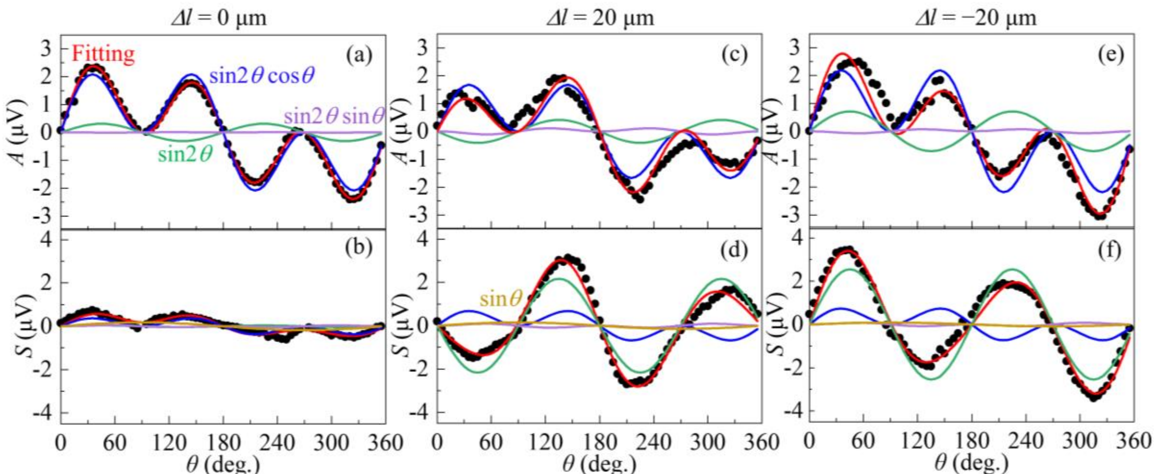

FIG. 5-4. θ dependences of (a) A and (b) S for a device with Δl = 0 μm. Those of devices with (c and d) Δl = 20 μm and (e and f) −20 μm are also shown. Fitting (red), which was done using the sum of $\sin 2\theta \cos\theta$ (blue), $\sin 2\theta$ (green), and $\sin 2\theta \sin\theta$ (purple) [and $\sin\theta$ (brown) for S], are shown in solid lines.

5.4.2 Controlling out-of-plane torques by electrode structure

To clarify the correlation between electrode asymmetry and the OOP torques, the author prepared several devices with different values of Δl and estimated OOP torque efficiencies. Given that $\sin 2\theta$ component is even function of H_{ext} (sign does not change after rotating θ by 180°) whereas the other components are odd function of H_{ext}, effective magnetic field of IP DL ($H_{DL,y}$), OOP FL($H_{FL,z}$), IP FL($H_{FL,y}$), and OOP DL ($H_{DL,z}$) torques are expressed as,

$$S_{odd} \equiv \frac{S_\theta - S_{180°+\theta}}{2} = H_{DL,y} \frac{\pi w t R_{AMR} f}{\Gamma \mu_0 \gamma (2H_0 + M_{eff})} \sin 2\theta \cos\theta, \quad (5\text{-}1)$$

$$S_{even} \equiv \frac{S_\theta + S_{180°+\theta}}{2} = -H_{FL,z} \frac{\pi w t R_{AMR} f}{\Gamma \mu_0 \gamma (2H_0 + M_{eff})} \sin 2\theta, \quad (5\text{-}2)$$

$$A_{odd} \equiv \frac{A_\theta - A_{180°+\theta}}{2} = -H_{FL,y} \frac{w t R_{AMR} (H_{res} + M_{eff})}{2\Gamma (2H_0 + M_{eff})} \sin 2\theta \cos\theta, \quad (5\text{-}3)$$

and

$$A_{\rm even} \equiv \frac{A_\theta + A_{180°+\theta}}{2} = -H_{{\rm DL},z}\frac{wtR_{\rm AMR}(H_0+M_{\rm eff})}{2\Gamma(2H_0+M_{\rm eff})}\sin 2\theta. \tag{5-4}$$

w is the width of the channel, $\hbar$ is the Dirac constant, e is the elementary charge, and t is the thickness of the Py layer. Here, $\sin 2\theta \sin\theta$ and $\sin\theta$ components are neglected because they are negligibly small in this experiment. Torque efficiency, ξ, calculated using,

$$H_{\rm DL(FL)} = \xi_{\rm DL(FL)}\frac{\hbar I_{\rm rf}}{2e\mu_0 M_S w t^2}, \tag{5-5}$$

are shown in Figs. 5-5(a) - 5-5(d). IP DL and FL torques ($\xi_{{\rm DL},y}$ and $\xi_{{\rm FL},y}$) did not show notable correlation with Δl. On the other hand, OOP DL and FL torques ($\xi_{{\rm DL},z}$ and $\xi_{{\rm FL},z}$) monotonically increased as increasing Δl. Therefore, the author concluded that the OOP torques are generated by asymmetry of electrode structure.

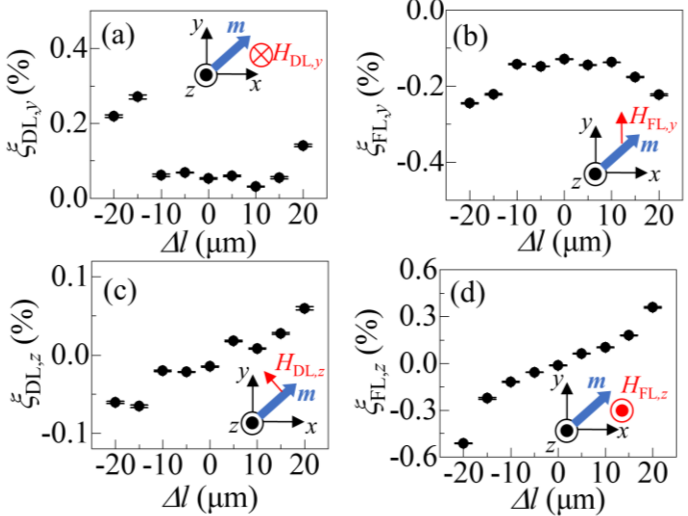

FIG. 5-5. (a) IP DL, (b) IP FL, (c) OOP DL, and (d) OOP FL torque efficiencies as a function of Δl. Orientations of effective fields generated by each torque are shown in the insets.

5.4.3 Origin of the out-of-plane torques

In this section, the author discusses the origin of the OOP torques. Origin of the OOP FL torque was discussed in previous works by Sklenar [22] and Ikebuchi [57]. They concluded that the OOP FL torque originates from the OOP Oersted field due to nonuniform current flow, which is also expected to exist in this experiment. However, OOP Oersted field cannot contribute to the OOP DL torque because symmetry of the torque is completely different. One might expect that the spin accumulation at the edge of the Py channel via the SHE

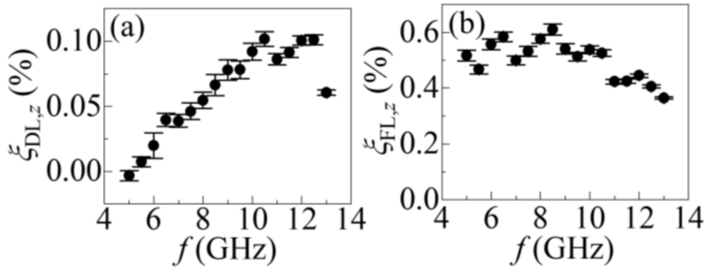

FIG. 5-6. Microwave frequency dependence of OOP DL and OOP FL torque efficiencies.

contributes to the OOP DL torque, because OOP spin accumulation at one side with a shorter length is more significant compared to the that with a longer length because of the difference in current density. However, the sign of $\xi_{DL,z}$ is expected to be opposite based on the fact that the SHA of Py is positive [58,59]. OOP DL torque can also be generated by precession of spin in the FM layer due to interface Rashba field [60,61]. However, DL torque due to surface precession should have additional $\cos\theta$ dependence in S, which cannot explain $\sin 2\theta$ dependence of the OOP DL torque observed in this experiment. To reveal the origin of the OOP DL torque, frequency dependences of $\xi_{DL(z)}$ and $\xi_{FL(z)}$ were measured. Figures 5-6(a) and 5-6(b) show $\xi_{DL(z)}$ and $\xi_{FL(z)}$ as a function of f. Both the OOP DL and FL torques show significant f dependence: $\xi_{DL,z}$ increases as increasing f and saturates at around 10 GHz, whereas $\xi_{FL,z}$ drops down above 10 GHz. If the OOP DL torque is generated by OOP spin accumulation, such frequency dependence cannot be explained. Plausible origin of the OOP DL torque observed in this experiment is the inductive magnetic field. Schematic of the explanation is shown in Fig. 5-7. According to the previous study, origin of the OOP FL torque is expected to be OOP Oersted field, $B_{Oersted}$ [Fig. 5-7(a)]. Since $B_{Oersted}$ is oscillating with microwave frequency, eddy current and resulting inductive magnetic field, $B_{induc.}$, is expected to be generated, which is well known as the complex magnetic permeability. Torque generated by $B_{induc.}$ is FL [Fig. 5-7(c)]. However, the phase of $B_{induc.}$ is shifted by $\pi / 2$, causing pseudo DL torque as shown in Figs. 5-7(b) and 5-7(d). Indeed, this hypothesis well explains the f dependences of OOP torques: OOP DL torque corresponding to the imaginary part of the permeability increases and saturates as increasing f, whereas OOP FL torque corresponding to the real part of the permeability starts to decrease from the frequency where inductive effect starts to saturate [62]. Therefore, the author concluded that the OOP DL torque in this experiment is caused by the inductive magnetic field.

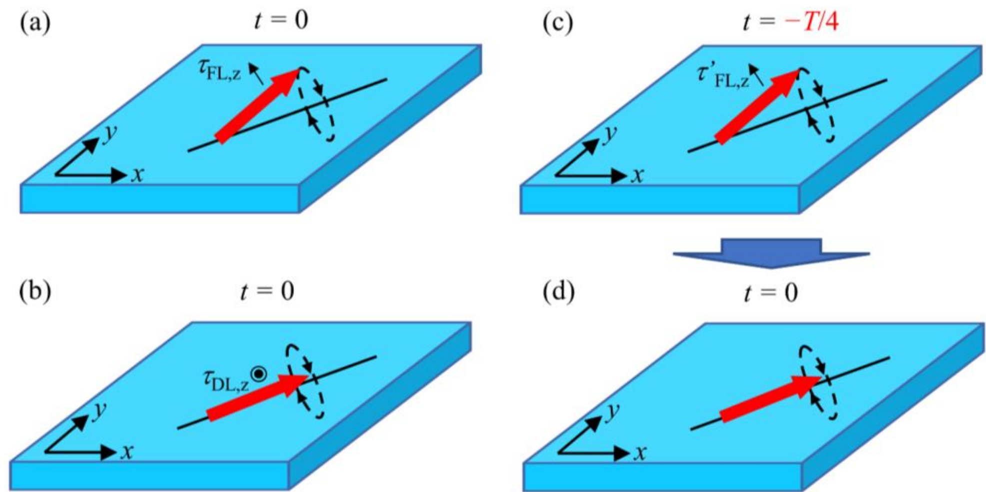

FIG. 5-7. Schematics of the explanation of how the torque caused by the inductive field contributes to the DL torque. (a) Direction of magnetization at $t = 0$ when the FMR is caused by the OOP FL torque and (b) OOP DL torque. (c) Direction of magnetization at $t = -T/4$ and (d) $t = 0$ when the FMR is caused by the OOP FL torque due to inductive field.

5.5 Application to the magnetoresistive random access memory

Although the OOP DL torque in this experiment was not caused by the OOP spin generation, the author found

out that it can be applicable to the field-free SOT switching of a FM with OOP magnetic anisotropy. When a heavy metal/FM bilayer structure is connected to the asymmetric electrode structure, IP DL torque due to the SHE rotates magnetization from $+z$ to the IP direction. After stopping pulse current, OOP DL torque due to $B_{\text{induc.}}$ is expected to make magnetization aligned along $-z$ direction. To verify such magnetization switching is possible, micromagnetic simulation using MuMax3 [34] was carried out. Figure 5-8 shows a schematic of the simulation. After magnetization is initialized along $+z$ direction, IP-spin-polarized pulse current with a width of $t_{\text{pls}} = 300$ ps is injected at $t = 0$. Following the pulse current, inductive field expressed as $B_{\text{induc.}} = B_0\exp[-(t - t_{\text{pls}}) / \tau]$ is applied, where time constant, τ, was set to be 500 ps. $B_{\text{induc.}}$ is reproduced by exponentially decayed magnetic field after stopping pulse current. Figure 5-9(a) shows simulated time evolution of the normalized z component of magnetization, m_z, with different magnitudes of B_0. Successful magnetization switching was demonstrated when $B_0 > 2$ μT, indicating that magnetization switching of the OOP FM is realized by $B_{\text{induc.}}$. To note is that magnetization switching cannot be realized by simply applying B_{Oersted} at the same time as the IP spin injection as shown in Fig. 5-9(b). Therefore, the author concluded that time delay of the OOP magnetic field due to inductive effect is essential for realizing OOP magnetization switching.

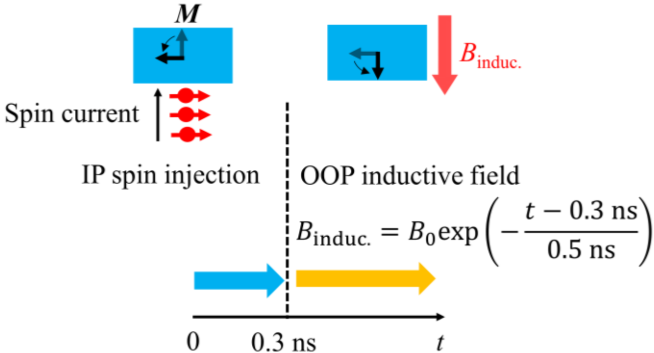

FIG. 5-8. A schematic of the simulation of magnetization reversal using IP DL torque and OOP inductive field.

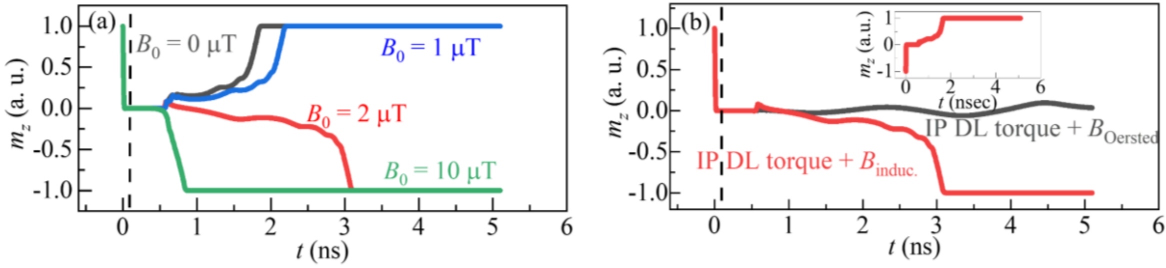

FIG. 5-9. (a) Calculated time evolution of m_z after application of IP DL torque with different magnitudes of inductive field. (b) Comparison of the time evolution of m_z with the assistance of OOP Oersted field and OOP inductive field.

Finally, the author proposes the MRAM structure as shown in Fig. 5-10. SOT layer is connected to asymmetric electrodes to generate B_{Oersted}. Since the FM electrode in a practical MRAM device is smaller than 100 nm, eddy current and resulting $B_{\text{induc.}}$ cannot be generated due to skin effect (see Appendix Section C for detail). To avoid this problem, the author proposes to fabricate metal layer that is separated from the MRAM circuit by insulating layer. Such large-area metal layer efficiently generates $B_{\text{induc.}}$ and will enable field-free

switching of the FM electrode.

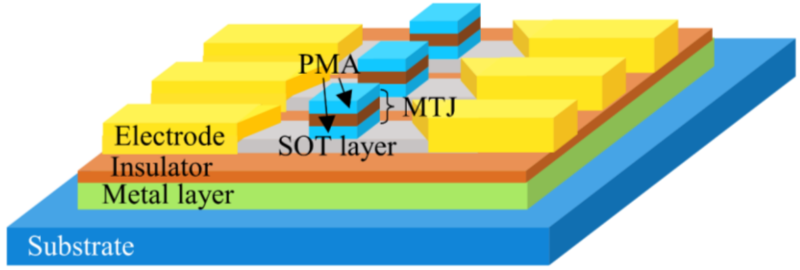

FIG. 5-10. A schematic of the device structure for field-free OOP MRAM utilizing inductive torque.

5.6 Summary

The author observed out-of-plane damping-like torque in a permalloy layer connected to asymmetric electrodes. Frequency dependence of the out-of-plane damping-like torque indicates that the origin is not out-of-plane spin accumulation but out-of-plane inductive field. From the micromagnetic simulation, out-of-plane damping-like torque caused by the inductive effect can realize magnetization switching of a ferromagnet with out-of-plane magnetic anisotropy without assist magnetic field. Importance of this study is that the asymmetry of electrode structure can be introduced by lithography technique, which is much easier and more versatile compared to the out-of-plane spin generation proposed so far. This method will contribute to the improvement of magnetoresistive random access memory technology as well as a better understanding of current-induced out-of-plane torque.

Chapter 6. Self-induced spin-orbit torque in nonmagnetic material/ferromagnetic material bilayer structures

6.1 Abstract

Until recently, strategy for realizing efficient spin-orbit torque generation via charge-to-spin conversion is to investigate material composed of heavy elements such as Pt, W, Bi, and/or Ta [8,27,63–65]. This is because the spin Hall effect originates from the spin-orbit interaction, which generally increases with increasing atomic number of the element (see Section 1.3). However, recent studies have revealed that ferromagnet also possesses large charge-to-spin conversion such as the spin Hall effect due to interplay between the spin-orbit interactiojn and time reversal inversion symmetry breaking [66–71]. In this sense, in a nonmagnet/ferromagnet bilayer structure, not only the spin Hall effect in the nonmagnet layer but also that in the ferromagnet layer gives rise to the spin-orbit torque acting on the magnetization of the ferromagnet itself, called self-induced spin-orbit torque [72]. However, self-induced spin-orbit torque in a nonmagnet/ferromagnet bilayer structure has been overlooked so far.

In this chapter, the author verifies significant influence of the self-induced spin-orbit torque comparable to the spin-orbit torque originating from the nonmagnet layer by measuring the ferromagnet thickness dependence of the torque acting on the magnetization using Ta/Co, Pt/Fe, and permalloy/Pt bilayer structures. Significant suppression of the torque acting on magnetization as increasing ferromagnet thickness was observed in Ta/Co and Pt/Fe bilayer structures, where the spin Hall angles of the nonmagnet and ferromagnet layers are opposite to each other and self-induced spin-orbit torque cancels the spin-orbit torque originating from the nonmagnet layer. Calculation based on the spin diffusion model indicates that material for efficient spin-orbit torque generation needs to be searched under consideration of the self-induced spin-orbit torque. This research proposes a novel strategy for spin-orbit torque research and indicates that revisiting spin-orbit torque research that claims gigantic spin Hall angle in a low-conductive material might be needed because self-induced spin-orbit torque becomes salient as a nonmagnet becomes less conductive.

Results presented in this chapter were published in the paper:

M. Aoki, E. Shigematsu, R. Ohshima, T. Shinjo, M. Shiraishi, and Y. Ando, "Anomalous sign inversion of spin-orbit torque in ferromagnetic/nonmagnetic bilayer systems due to self-induced spin-orbit torque", Physical Review B **106**, 174418 (2022).

6.2 Introduction and research purpose

6.2.1 Revisiting of the spin-orbit torque

First, the author revisits the mechanism of the SOT originating from the SHE in the NM layer. In a NM/FM bilayer structure, electric current flowing in the NM layer, $J_{c(NM)}$, is converted to spin current, $J_{s(NM)}$, via the SHE (Fig. 6-1). Spin current is injected into the FM layer and causes fluctuation of spin angular momentum in the FM layer. Owing to conservation of angular momentum, torque acts on the magnetization of the FM layer, which is called the SOT. To note is that the essence of the SOT is the fluctuation of spin angular momentum in the FM layer.

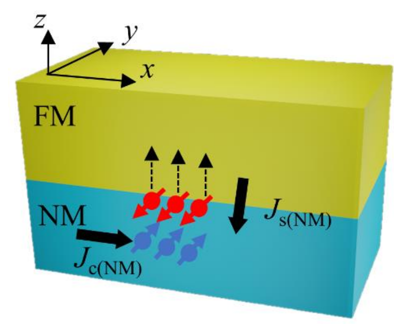

FIG. 6-1. Spin injection into FM via the SHE in NM.

6.2.2 Mechanism of the self-induced spin-orbit torque

On the other hand, electric current in the FM layer, $J_{c(FM)}$, is converted to the spin current, $J_{s(FM)}$, via the SHE in the FM layer (Fig. 6-2). $J_{s(FM)}$ diffuses into the NM layer owing to the spin relaxation in the NM layer and causes fluctuation of spin angular momentum in the FM layer. In this case, also, torque is given to the magnetization of the FM layer. This self-induced SOT (SI-SOT) has been neglected until recently, however, recent discoveries of large SHE in FMs [58,68] indicate need of considering SI-SOT in a NM/FM bilayer structure. Purpose of this study is to observe SI-SOT in NM/FM bilayer structures and show the significance of the SI-SOT in the SOT research.

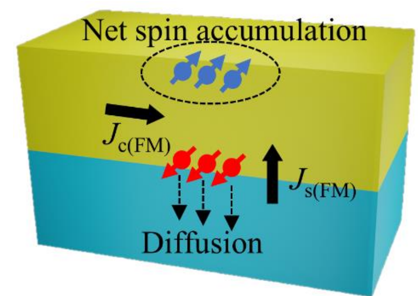

FIG. 6-2. Spin absorption into NM via the SHE in FM.

6.3 Experimental setup

6.3.1 Sample fabrication

Ta/Co bilayer structure was mainly used in this study. Since the SHA of Ta and Co are opposite to each other, SI-SOT caused by the SHE in Co cancels the SOT caused by the SHE in Ta. If sign reversal of the net of SOT acting on magnetization is observed, conventional flamework without considering the SI-SOT cannot explain the result and existence of the SI-SOT can be confirmed. A rectangular shape of Ta (t_{NM} nm)/Co (t_{FM} nm)/SiO_2 (7 nm) channel was fabricated using EB lithography and DC magnetron sputtering. After patterning of electrode by EB lithography, SiO_2 capping layer was etched by Ar ion milling. Then, the sample was moved into EB evaporation system without breaking vacuum and Ti (3 nm)/Au (70 nm) layers were deposited as an electrode.

6.3.2 Measurement setup

Figure 6-3 shows schematics of the device structure and measurement circuit used in this study. ST-FMR

method was mainly used in this study. Microwave current was irradiated by using an analog commercial signal generator (KEISIGHT N5173B EXG) and rectification DC voltage, V_{DC}, was detected using a nanovoltmeter (Keithley Nanovoltmeter 2182A) via bias tee. External magnetic field, H_{ext}, was applied along IP direction, where the angle between x axis and H_{ext} was defined as θ. SHH measurement was also carried out as a control experiment. In the SHH measurement, an AC current, I_{ac}, with a frequency of 17 Hz was injected by an AC and DC current source (Keithley 6221) (see Fig. 6-4 for a schematic of device structure). SHH signals were detected by a lock-in amplifier (Stanford Research System SR 830). The samples were set in a physical property measurement system (Quantum Design PPMS) and H_{ext} was applied along IP direction, where angle between x axis and H_{ext} was defined as ϕ.

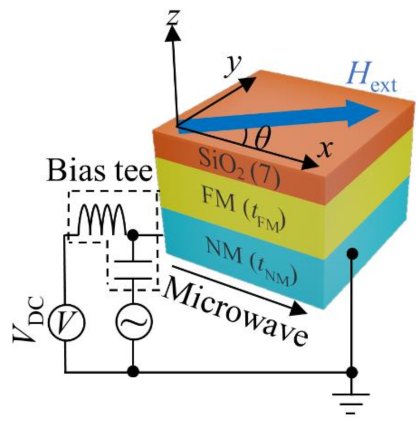

FIG. 6-3. Schematics of the device structure and measurement circuit for the ST-FMR method.

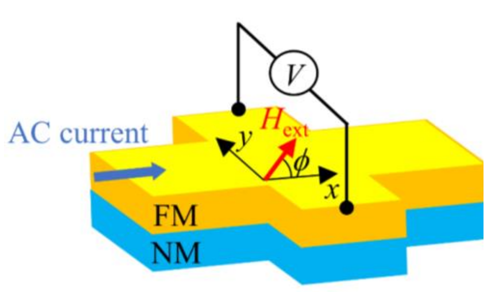

FIG. 6-4. A schematic of the device structure for the SHH measurement.

6.4 Sign reversal of the net of spin-orbit torque

6.4.1 Spin-torque ferromagnetic resonance

Figure 6-5(a) shows ST-FMR spectra obtained from (left) Ta(5)/Co(3), (middle) Ta(5)/Co(5), and (right) Ta(5)/Co(17.5) devices, where numbers in bracket indicate thickness in the unit of nanometer. θ and signal output power were fixed to be 45° and 13 dBm, respectively. f was set to be 13 GHz when t_{FM} = 3 nm and 16 GHz when $t_{FM} \geq 5$ nm. Red and blue lines are symmetric and antisymmetric components obtained from the fitting using Eq. (1-7). Sign of A changes between t_{FM} = 3 nm and 5 nm, which is explained by the competition between Oersted field and FL-SOT [73]. On the other hand, sign reversal of S between t_{FM} = 5 nm and 17.5 nm, meaning sign reversal of the DL-SOT, can be explained by the competition between SOT generated by the SHE in Ta and SI-SOT generated by the SHE in Co because thickness dependences of these two are different with each other as discussed later. To confirm that sign reversal of S originates from the SI-SOT, the author measured θ dependence of S and A to eliminate artifacts such as nonuniform flow of electric current (see Section 1.8.2). Figures 6-5(b) and 6-5(c) show θ dependence of S for devices with t_{FM} = 5 nm and 17.5 nm, respectively. Lines in color indicate $\sin 2\theta \cos\theta$ (blue), $\sin 2\theta$ (green), $\sin 2\theta \sin\theta$ (purple), and $\sin\theta$ (brown) components, origin of which are shown in section 1.8.2. All signals were successfully fitted by the sum of these angular dependences (fittings are shown as red lines) and dominated by $\sin 2\theta \cos\theta$ component coming from either SOT or SI-SOT.

Note that the SP-ISHE and ANE in $\sin 2\theta \cos\theta$ were negligibly small (see Appendix Section D for detail). From these results, the author concluded that SOT originating from Ta is canceled by the SI-SOT originating from Co.

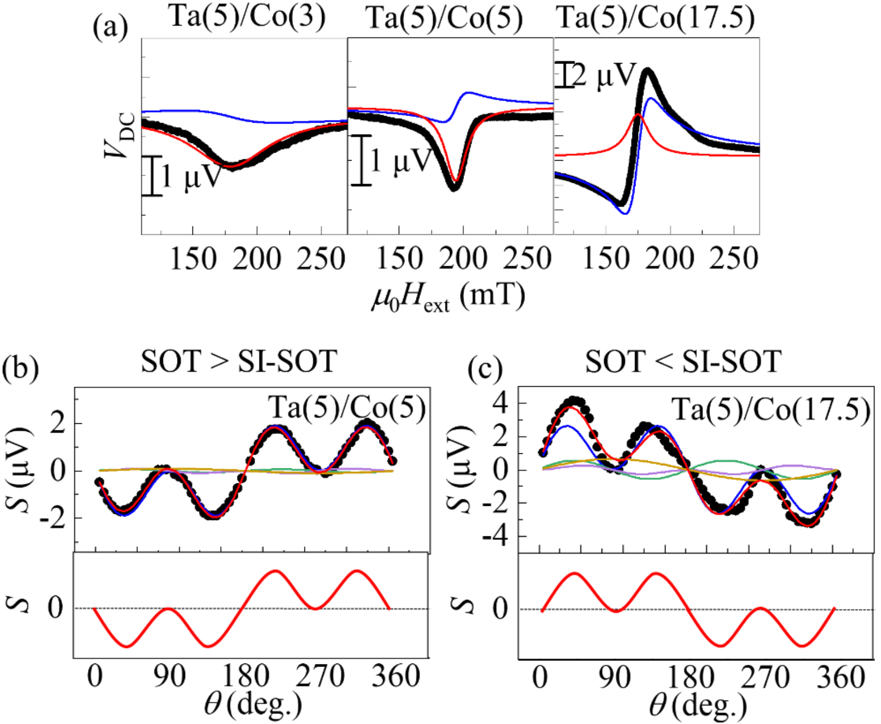

FIG. 6-5. (a) ST-FMR spectra at $\theta = 45°$ for the Ta/Co device with (left) t_{FM} = 3 nm, (middle) 5 nm, and (right) 17.5 nm. Red and blue curves correspond to the symmetric and anti-symmetric components obtained by the fitting using Eq. (1-7). (b) S as a function of θ for the Ta/Co device with t_{FM} = 5 nm and (c) 17.5 nm. Solid lines are fitting (red), $\sin 2\theta \cos\theta$ (blue), $\sin 2\theta$ (green), $\sin 2\theta\ \sin\theta$ (purple), and $\sin\theta$ (brown) components. Lower panels of (b) and (c) show expected θ dependence when SOT originating from Ta is more and less significant compared to the SI-SOT originating from Co, respectively.

6.4.2 Control experiments by the second harmonic Hall method

To confirm that sign inversion due to SI-SOT is true, the author estimated SOT in Ta/Co bilayers by using SHH method. Figures 6-6(a) and 6-6(b) show the SHH resistance as a function of ϕ for Ta(5)/Co(3) and Ta(5)/Co(10), respectively, where signals were fitted by Eq. (1-14). $\cos\phi$ components of the SHH resistance obtained by Eq. (1-14), R_a, were plotted as a function of $\mu_0 H_{ext}$ for Ta(5)/Co(3) and Ta(5)/Co(10) as shown in Figs. 6-6(c) and 6-6(d), respectively. ξ_{DL} can be estimated by applying fitting using Eq. (1-15) to R_a-$\mu_0 H_{ext}$ plot. As a result, ξ_{DL} was negative (− 0.093 ± 0.004) for Ta(5)/Co(3) whereas it was positive (+ 0.013 ± 0.012) for Ta(5)/Co(10). Sign reversal of the torque acting on magnetization as increasing t_{FM} was also confirmed in the SHH method, consistent with the result of the ST-FMR measurement. The author also obtained consistent result in the measurement of shift of the MR curve (see Appendix Section E for detail).

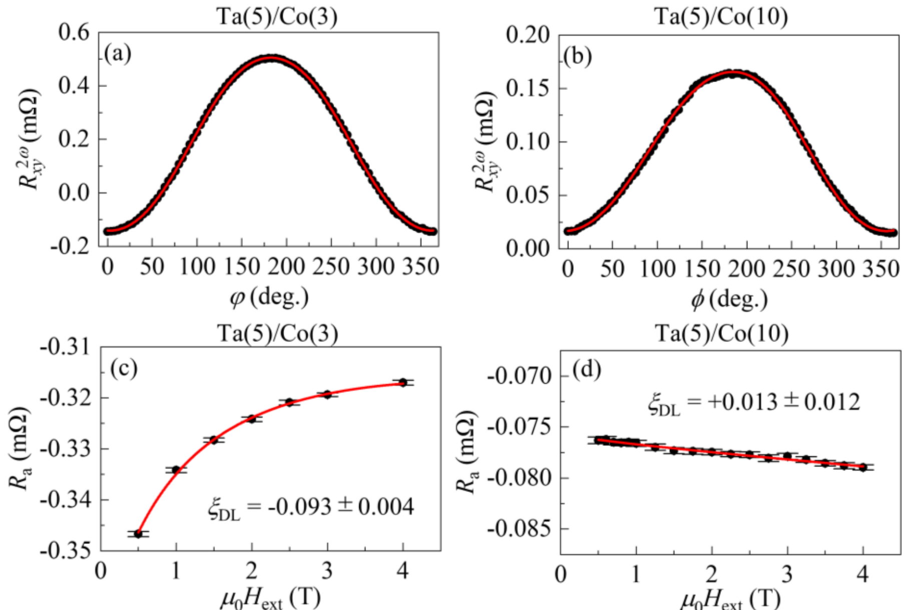

FIG. 6-6. (a) SHH voltage as a function of ϕ for the device with t_{FM} = 3 nm and (b) 10 nm. (c) cosϕ component of the SHH voltage as a function of μ_0H_{ext} for the device with t_{FM} = 3 nm and (d) 10 nm.

6.4.3 Control experiments using different materials

SOT in Pt/Fe bilayers was also investigated by the ST-FMR. Since the SHAs of Fe and Pt are opposite to each other [58], cancellation of SOT originating from Pt by SI-SOT originating from Fe is expected in the same

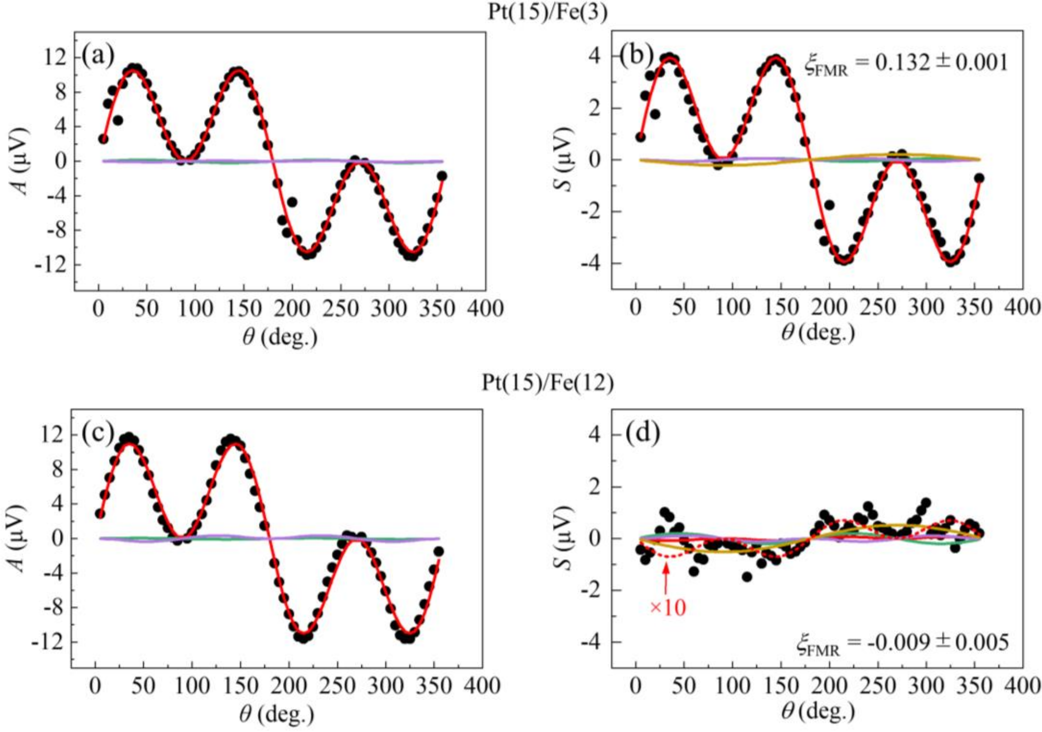

FIG. 6-7. (a)[(c)] θ dependences of A and (b)[(d)] S for the Pt (15)/Fe (3) [Pt (15)/Fe (12)] device.

manner as Ta/Co bilayers. Figures 6-7(a) and 6-7(b) show θ dependence of A and S for Pt (15)/Fe (3) bilayer structure. θ dependences were successfully fitted with the sum of four different angular dependences and ξ_{FMR} was calculated to be + 0.132 ± 0.001 by using Eq. (1-10). This value roughly corresponds to the SHA in Pt, indicating negligible SI-SOT when t_{FM} = 3 nm. Figures 6-7(c) and 6-7 (d) show θ dependences of A and S for Pt (15)/Fe (12) bilayer. Clear $\sin 2\theta \cos\theta$ component of A was obtained. However, $\sin 2\theta \cos\theta$ component of S was negligibly small, resulting in small negative ξ_{FMR}, − 0.009 ± 0.005. Suppression of ξ_{FMR} as increasing thickness of Fe is consistent with the scenario of SI-SOT.

6.5 Analysis based on the spin-diffusion model

Figure 6-8(a) shows ξ_{FMR} as a function of t_{FM} for Ta/Co bilayer devices. Sign reversal of ξ_{FMR} at t_{FM} = 3 nm is caused by FL-SOT. On the other hand, sign of ξ_{FMR} also changed from negative to positive when t_{FM} was thicker than 7 nm due to the SI-SOT. Figure 6-8(b) shows inverse plot of Fig. 6-8(a). So far, ξ_{FL} and ξ_{DL} have been thought to be estimated from the slope and intercept of $1/\xi_{FMR}$-$1/t_{FM}$ plot [73,74]. However, $1/\xi_{FMR}$ as a function of $1/t_{FM}$ in Ta/Co bilayer apparently shows nonlinear behavior. Therefore, we calculated thickness dependence of ξ_{FMR} by solving spin-diffusion equation [72,75] applying the following boundary conditions: continuities of the spin chemical potential and spin current at the NM/FM interface, and zero spin current at the top and bottom of the NM/FM bilayer. Spin current with a spin polarization transverse to the magnetization at the NM/FM interface, $J_{s\perp}$, is expressed as,

$$J_{s\perp} = \frac{\tanh\left(\frac{t_{NM}}{2l_{NM}}\right) R_{s(NM)} J_{c(NM)} \theta_{NM} + \tanh\left(\frac{t_{FM}}{2l_{FM}}\right) R_{s(FM)} J_{c(FM)} \theta_{FM}}{R_{s(NM)} \coth\left(\frac{t_{NM}}{l_{NM}}\right) + R_{s(FM)} \coth\left(\frac{t_{FM}}{l_{FM}}\right)} \sin\theta. \quad (6\text{-}1)$$

θ_{NM} (θ_{FM}) is the SHA of the NM (FM) layer, and $R_{s(NM)}$ ($R_{s(FM)}$) $\equiv$ l_{NM} / σ_{NM} (l_{FM} / σ_{FM}) is the spin resistance of the NM (FM) layer, where σ_{NM} (σ_{FM}) is the conductivity and l_{NM} (l_{FM}) is the spin diffusion (relaxation) length of the NM (FM) layer (see Appendix Section F for detail). Given that the ξ_{DL} is simply expressed as, $\xi_{DL} = J_{s\perp} / (J_{c(Ta)} \sin\theta)$, ξ_{FMR} is calculated to be,

$$\xi_{FMR} = \left\{ \frac{R_{s(NM)} \coth\left(\frac{t_{NM}}{l_{NM}}\right) + R_{s(FM)} \coth\left(\frac{t_{FM}}{l_{FM}}\right)}{\tanh\left(\frac{t_{NM}}{2l_{NM}}\right) R_{s(NM)} \theta_{NM} + \tanh\left(\frac{t_{FM}}{2l_{FM}}\right) R_{s(FM)} \frac{\sigma_{FM}}{\sigma_{NM}} \theta_{FM}} + \frac{\hbar}{e\mu_0 M_s t_{NM} t_{FM}} \frac{\xi_{FL}}{\xi_{DL}} \right\}^{-1}. \quad (6\text{-}2)$$

Figures 6-8(c) and 6-8(d) show t_{FM} dependence of ξ_{FMR} calculated with variable θ_{FM} and fixed l_{FM} (Case 1A), and fixed θ_{FM} and variable l_{FM} (Case 1B), respectively. Values used in calculation were those expected in Ta/Co bilayer structure. We used literature values of l_{NM} and θ_{NM} and the measured values for σ_{NM} and σ_{FM} as shown in Case 1 in Table 6-1. ξ_{FL}/ξ_{DL} was set to be 1 given the fact that FL-SOT is large enough to cancel the Oersted field when t_{FM} < 5 nm. Cases 1A and 1B qualitatively reproduce experimental results shown in Fig. 6-8(a). Using θ_{FM} = 0.05, θ_{NM} = −0.15, l_{FM} = 3 nm, and l_{NM} = 1.8 nm, contribution of SI-SOT to ξ_{DL} is calculated to be approximately −43 % of that of the SOT arising from the NM layer, indicating that the SI-SOT significantly hampers the SOT from the Ta layer. The author also measured SOT in Py/Pt bilayer structure, where signs of SOT originating from Pt and SI-SOT originating from Py are the same and no sign reversal is expected. Figure 6-8(e) shows ξ_{FMR} as a function of t_{FM} for Py/Pt bilayers. ξ_{FMR} monotonically increases due to enhancement of

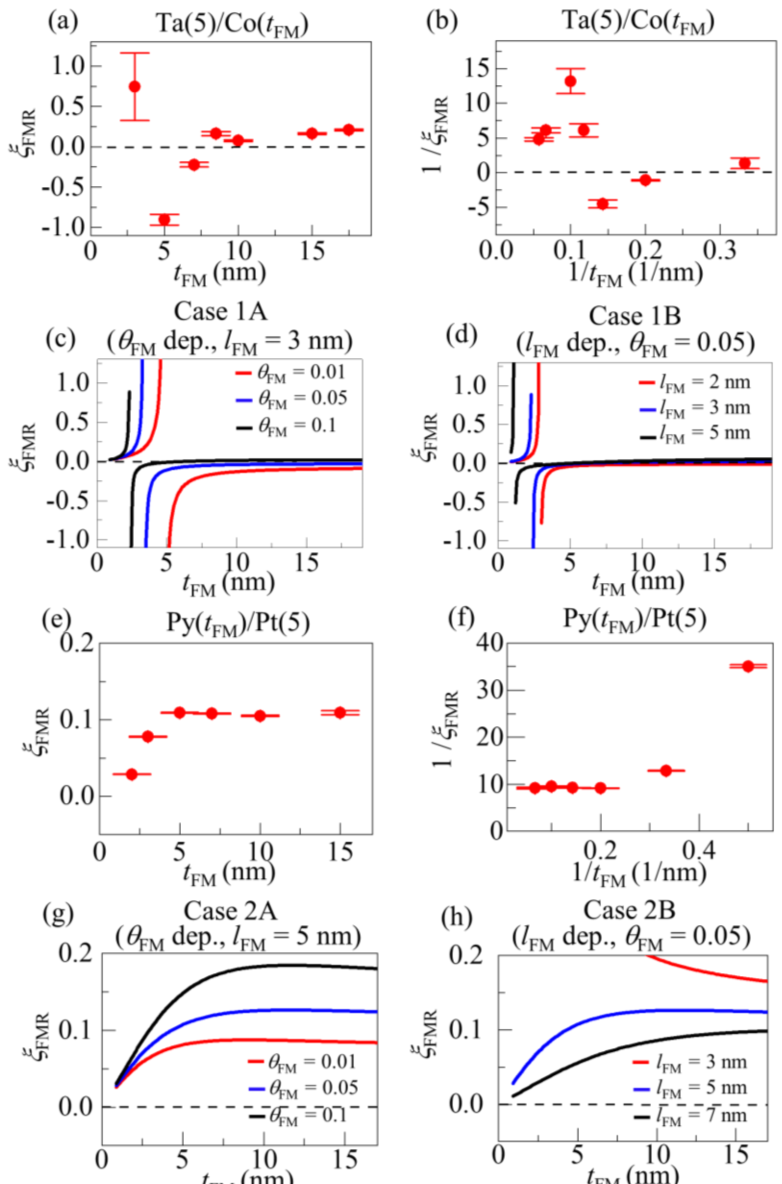

FIG. 6-8. (a) [(c)] ξ_{FMR} as a function of t_{FM} and (b) [(d)] inverse plots for Ta(5)/Co(t_{FM}) and Py(t_{FM})/Pt(5) devices. (e) Calculated t_{FM} dependence of ξ_{FMR} assuming case 1A, (f) case 1B, (g) case 2A, and (h) case 2B. Parameters used in the calculation are shown in Table 6-1.

SI-SOT and saturates at around t_{FM} = 5 nm. Indeed, $1/\xi_{FMR}$-$1/t_{FM}$ does not show linear behavior because of the SI-SOT, meaning that t_{FM} dependence in Fig. 6-8(f) cannot be explained by the FL-SOT contribution [73,74]. On the other hand, t_{FM} dependence of ξ_{FMR} was clearly explained by the spin diffusion model as shown in Fig. 6-8(g) (Case 2A) and 6-8(h) (Case 2B). Using θ_{FM} = 0.05, θ_{NM} = 0.32, l_{FM} = 5 nm, and l_{NM} = 1.4 nm, contribution of SI-SOT is estimated to be + 27% of that of SOT originating from Pt layer. To note is that combination of NM and FM layer with same polarity of SHA has advantage in terms of efficient SOT generation because SOT is efficiently generated with assistance from the SI-SOT. Searching combination of NM and FM where SOT and SI-SOT is enhanced by each other will be a novel strategy for realizing more efficient SOT generation.

Table 6-1. Parameters used in the calculation of the spin diffusion equation for each cases.

Case	σ_{NM} ($\times 10^4$ (Ω^{-1}m^{-1}))	σ_{FM} ($\times 10^4$ (Ω^{-1}m^{-1}))	l_{NM} (nm)	l_{FM} (nm)	θ_{NM}	θ_{FM}	ξ_{FL}/ξ_{DL}
1	43	101	1.8 [8]	2 – 5	–0.15 [8]	0.01 – 0.1	1
2	176	182	1.4 [74]	3 – 7	0.32 [74]	0.01 – 0.1	–0.2
3	176	101	3	5	0.1	0.1	–1,0,1
4	1.76 ~ 176	101	3	5	0.001 - 0.1	0.1	0

6.6 Influence on the estimation of the spin Hall angle

Since the SI-SOT is found to exist in typical NM/FM bilayer structures as Ta/Co, Py/Pt, and Pt/Fe, the author discusses how significantly the SI-SOT affects the estimation of the SHA in other systems by calculating Eq. (6-2) with different parameters (see Table 6-1). Figure 6-9(a) shows $1/\xi_{FMR}$ as a function of $1/t_{FM}$ when ξ_{FL}/ξ_{DL} = 1, 0, or −1 is assumed. In the conventional understanding, ξ_{FL} is proportional to the slope of this plot [73,74]. However, it is apparent that the slope is non-zero even when ξ_{FL} is zero due to the SI-SOT. Therefore, the author claims that ξ_{FL} cannot be estimated in such a conventional way. Figure 6-9(b) shows ξ_{FMR} as a function of t_{FM} when low-conductive material is used as a NM layer. This system corresponds to, *e.g.*, a topological insulator/FM bilayer structure. In this case, ξ_{FMR} is as large as 0.15 even when θ_{NM} is set to be 0.001. So far, ξ_{FMR} is believed to become close to θ_{NM} when t_{FM} is much thicker than spin-relaxation length of the FM layer. Therefore, result of Case 4A indicates θ_{NM} might be overestimated by more than two orders of magnitude if the SI-SOT is neglected. Calculated result of Case 4B, where σ_{NM} is changed, shows clear enhancement of ξ_{FMR} as decreasing σ_{NM} despite that θ_{NM} is fixed to be the same value as shown in Fig. 6-9(c). Given these results, the author claims that estimation of θ_{NM} needs to be careful especially when σ_{NM} is low. Mechanism of this overestimation is qualitatively explained as follows. ξ_{FMR} is calculated by dividing S by A. S originates from the sum of the SOT and the SI-SOT, where both $J_{s(NM)}$ and $J_{s(FM)}$ are considered. On the other hand, A mainly

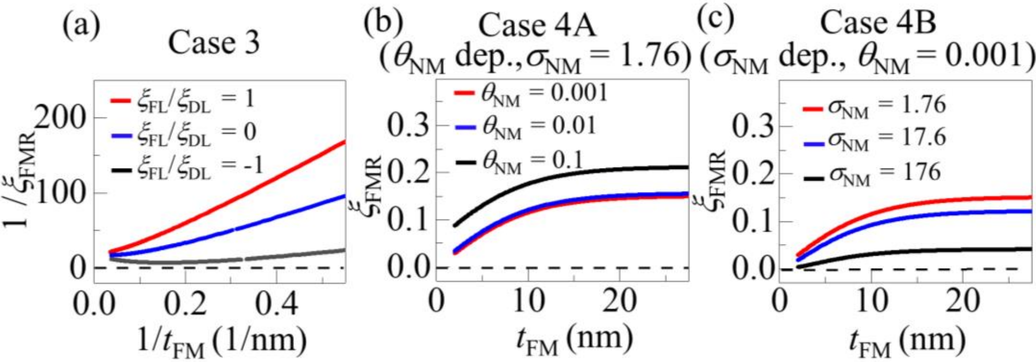

FIG. 6-9. (a) Calculated $1/t_{FM}$ dependence of $1/\xi_{FMR}$ assuming case 3. (b) Calculated t_{FM} dependence of ξ_{FMR} assuming case 4A and (c) case 4B. Parameters used in the calculation are shown in Table 6-1.

originates from the Oersted field, where only $J_{c(NM)}$ is considered. If electric current flows much more in the FM layer due to small conductivity of the NM layer, S / A is significantly enhanced because the denominator is quite small whereas the numerator is kept large. The author claims that this kind of overestimation also happens in other ways for estimating θ_{NM} such as the SHH method, current-induced switching, and shift of the MR curve (see Chap. 1.8), because in all method the signal produced by the sum of the SOT and SI-SOT is divided only by $J_{c(NM)}$.

6.7 Summary

The author verified existence of the self-induced spin-orbit torque in nonmagnet/ferromagnet bilayer structures by using multiple methods for measuring spin-orbit torque as well as using different materials. From the calculation using the spin-diffusion model, it was found that choosing nonmagnet and ferromagnet layers with the same sign of the spin Hall angle will enable more efficient spin-orbit torque generation. Moreover, the author found that the self-induced spin-orbit torque significantly hampers the conventional way for estimating the spin Hall angle of the nonmagnet layer. Especially when a low-conductive nonmagnet layer is used, self-induced spin-orbit torque needs to be considered in the analysis otherwise the value of θ_{NM} is misestimated by orders of magnitude. Therefore, this research will contribute to more precise estimation of the spin Hall angle as well as realize of low-power-consumption spin-orbit torque devices.

Chapter 7. Observation of giant self-induced spin-orbit torque and its anisotropy in $L2_1$ ordered Co_2MnGa single layer

7.1 Abstract

Spin-orbit torque enables manipulation and even switching of magnetization by electric current. Aiming at large spin-orbit torque generation for efficient spintronics devices, a variety of materials have been investigated and some of them have shown gigantic spin-orbit torque generation, *e.g.*, topological insulators [19,28,29]. On the other hand, material that exhibits anisotropy in the spin-orbit torque, *i.e.*, modulation of magnitude and/or sign of the spin-orbit torque with changing applied-current direction, is, in principle, limited to low-symmetric materials [76]. Since the anisotropic spin-orbit torque expands functionality of the spin-orbit torque devices whereas most of the materials with large spin Hall angle possess high-crystal symmetry, introducing anisotropy of spin-orbit torque to a material with high-crystal symmetry is desirable.

In this chapter, the author focuses on Co_2MnGa, a Heusler alloy with $L2_1$ crystal ordering and is known as a Weyl ferromagnet [77–79]. Owing to the presence of the Weyl cones and resulting large Berry curvatures, large self-induced spin-orbit torque was observed even without adjacent metal layer. Moreover, the author found that the self-induced spin-orbit torque in Co_2MnGa is strongly anisotropic, *i.e.*, sign of the self-induced spin-orbit torque reverses with changing applied-current direction by 45 degrees despite of its high-symmetric crystal structure. Additional experiments using Co_2MnGa films with different thicknesses and different capping materials, as well as theoretical calculations, revealed that the large self-induced spin-orbit torque and its anisotropy are induced by the distribution of the Weyl points and their modulation by external strain. This work will pave a way for introducing anisotropy to spin-orbit torque even for a material with high crystal symmetry.

Results presented in this chapter were published in the paper:

M. Aoki, Y. Yin, S. Granville, Y. Zhang, N. Medhekar, L. Leiva, R. Ohshima, Y. Ando, and M. Shiraishi "Gigantic anisotropy of self-induced spin-orbit torque in Weyl ferromagnet Co_2MnGa", Nano Letters, accepted.

7.2 Introduction and research purpose

7.2.1 Weyl ferromagnet Co_2MnGa

Co_2MnGa (CMG) is a Heusler alloy with $L2_1$ crystal ordering [see Fig. 7-1(a)] and classified into a topological material called Weyl ferromagnet [77–80]. Interesting point of this material is the presence of pairs of linear dispersion in momentum space as shown in Fig. 7-1(b), which is called Weyl point [81]. So far, large AHE [82], ANE [77,83], and SHE [59] have been reported in CMG due to the large Berry curvature originating from Weyl points.

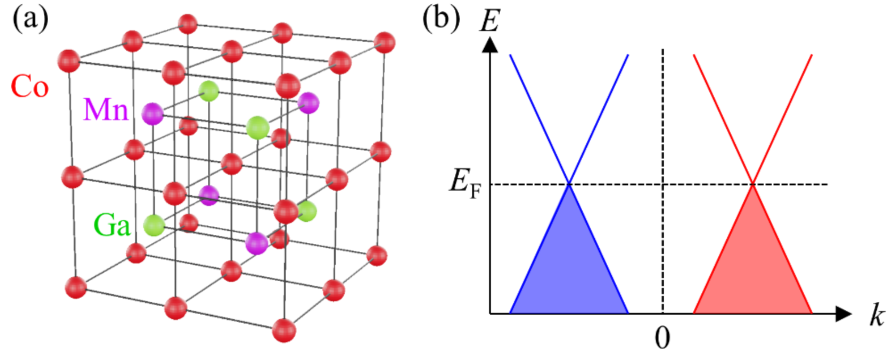

FIG. 7-1. (a) A schematic of crystal structure of $L2_1$-ordered CMG. (b) A schematic of the band structure of Weyl semimetal.

7.2.2 Anisotropy in the spin Hall effect

In this section, the author explains the relationship between anisotropy in the spin Hall conductivity (SHC) and symmetry of the crystal structure based on classical explanation by Chudnovsky [76]. When the SOI exists, Hamiltonian of one electron is given by,

$$\mathcal{H} = \frac{\boldsymbol{p}^2}{2m} + U(\boldsymbol{r}) + \frac{\hbar}{4m^2c^2}\boldsymbol{\sigma}\cdot(\nabla U \times \boldsymbol{p}), \tag{7-1}$$

where $\boldsymbol{p}$ is momentum of electron, m is effective mass of electron, $U(\boldsymbol{r})$ is the electrostatic crystal potential, c is speed of light, and $\boldsymbol{\sigma}$ is vector of spin. Since $1 / c^2$ is small enough compared to the other terms, Eq. (7-1) is equivalent to,

$$\mathcal{H} = \frac{1}{2m}\left(\boldsymbol{p} - \frac{e}{c}\boldsymbol{A}_\sigma\right)^2 + U(\boldsymbol{r}), \tag{7-2}$$

and vector potential, $\boldsymbol{A}_\sigma$, is defined as,

$$\boldsymbol{A}_\sigma \equiv -\frac{\hbar}{4emc}(\boldsymbol{\sigma} \times \nabla U). \tag{7-3}$$

Therefore, effective spin-dependent magnetic field acting on moving electron, $\boldsymbol{B}_\sigma$, is expressed as,

$$\boldsymbol{B}_\sigma = \nabla \times \boldsymbol{A}_\sigma = -\frac{\hbar}{4emc}[\nabla \times (\boldsymbol{\sigma} \times \nabla U)]. \tag{7-4}$$

By taking space average of Eq. (7-4), effective magnetic field, $\boldsymbol{B}_{\text{eff}}$, is expressed as

$$\boldsymbol{B}_{\text{eff}} = -\frac{\hbar}{4emc}\langle \boldsymbol{\nabla} \times (\boldsymbol{\xi} \times \boldsymbol{\nabla} U)\rangle, \quad (7\text{-}5)$$

where $\boldsymbol{\xi}$ is the vector of the spin averaged by space. SHE is qualitatively explained by the Lorentz force caused by $\boldsymbol{B}_{\text{eff}}$. For a cubic lattice structure,

$$\langle \boldsymbol{\nabla}_i \boldsymbol{\nabla}_j U\rangle = C\delta_{ij}, \quad (7\text{-}6)$$

where C is constant. Given that each element of Eq. (7-5) is composed of Eq. (7-6), $\boldsymbol{B}_\sigma$ becomes isotropic irrespective of crystal axis. Therefore, in a cubic material like CMG, in principle, sign and magnitude of SHC is always the same irrespective of applied-current direction.

7.2.3 Spin-orbit torque in a single ferromagnet layer

To generate SOT, net accumulation of up or down spins is needed. Therefore, high-symmetric structure like single FM layer sandwiched by two insulating layers does not allow generation of SOT, in principle. However, recent studies have found that SOT can be generated even in such a high-symmetric system if the situation at top and bottom interfaces are different in viewpoint of, *e.g.*, magnetic anisotropy [84], spin scattering [85], distortion [86], and/or REE [61]. In addition, SHE in $3d$ FMs has revealed to be significant by recent studies [58,68]. Therefore, SI-SOT in a single FM layer is sometimes sizable [84,87,88]. As mentioned in Section 7.2.1, SHE in CMG is significantly large owing to the presence of Weyl points in momentum space [59], indicating that the SI-SOT in a CMG layer without any adjacent metal layer can be sizable. The purpose of this study is to investigate SI-SOT in a single CMG layer.

7.3 Experimental setup

7.3.1 Sample fabrication

CMG (t nm) films were grown by Dr. Simon Granville and Dr. Yao Zhang at Victoria University of Wellington in New Zealand. CMG (001) films were epitaxially deposited on a single crystalline MgO (001) substrate in a Kurt J Lesker CMS-18 magnetron sputtering system. Before deposition of CMG films, MgO substrates were cleaned with an Ar plasma and then annealed at 400 °C for 1 hour in vacuum. After deposition, samples were post-annealed *in situ* at 550 °C for 1 hour. After cooling down the samples, capping layer [MgO (10 nm) or Ta (3 nm)] was deposited on the top. Samples were shipped to Kyoto and the author fabricated device for measuring SOT. CMG/cap layers were patterned into a Hall-bar shape using EB lithography and Ar ion milling. Then, electrode structure was drawn by EB lithography and capping layer was removed by Ar ion milling. After additional milling to remove surface oxidation layer, Ti (3 nm)/Au (100 nm) electrodes were deposited using EB evaporation without breaking vacuum.

7.3.2 Measurement setup

Figure 7-2 shows a schematic of the measurement setup for the SHH method. An AC current, I_{ac}, with a frequency of 17 Hz was injected using an AC and DC current source (Keithley 6221). SHH signals were detected by a lock-in amplifier (Stanford Research System SR830). Measurements were carried out in a physical

property measurement system (Quantum Design PPMS) and external magnetic field, $\mu_0 H_{ext}$, was swept from 0.3 to 4 T. Amplitude of I_{ac} was set to be 20 mA and 10 mA when t = 30 nm and 15 nm, respectively. All measurements were carried out at room temperature.

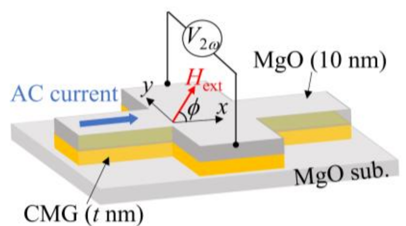

FIG. 7-2. A schematic of the device structure.

7.4 Material characterization

First, crystal structure was analyzed using X-ray diffraction (XRD) to verify single crystal $L2_1$ structure. Figure 7-3(a) shows $2\theta/\theta$ scan of XRD obtained from the MgO substrate/CMG (30 nm)/MgO (10 nm) film. Only CMG (002) and (004) peaks were obtained, indicating single-crystal growth along OOP direction. Inset shows $2\theta/\theta$ scan of XRD when $\phi = 45°$ and $\chi = 13.22°$. Presence of CMG (113) superstructure peak indicates $L2_1$ crystal ordering. Figures 7-3(b) and 7-3(c) show CMG (202) and MgO (202) peaks obtained from ϕ scan of XRD. When lattice constants of MgO and CMG are defined as a_{MgO} and a_{CMG}, relationship between crystal orientations of MgO and CMG is expected to be different by 45° as shown in Fig. 7-3(d) because $\sqrt{2}a_{MgO} \sim a_{CMG}$. MgO (202) peaks were shifted from CMG (202) peaks by 45°, which is consistent with the schematic shown in Fig. 7-3(d).

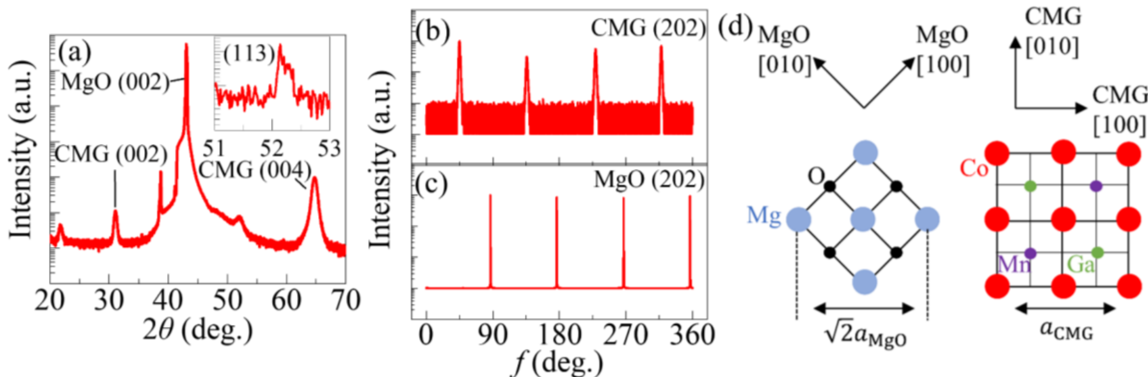

FIG. 7-3. (a) Spectrum of $2\theta/\theta$ scan. (b) CMG (202) and (c) MgO (202) peaks obtained from ϕ scan. (d) A schematic of the relationship between the crystal orientations of MgO and that of CMG.

7.5 Spin-orbit torque in Co_2MnGa

7.5.1 Anisotropy of the spin-orbit torque

First, SI-SOT was analyzed for the CMG (30 nm)/MgO (10 nm) film. Figures 7-4(a) and 7-4(b) show transverse resistance as a function of $\mu_0 H_{ext}$ applied OOP when I_{ac} was applied along CMG [100] and CMG [110] axis, respectively. Linear fittings were applied in three regimes: (1) large negative H_{ext} where magnetization is saturated, (2) small H_{ext} where magnetization is not saturated, and (3) large positive H_{ext} where magnetization is saturated. R_{AHE} was estimated from the difference of the line (1) and (3), whereas H_k was estimated from the intercept of lines (1) or (3) and (2). Fig. 7-4(c) and 7-4(d) show SHH resistance, $R_{2\omega}$, as a

function of ϕ when I_{ac} was applied along CMG [100] and CMG [110] axis, respectively. A black line is fitted line using Eq. (1-14). In this experiment, the author focuses only on the DL-SOT because FL-SOT is always coexisting with the Oersted field originating from small nonuniformity in the current distribution, which is difficult to subtract. Figures 7-4(e) and 7-4(f) show R_a as a function of $\mu_0 H_{ext}$ when I_{ac} was parallel to CMG [100] and [110] axes, respectively. Enhancement or suppression as decreasing H_{ext} corresponds to the signal induced by the DL-SOT according to Eq. (1-15). From the signals shown in Figs. 7-4(e) and 7-4(f), values of ξ_{DL} were estimated to be -0.133 ± 0.013 and $+0.050 \pm 0.009$ with I_{ac} along [100] and [110], respectively. There are two notable findings: (1) DL-SOT as large as a heavy metal/FM bilayer structure even without adjacent metal layer and (2) significant anisotropy of the DL-SOT with respect to applied-current direction.

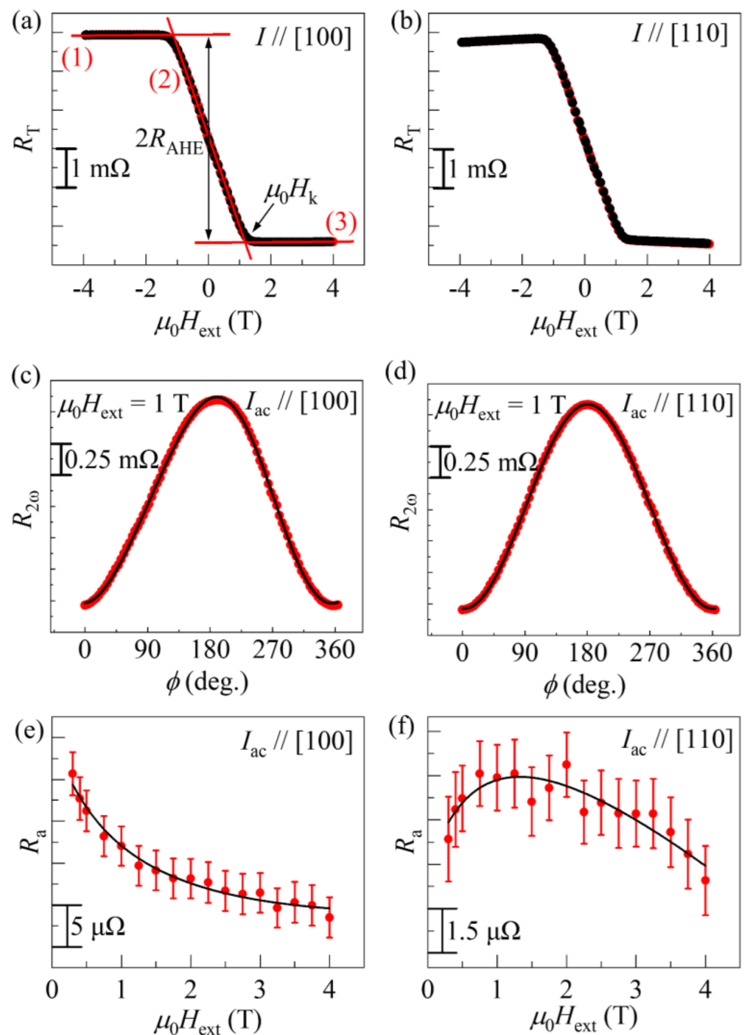

FIG. 7-4. (a) [(b)] AHE, (c) [(d)] SHH voltage as a function of ϕ, and (e) [(f)] V_a as a function of H_{ext} when electric current was applied along [100] ([110]) crystal axis.

7.5.2 Capping material and thickness dependences

The author also measured the DL-SOT for thinner CMG (t = 15 nm) and Ta-capped CMG films (t = 30 nm.) Figure 7-5 shows comparison of ξ_{DL}. In all devices, sign of ξ_{DL} depends on applied-current direction, indicating

strong anisotropy in the SI-SOT. To note is that ξ_{DL} is significantly enhanced as increasing t_{FM} from 15 nm to 30 nm in both MgO-capped and Ta-capped CMG films. If the DL-SOT originates from the REE (see Chap. 1-4), spins generated at the top surface should be canceled by those generated at the bottom surface in CMG/MgO devices. Top and bottom CMG/MgO interfaces might be different with each other due to the difference of the crystal structure and contribute to the DL-SOT. However, this scenario cannot explain strong enhancement of ξ_{DL} as increasing thickness of CMG in Ta-capped CMG films because MgO/CMG and CMG/Ta interfaces are always different irrespective of the value of t. Therefore, the author expected that the DL-SOT originates from the bulk of the CMG. Second, ξ_{DL} is further enhanced by changing the capping layer from MgO to Ta, which cannot be explained by SOT due to the SHE in Ta layer, sign of which is the same irrespective of applied-current direction. In the following, the author focuses on the bulk effect of CMG and investigates the origin of (1) large DL-SOT and (2) its anisotropy.

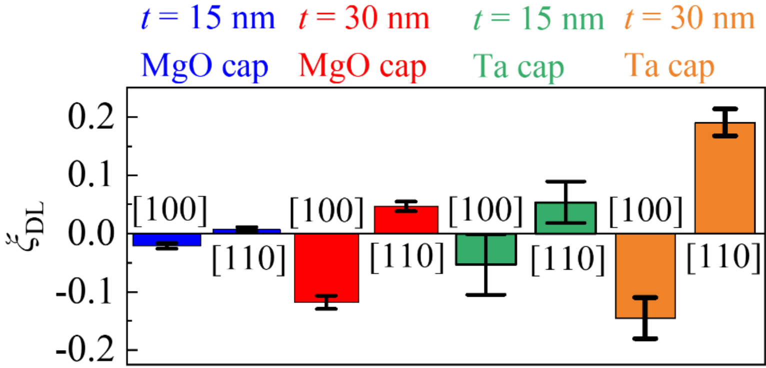

FIG. 7-5. Summary of the values of ξ_{DL} measured from CMG (t nm)/capping layer structures when I_{ac} was applied along [100] or [110] crystal axis.

7.6 Self-induced spin-orbit torque generated by nonuniform lattice distortion

7.6.1 Verification of lattice distortion

To investigate the origin of large ξ_{DL}, the author focused on a broken inversion symmetry due to nonuniform lattice distortion. CMG is epitaxially grown on the MgO (001) substrate. Since $\sqrt{2}a_{\mathrm{MgO}}$ (5.961 Å) is slightly longer than the bulk value of a_{CMG} (5.767 Å), lattice mismatch and resulting tetragonal distortion to CMG lattices as shown in Fig, 7-6(a) is expected. Since the distortion becomes stronger as is close to the substrate/CMG interface, SHA of CMG at top and bottom interfaces are also expected to be different with each other, causing the SI-SOT. To confirm existence of nonuniform distortion, the author compared the peak position of CMG (002) in the XRD spectra obtained from CMG films with t = 15 nm and 30 nm as shown in Fig. 7-6(b). A black line indicates expected peak position assuming bulk value of a_{CMG}. CMG (002) peaks were clearly shifted to higher angle as decreasing thickness, which means average value of out-of-plane lattice constant becomes shorter as t becomes thinner. Indeed, this trend is consistent with the schematic shown in Fig. 7-6(a). The author also measured FMR line width, Γ, using the ST-FMR method as shown in Fig. 7-6(c). Intercept of $\mu_0\Gamma$ - f plot (called inhomogeneous damping) is known to originate from the distortion of the lattice

structure [89]. Therefore, large intercept observed only in the CMG film with t = 15 nm is also consistent with the schematic shown in Fig. 7-6(a). From these experiments, the author concluded that there is a nonuniform distortion in our CMG films due to the lattice mismatch between MgO substrate and CMG.

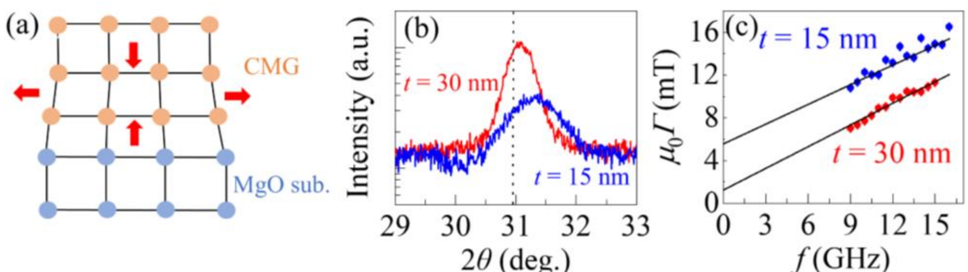

FIG. 7-6. (a) A schematic of the nonuniform strain caused by lattice mismatch. (b) CMG (002) peak of XRD and (c) FMR line width as a function of f for CMG thickness of 15 nm and 30 nm.

7.6.2 Calculation of spin diffusion equation

In this section, the author discusses how the nonuniform distortion contributes to the SI-SOT. The author starts from the spin-diffusion model [75] in a NM/FM/NM multilayer as shown in Fig. 7-7(a). As discussed before, SHA is also expected to be nonuniform because of the distortion. For simplicity, SHA is assumed to linearly change as a function of x, $\theta_{SH}(x) = \theta_{SH}\, x/t$, and SHE in the NM layer is neglected. Spin current, J_s, in the FM layer is calculated as,

$$J_{\mathrm{s}} = \frac{-\frac{\lambda_{\mathrm{N}}}{\sigma_{\mathrm{N}}} J_{\mathrm{c}} \theta_{\mathrm{SH}} \left[-\left\{ \frac{\lambda_{\mathrm{N}}}{\sigma_{\mathrm{N}}} - \frac{\lambda_{\mathrm{F}}}{\sigma_{\mathrm{F}}} \tanh\left(\frac{\delta}{\lambda_{\mathrm{N}}}\right) \right\} e^{-\frac{x}{\lambda_{\mathrm{F}}}} + \left\{ \frac{\lambda_{\mathrm{N}}}{\sigma_{\mathrm{N}}} - \frac{\lambda_{\mathrm{F}}}{\sigma_{\mathrm{F}}} \tanh\left(\frac{\delta}{\lambda_{\mathrm{N}}}\right) \right\} e^{\frac{x}{\lambda_{\mathrm{F}}}} \right]}{2\sinh\left(\frac{t}{\lambda_{\mathrm{F}}}\right) \left\{ \left(\frac{\lambda_{\mathrm{N}}}{\sigma_{\mathrm{N}}}\right)^2 + \left[\frac{\lambda_{\mathrm{F}}}{\sigma_{\mathrm{F}}} \tanh\left(\frac{\delta}{\lambda_{\mathrm{N}}}\right) \right]^2 \right\} + 4\frac{\lambda_{\mathrm{F}}\lambda_{\mathrm{N}}}{\sigma_{\mathrm{F}}\sigma_{\mathrm{N}}} \tanh\left(\frac{\delta}{\lambda_{\mathrm{N}}}\right) \cosh\left(\frac{\delta}{\lambda_{\mathrm{N}}}\right)} + J_{\mathrm{c}} \theta_{\mathrm{SH}} \frac{x}{t}, \tag{7-7}$$

where λ_N (λ_F) is spin diffusion (relaxation) length of the NM (FM), σ_N (σ_F) is conductivity of the NM (FM), and J_c is current density in the FM. Applying approximation, $\delta \rightarrow \infty$ and $t >> \lambda_F$ (~ 3 nm), ξ_{DL} is calculated to be,

$$\xi_{\mathrm{DL}} \sim \frac{\int_0^t \nabla J_{\mathrm{s}}(x) dx}{J_{\mathrm{c}}} = \frac{J_{\mathrm{s}}(t) - J_{\mathrm{s}}(0)}{J_{\mathrm{c}}} = \theta_{\mathrm{SH}}(t)\beta_t - \theta_{\mathrm{SH}}(0)\beta_0 \neq 0. \tag{7-8}$$

Here, spin absorption rate, β, is given by,

$$\beta = \frac{\frac{\sigma_{\mathrm{N}}}{\lambda_{\mathrm{N}}}}{\frac{\lambda_{\mathrm{F}}}{\sigma_{\mathrm{F}}} + \frac{\sigma_{\mathrm{N}}}{\lambda_{\mathrm{N}}}}. \tag{7-9}$$

Meaning of Eq. (7-8) is that combination of nonuniform θ_{SH} and spin absorption at top and bottom interfaces generate SI-SOT in a FM layer even without adjacent metal layer. Eq. (7-8) indicates that thicker CMG film is expected to show larger ξ_{DL} as the difference between $\theta_{SH}(0)$ and $\theta_{SH}(t)$ is larger. In addition, larger β_t is also expected to enhance ξ_{DL}. Both expectations are reproduced by calculating Eq. (7-8) a shown in Fig. 7-7(b). Indeed, this model well explains experimental results. For example, 30-nm-thick CMG film shows much larger ξ_{DL} compared to 15-nm-thick CMG and Ta-capped CMG shows even larger ξ_{DL} compared to MgO-capped CMG because of large spin absorption at CMG/Ta interface owing to the SOI in Ta as shown in Fig. 7-5. To note is that ξ_{DL} in CMG/MgO device is as large as that in heavy metal/FM bilayer, indicating large β at

CMG/MgO interface despite of absence of high SOI material. It is known that orbital hybridization is formed at CMG/MgO interface from the previous research, where perpendicular magnetic anisotropy of CMG is realized due to strong orbital hybridization between CMG and MgO or Pd [90]. Given that bonding between oxygen and metal ions contributes to strong REE [91,92], strong orbital hybridization at CMG/MgO interface well explains significant spin absorption at CMG/MgO interface and resulting large ξ_{DL}.

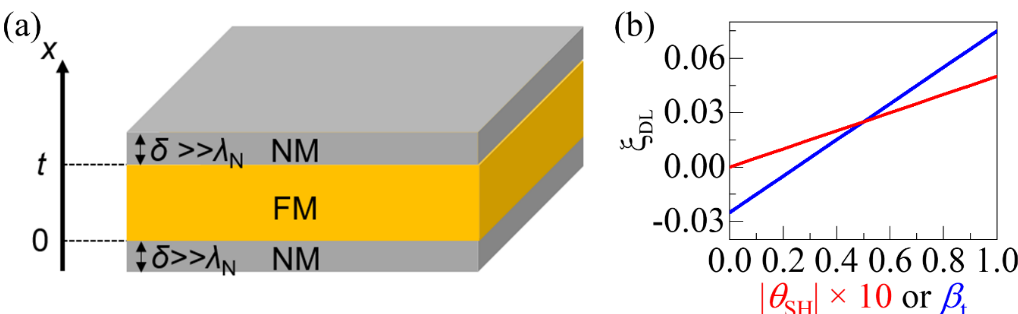

FIG. 7-7. (a) A schematic of the model assumed in the calculation. (b) ξ_{DL} as functions of $|\theta_{SH}|$ and β_t calculated using Eq. (7-8). $\beta_0 = 0.5$, $\theta_{SH(t)} = 0.1$, and $\theta_{SH(0)} = 0.05$ in the calculation of β_t dependence, whereas β_0 and β_t are set to be 0.5 in the calculation of $|\theta_{SH}|$ dependence.

7.7 First principles calculations

7.7.1 Band structure and spin Hall conductivity

Now the author verified that the large SI-SOT in CMG is caused by nonuniform distortion due to lattice mismatch and interface spin absorption. Next, the author discusses the origin of significant anisotropy in the SI-SOT with respect to applied-current direction. To investigate the origin of the anisotropy, first principles calculations were carried out in cooperation with Dr. Yuefeng Yin and Prof. Nikhil V. Medhekar at Monash University in Australia. First, band structures of CMG were calculated as shown in Fig. 7-8(a) (majority spin of unstrained CMG) and 7-8(b) (majority spin of strained CMG). Red and blue dots in band structures correspond to positive and negative Berry curvature hot spots originating from Weyl points. A positive Berry curvature hot spot exists along [110] line in unstrained CMG as shown in Fig. 7-8(c). On the other hand, when strain was introduced, Berry curvature hot spots were distributed along [100] and [111] lines. This anisotropic distribution of the Berry curvature modulated by the external strain might cause anisotropic SI-SOT in CMG. Next, SHC was calculated. Normally, SHC is calculated by integrating Berry curvature of all the Brillouin zone based on Kubo formula [93]. In this case, one identical value is obtained irrespective of the applied electric-current direction because the Kubo formula is based on assumption that electron's state is in thermal equilibrium. To visualize anisotropic SHC, Berry curvatures were integrated only along the specific axis. Figures 7-8(c) and 7-8(d) show SHC, σ_s, calculated by integrating Berry curvatures along CMG [100] axis with and without strain, respectively. Here, strain is introduced simply by changing the in-plane lattice constant to the value of $\sqrt{2}a_{MgO}$ with keeping the volume of a unit cell. Red and blue lines are SHC of up and down spin, respectively. When we focus around the Fermi level within the energy of room temperature, *i.e.*, $|E - E_F| < kT \sim 25$ meV, contribution of up spin is significantly enhanced by introducing strain, meaning that $\theta_{FM}(0)\beta_0$ is dominant and

ξ_{DL} becomes negative according to Eq. (7-8). On the other hand, when σ_s is calculated by integrating Berry curvatures along [110] line, σ_s is significantly suppressed by introducing strain, meaning that $\theta_{FM}(t)\beta_t$ is dominant and ξ_{DL} becomes positive. Indeed, sign of ξ_{DL} well corresponds to the experimental value in both cases. Therefore, the author concluded that the anisotropy originates from anisotropic distribution of Weyl points and its strong modulation caused by small external strain.

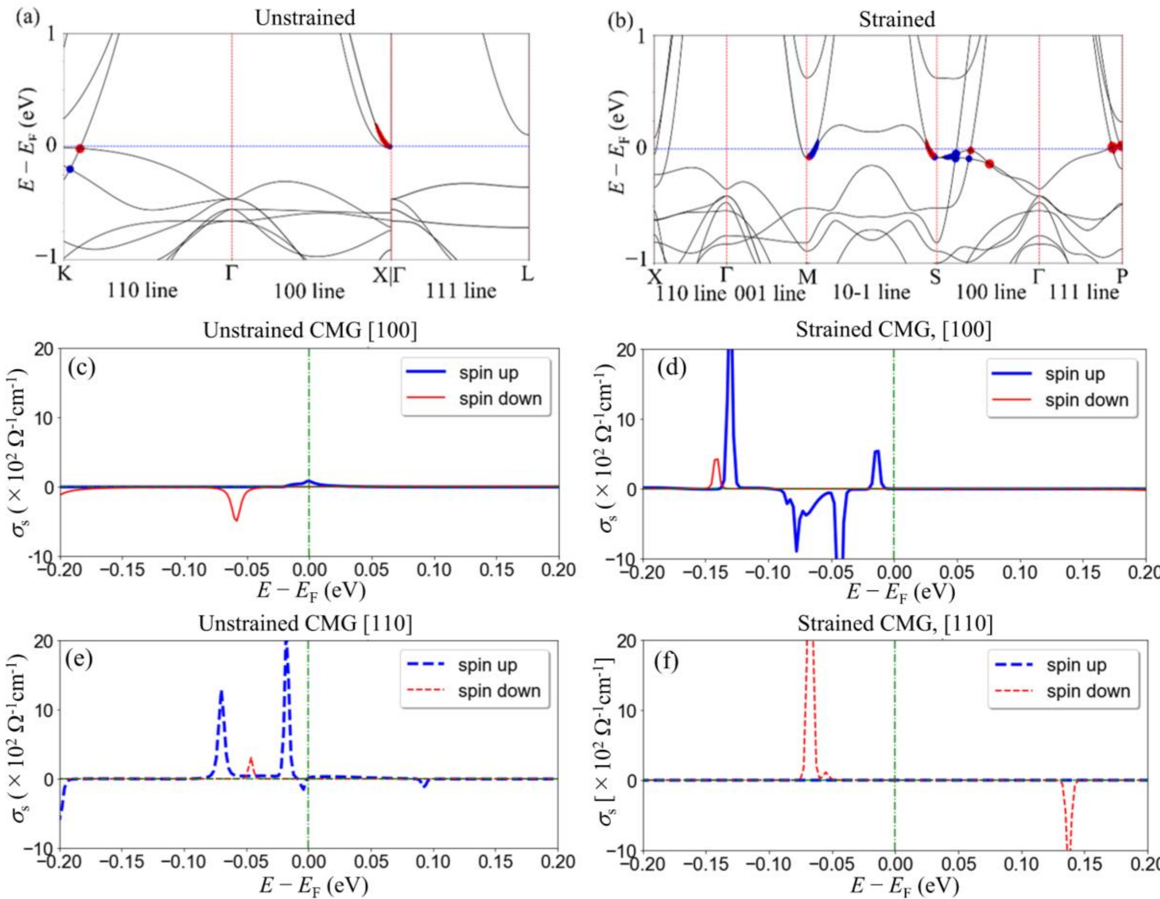

FIG. 7-8. (a) Band structure of unstrained and (b) strained CMG for majority spin band. Red and blue dots indicate positive and negative Berry curvature hot spots. (c) [(e)] SHC of unstrained and (c) [(e)] strained CMG calculated by integrating Berry curvatures along [100] ([110]) line.

7.7.2 Consistency with previous works

In this section, the author discusses consistency in the sign of the SHC observed in this study by comparing with previous works. In the geometry used in this study, positive ξ_{DL} correspond to positive (negative) spin-current injection from the bottom (top) interface. Given the fact that sign of ξ_{DL}, which corresponds to sign of $\theta_{SH}(0)$ [$-\theta_{SH}(t)$], is negative (positive) when current was applied along [100] ([110]) direction, expected sign of θ_{SH} is negative. Leiva, Shiraishi *et al*. reported $\theta_{SAH} + \theta_{SH} = -0.19$ by using a spin valve method [59], where θ_{SAH} is the spin anomalous Hall angle [66]. Isshiki *et al*. reported $\theta_{SAH} + \theta_{SH} = -0.09$ by carefully subtracting thermal contribution [94]. Tang *et al*. reported that θ_{SH} is larger compared to θ_{SAH} by the SHH measurement in CMG/Ti/CoFeB multilayer [95]. All these works support the negative sign of θ_{SH} estimated from the experiment

of this study.

7.7.3 Comparison with spin-orbit torque anisotropy of other materials

Next, the author compares the anisotropy of the SI-SOT in CMG with that in other systems reported so far. As discussed in Section 7.2.2, anisotropy of the SHC is small in a high-symmetric materials, in principle. For instance, anisotropy of the SHC, $|\Delta\sigma_s|$, of fcc Pt is small [96], whereas those of low-symmetric materials such as hexagonal Mn_3Sn [97] and orthorhombic $SrIrO_3$ [98] are large as shown in Table 7-1. In this study, anisotropy of SOT, $|\Delta\sigma\xi_{DL}|$, was calculated to be 1.4×10^5 $(\Omega \cdot m)^{-1}$. Given that $|\Delta\sigma_s|$ takes maximum value of $|\Delta\sigma\xi_{DL}|$, anisotropy of SOT in CMG is significantly large compared to any other materials reported so far, despite of its high-symmetric crystal structure. These results indicate that large anisotropy in SOT can be achieved even in a high-symmetric materials if distribution of Berry curvature hot spots is anisotropic and is modulated by small external strain. Since the strain can easily be controlled by changing deposition condition and/or changing substrate, these findings are applicable to wide variety of systems and could be a mechanism for introducing anisotropic SOT.

Table 7-1. Comparison of anisotropy of SOT in different materials.

	Pt [96]	Mn_3Ga [97]	$SrIrO_3$ [98]	CMG (This work)
Crystal structure	fcc	Hexagonal	Orthorhombic	$L2_1$
$|\Delta\sigma\xi_{DL}|$ $[\times 10^4\ (\Omega \cdot m)^{-1}]$	1.5	< 6.0	4.0	14

7.8 Summary

The author investigated self-induced spin-orbit torque in a single Co_2MnGa layer without any adjacent metal layer. As a result, self-induced spin-orbit torque was found to be as large as the spin-orbit torque in heavy metal/ferromagnet bilayer structures. Moreover, sign and magnitude of self-induced spin-orbit torque were strongly dependent on the applied-current direction with respect to the crystal axis. Experiments on Co_2MnGa films with different thicknesses and with different capping materials, as well as structural analysis and first principles calculations revealed that anisotropy originates from the distribution of Weyl points and its modulation caused by slight strain owing to the lattice mismatch between MgO substrate. This work will contribute to the development of novel spin-orbit torque devices with flexible spin-orbit torque generation controlled by applied current direction, as well as to the understanding of physics in topological materials.

Chapter 8. Conclusion

In this chapter, the author summarizes the result and discussions of the research. The author established a way for detecting spin-orbit torque switching of in-plane ferromagnet by using the spin-rectification effect, named as the low-frequency spin-torque ferromagnetic resonance. As following, the author found that the spin-dependent unidirectional spin Hall magnetoresistance, which is caused by the spin Hall effect and spin-dependent electron mobility in ferromagnet, coexists with the spin-torque ferromagnetic resonance spectrum as the background signal. Using these methods, the author demonstrated ultrafast magnetization switching of a ferromagnet with in-plane magnetic anisotropy. The author also investigated the self-induced spin-orbit torque in ferromagnet/nonmagnet bilayer structures and in a single Co_2MnGa layer without any adjacent metal layer, both of which will pave a way for material search for novel and efficient spin-orbit torque devices.

The author summarizes conclusions of this dissertation as below:

Detection of spin-orbit torque magnetization switching by low-frequency spin-torque ferromagnetic resonance (Chap. 2)

- Enhancement of the non-resonant spin-rectification effect as decreasing microwave frequency was observed.
- Magnetization switching of permalloy due to the spin Hall effect in Pt was detected using the hysteresis characteristics of the enhanced non-resonant spin-rectification effect (low-frequency spin-torque ferromagnetic resonance).
- This method is applicable to a permalloy electrode as small as 100 nm owing to its high sensitivity.

Coexistence of the low-frequency spin-torque ferromagnetic resonance and unidirectional spin Hall magnetoresistance (Chap. 3)

- Offset signal with a polarity depending on the magnetic field in the measurement of the spin-rectification effect (called the background signal) was found to originate from the spin-dependent unidirectional spin Hall magnetoresistance.
- Spin Hall angle of Pt and Ta were estimated to be 0.052 and −0.084, respectively, from the value of the background signal.
- Spin-orbit torque switching of Co using the spin Hall effect in W was detected using the background signal.

Ultrafast spin-orbit torque magnetization switching using two current pulses (Chap. 4)

- Both writing speed and power consumption of the spin-orbit torque switching of an in-plane ferromagnet were improved by more than an order of magnitude by applying two current pulses.
- Magnetization orientation was controlled along any direction by controlling injected spin polarization, which can be used for neuromorphic computing.

Current-induced out-of-plane torque in a single permalloy layer controlled by electrode structure (Chap. 5)

- Current-induced out-of-plane damping-like torque was observed in a single permalloy layer connected to asymmetric electrodes.
- Origin of the out-of-plane damping-like torque was found to be non-uniform electric current and resulting out-of-plane inductive field.
- Field-free switching of an out-of-plane ferromagnet was simulated by using both the in-plane spin injection and out-of-plane inductive field.

Self-induced spin-orbit torque in nonmagnetic material/ferromagnetic material bilayer structures (Chap. 6)

- Anomalous sign reversal of the torque acting on the magnetization of Co was observed in Ta/Co bilayer structure, origin of which was found to be competition between the conventional spin-orbit torque and the self-induced spin-orbit torque.
- Calculation using spin diffusion model indicated that careful consideration of the self-induced spin-orbit torque is needed when estimating the spin Hall angle of the low-conductive material otherwise leading to a serious misestimation.

Observation of giant self-induced spin-orbit torque and its anisotropy in $L2_1$ ordered Co_2MnGa single layer (Chap. 7)

- Giant self-induced spin-orbit torque was observed in a Co_2MnGa film without any adjacent metal layer.
- Sign reversal and change of magnitude in the self-induced spin-orbit torque were observed when applied-current direction with respect to the crystal axis was changed by 45 degrees.
- Large self-induced spin-orbit torque and its anisotropy can be explained by the distribution of the Berry curvature originating from Weyl points and its modulation by external strain.

Appendix

A. Details of the simulation of MuMax3 (Section 2.5.3)

The micromagnetic simulations were performed using the MuMax3 package providing GPU-accelerated calculation of magnetization dynamics. The motion of the magnetic moment was simulated in a 500 nm × 2 μm × 4 nm rectangular geometry. The size of the unit cell was 31 nm × 31 mm × 2 nm. In the simulation in Section 2.5.3, magnetic moment of each cell was initialized along (0.1, 1, 0) direction, which is intentionally tilted from *y* direction to make domain-wall state at the most stable. Then, AC magnetic field with a frequency of *f* was applied along *y* direction. Here, evolution of the amplitude of the AC magnetic field was proportional to $1 - \exp(-t/t_{step})$ with $t_{step} = 0.04 / f$ to excite uniform magnetization oscillation.

B. Frequency dependent power loss (Section 3.4.2)

Power loss of microwave within the cable was estimated from the S_{11} parameter measured by using vector network analyzer (KEYSHIGHT E5071C). Given that S_{11} parameter is the indicative of the power loss during a round trip between the source and the device, power loss within the cable corresponds to the square root of the S_{11} parameter. Figure A1 shows power of microwave applied into the device after transported in the cable normalized by the value of original microwave power, P_{in} / P_s, as a function of *f*. Microwave current, I_{rf}, was calculated using,

$$I_{rf} = \frac{2}{Z + R_0}\sqrt{2ZP_{in}}, \tag{A-1}$$

where Z and R_0 are the characteristic impedance of the cable (50 Ω) and the resistance of the channel, respectively.

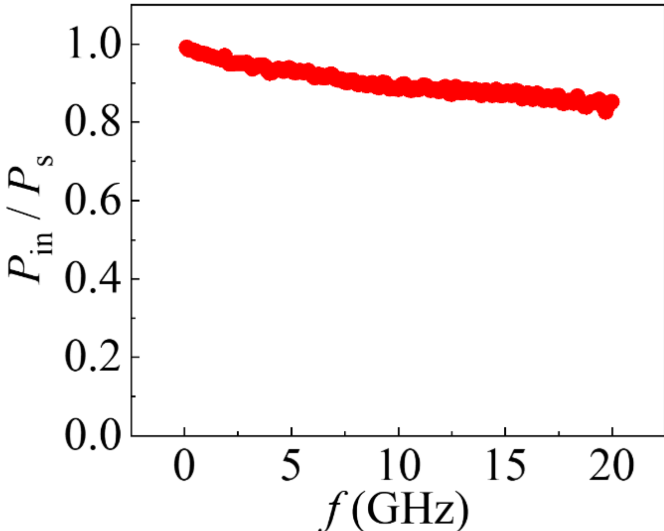

FIG. A1. P_{in} / P_s as a function of *f* in the measurement setup for detecting the BG signal.

C. Estimation of inductive effect with different frequencies (Section 5.5)

Inductive effect becomes less significant as the size of the metal layer becomes smaller because of the skin effect. For a rectangular-shaped FM film, real and complex part of magnetic permeability, μ and μ', respectively, for out-of-plane magnetic field are expressed as,

$$\mu = \frac{1}{\theta}\left(\frac{\sinh\theta + \sin\theta}{\cosh\theta + \cos\theta}\right)\mu_{\mathrm{DC}}\mu_0, \tag{A-2}$$

$$\mu' = \frac{1}{\theta}\left(\frac{\sinh\theta - \sin\theta}{\cosh\theta + \cos\theta}\right)\mu_{\mathrm{DC}}\mu_0, \tag{A-3}$$

$$\theta^2 = 4\pi^2 f^2 \sigma \mu_{\mathrm{DC}}\mu_0 w^2 = \left(\frac{2w}{\delta}\right)^2, \tag{A-4}$$

where μ_{DC} is the relative permeability in the DC limit, σ is the conductivity, and δ is the skin depth. μ_{DC} of the FM is typically 10^2 ~ 10^6 [62]. However, the author concluded that μ_{DC} needs to be set to be 1 because the magnetization just before generating $B_{\mathrm{induc.}}$ is kept along IP direction, which increases the minimum size for application of the OOP inductive torque. Figures A2(b) and A2(c) show μ and μ' calculated using Eq. (A-2)-(A-4) as a function of channel width, w. For simplicity, channel length, l, was set to be infinity. σ was set to be 1.0×10^6 $(\Omega \cdot \mathrm{m})^{-1}$. A dashed line in Fig. A2(c) indicates the value of μ' for realizing $B_{\mathrm{induc.}}$ with application of typical current density for SOT switching using a FM with OOP magnetic anisotropy. The minimum value of w was estimated to be 400 nm for the fall time of pulse current of 100 ps. This value is rather large compared to the device size of a practical MTJ, however, this issue can be solved by a device structure with a metal-layer insertion as shown in Fig. 5-10.

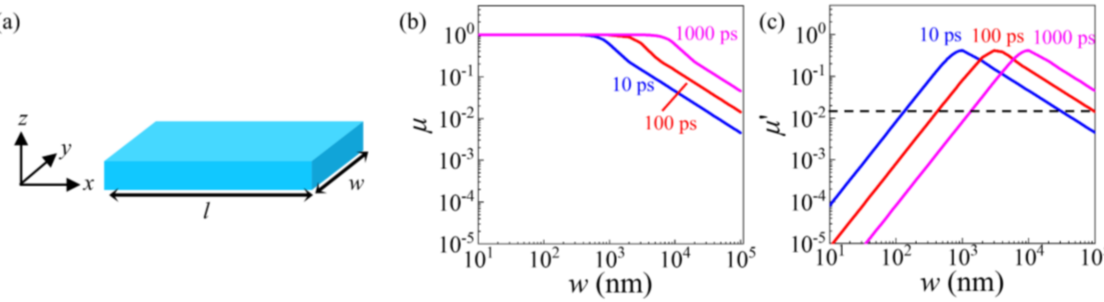

FIG. A2. (a) A schematic of the model used in the calculation. (b) μ and (c) μ' as a function of w with different fall time of pulse current.

D. Influence of the spin pumping and anomalous Nernst effect (Section 6.4.1)

SP-ISHE is known to coexist with the ST-FMR signal and might explain sign reversal of the symmetric component of the ST-FMR spectra in Ta/Co bilayer structure [99,100]. Therefore, the author estimated the influence of the SP-ISHE. Figure A3(a) shows $\mu_0 M_{\mathrm{eff}}$ as a function of $1/t_{\mathrm{FM}}$ for Ta (5 nm)/Co (t_{FM} nm) devices obtained from the Kittel equation [11]. Using interface perpendicular magnetic anisotropy energy, K_{s}, $\mu_0 M_{\mathrm{eff}}$ is expressed as [101],

$$\mu_0 M_{\mathrm{eff}} = \mu_0 M_{\mathrm{s}} - \frac{2K_{\mathrm{s}}}{M_{\mathrm{s}}}\frac{1}{t_{\mathrm{FM}}}. \tag{A-5}$$

From the fitting using Eq. (A-5), $\mu_0 M_s$ of Co was estimated to be 1.87 T. Figure A3(b) shows α as a function of $1 / t_{FM}$ obtained from the frequency dependence of Γ. Considering that two-magnon scattering is very small in Ta/Co bilayer [102,103], only the spin pumping and interfacial spin flipping contribute to the enhancement of α as [104],

$$\alpha = \alpha_{\mathrm{int}} + g_{\mathrm{eff}}^{\uparrow\downarrow}\frac{g\mu_{\mathrm{B}}}{4\pi M_{\mathrm{s}}}\frac{1}{t_{\mathrm{FM}}}, \tag{A-6}$$

where α_{int}, $g_{\mathrm{eff}}^{\uparrow\downarrow}$, g, and μ_B are the intrinsic damping coefficient, effective mixing conductance, the g factor, and Bohr magneton, respectively. From the fitting using Eq. (A-6), α_{int} of Ta/Co system was estimated to be 0.0055. Next, the author measured NM thickness dependence of α to estimate the spin mixing conductance due to spin pumping effect. Figure A3(c) shows α as a function of t_{NM} for Ta (t_{NM})/Co (5 nm) devices. t_{NM} dependence of α is expressed as [105],

$$\alpha = \alpha_{\mathrm{int}} + g_{\mathrm{Ta}}^{\uparrow\downarrow}\frac{g\mu_{\mathrm{B}}}{4\pi M_{\mathrm{s}}}\frac{1}{t_{\mathrm{FM}}}\left(1 - e^{-\frac{2t_{\mathrm{NM}}}{l_{\mathrm{NM}}}}\right), \tag{A-7}$$

where $g_{\mathrm{Ta}}^{\uparrow\downarrow}$ is the spin mixing conductance due to the spin pumping into Ta and l_{NM} ~ 1.8 nm [106] is the spin diffusion length of Ta. From the fitting using Eq. (A-7), $g_{\mathrm{Ta}}^{\uparrow\downarrow}$ was estimated to be 1.7×10^{-19} m^{-2}. Finally, the author estimated the voltage induced by the SP-ISHE, V_{SP}, using [100],

$$V_{\mathrm{SP}} = \frac{Le\theta_{\mathrm{NM}} g_{\mathrm{Ta}}^{\uparrow\downarrow} l_{\mathrm{NM}}}{2\pi(t_{\mathrm{NM}}\sigma_{\mathrm{NM}} + t_{\mathrm{FM}}\sigma_{\mathrm{FM}})}\tanh\left(\frac{t_{\mathrm{NM}}}{2l_{\mathrm{NM}}}\right)\frac{(\tau_{\mathrm{DL}}^0)^2\omega_1 + (\tau_{\mathrm{FL}}^0 + \tau_{\mathrm{Oe}}^0)^2\omega_2}{\alpha^2(\omega^+)^2}, \tag{A-8}$$

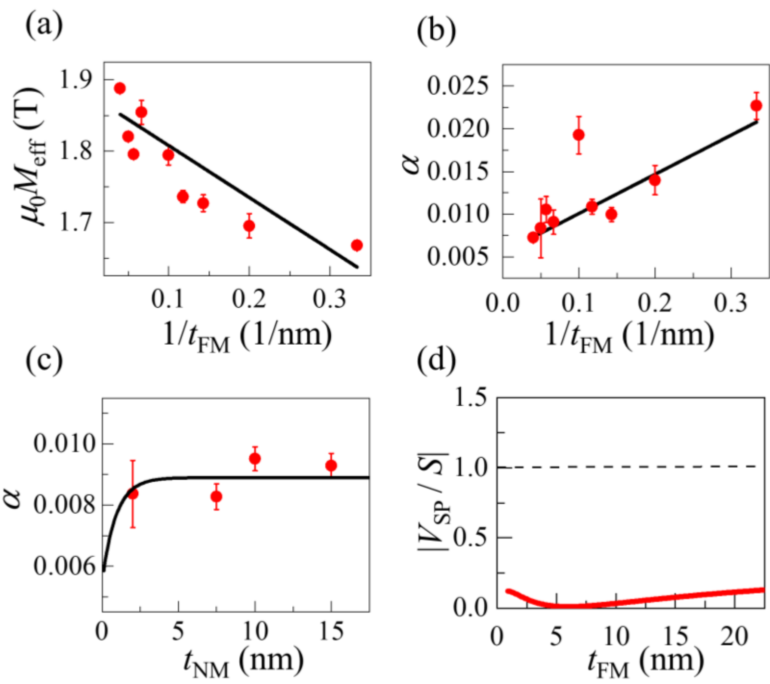

FIG. A3. (a) $\mu_0 M_{\mathrm{eff}}$ as a function of t_{FM}, a as a function of $1/t_{FM}$, (b) a as a function of $1/t_{FM}$, and (c) α as a function t_{NM} measured from Ta (t_{NM})/Co (t_{FM}) devices. (d) $|V_{SP} / S|$ estimated from Eq. (A-8), Eq. (A-9), and Eq. (6-1) when the SI-SOT is neglected, *i.e.*, $\theta_{FM} = 0$.

where L, e, and $\sigma_{NM(FM)}$ are the channel length, the elementary charge, and conductivity of the NM(FM) layer. $\tau^0_{DL(FL)} = \xi_{DL(FL)}\mu_B J_{c(NM)}/eM_s t_{FM}$ and $\tau^0_{Oe} = \gamma\mu_0 J_{c(NM)} t_{FM}/2$, where γ is the gyromagnetic ratio. ω_1, ω_2, and ω_+ are expressed as $\omega_1 = \mu_0\gamma H_0$, $\omega_2 = \mu_0\gamma(H_0 + M_{eff})$, and $\omega_+ = \omega_1 + \omega_2$ using ferromagnetic the resonance field, H_0. On the other hand, S in the ST-FMR spectrum is numerically expressed as [100],

$$S = \frac{I_{rf}R_{AMR}}{2\alpha\omega^+}\tau^0_{DL}, \tag{A-9}$$

where R_{AMR} is the amplitude of the AMR ratio defined as $R = R_0 + R_{AMR}\sin 2\theta$. Figure A3(d) shows $|V_{SP}/S|$ as a function of t_{FM} for the Ta/Co bilayer structure used in Chap. 6 calculated using Eq. (A-8), Eq. (A-9), and Eq. (6-1) when the SI-SOT is neglected, *i.e.*, $\theta_{FM} = 0$. In the calculation, measured values of Co AMR ratio = 0.5 %, $\sigma_{NM} = 4.3 \times 10^5$ $(\Omega \cdot m)^{-1}$, and $\sigma_{FM} = 1.0 \times 10^6$ $(\Omega \cdot m)^{-1}$ were used. The fixed parameters were $l_{NM} = 1.8$ nm, $l_{FM} = 3$ nm, $\theta_{NM} = -0.15$, and $\xi_{FL} / \xi_{DL} = 1$. At all thickness ranges, $|V_{SP}/S|$ was much smaller than 1, meaning that SP-ISHE cannot explain the sign inversion of the ST-FMR signal.

Not only SP-ISHE but also ANE and resonance heating is known to generate symmetric Lorentzian signal in the ST-FMR measurement. However, sign of symmetric component generated by the ANE should be negative (see Section 3.4.3), which cannot explain the sign reversal of the ST-FMR from negative to positive.

E. Measurement of the shift of the magnetoresistance curve (Section 6.4.2)

Figure A4(a) shows enlarged MR curves measured with different polarity of DC electric current, I_{DC}, for Ta(5 nm)/Co(3 nm) device. Dotted lines are MR curves measured with a DC electric current, $I_{DC} = -6$ mA, and solid lines are that with $I_{DC} = +6$ mA. Red curves were obtained when H_{ext} was swept from higher to lower (down sweep), whereas black ones were obtained when swept from lower to higher (up sweep). Peak positions of the MR curves, $\mu_0 H_{sw}$, were shifted with respect to the polarity of I_{DC}, indicating that magnetization in Co feels effective magnetic field generated by I_{DC}. Figure A4(b) shows $\mu_0 H_{sw}$ as a function of I_{DC} for Ta (5 nm)/Co (3 nm) bilayer. Effective magnetic field generated by I_{DC} can be estimated from the slope of this plot, however, contribution of Oersted field, H_{Oe}, needs to be excluded to estimate the spin-orbit effective field, H_{SO}. Therefore, the author subtracted contribution of Oersted field as shown in Fig. A4(c), where $\mu_0(H_{sw} - H_{Oe})$ is plotted as a function of I_{DC}. H_{Oe} was calculated using $H_{Oe} = \frac{j_{NM}t_{NM}}{2}$. From the slope shown in Fig. A4(c), H_{SO} and ξ_{FL} were calculated. Figures A4(d) and A4(e) show torque efficiencies before and after subtracting Oersted field for Ta/Co bilayers with different t_{FM}. ξ_{FL} was negative when Co layer was thin, however, it became close to zero and polarity changes around $t_{FM} \sim 10$ nm. Given that the FL-SOT is proportional to $\boldsymbol{\sigma} \times \boldsymbol{M}$, sign reversal of the FL-SOT is consistent with the sign reversal of spin polarization injected into the FM layer due to the competition between SHEs in Ta and Co.

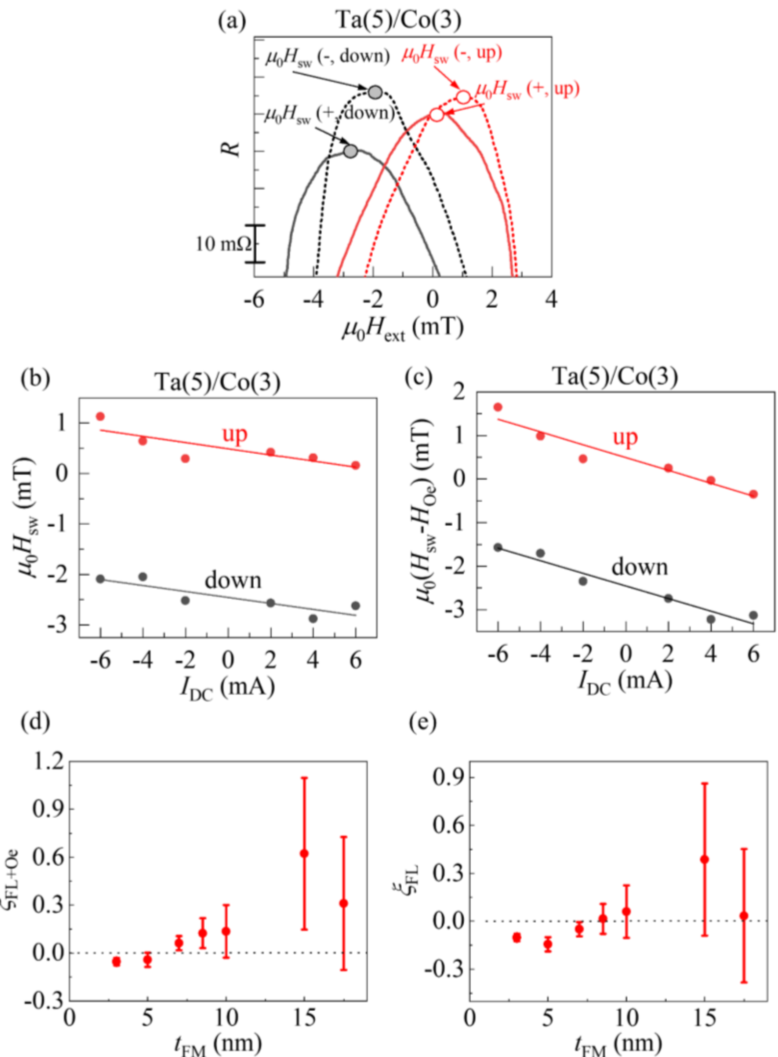

FIG. A4. (a) MR curve of Ta(5)/Co(3) device with $I_{DC} = \pm$ 6 mA. (b) $\mu_0 H_{sw}$ and (c) $\mu_0(H_{sw} - H_{Oe})$ as a function of I_{DC} for Ta(5)/Co(3), where slopes of the fitting are proportional to H_{SO} + H_{Oe} and H_{SO}, respectively. (e) ξ_{FL+Oe} and (f) ξ_{FL} as a function of t_{FM} for Ta(5)/Co(t_{FM}) bilayers.

F. Calculation using spin-diffusion equation (Section 6.5)

To calculate Eq. (6-1), the author used spin diffusion equation (see Fig. A5 for a schematic of the model for calculation). Here, spin current with a spin polarization perpendicular to the magnetization is considered because spin parallel to the magnetization does not give SOT. Therefore, in this experiment, up and down spins are not needed to be separated. In the FM layer, spin current, J_s, and spin chemical potential, μ_s, are assumed as,

$$J_s(z) = \frac{1}{el_{FM}}\left(-Ae^{-\frac{z}{l_{FM}}} + Be^{\frac{z}{l_{FM}}}\right) + J_{sFM(0)}, \tag{A10}$$

$$\mu_s(z) = A\sigma_{FM}^{-1}e^{-\frac{z}{l_{FM}}} + B\sigma_{FM}^{-1}e^{\frac{z}{l_{FM}}}. \tag{A11}$$

In the NM layer, J_s and μ_s are assumed as,

$$J_s(z) = \frac{1}{el_{\mathrm{NM}}}\left(-Ce^{-\frac{z}{l_{\mathrm{NM}}}} + De^{\frac{z}{l_{\mathrm{NM}}}}\right) + J_{\mathrm{sNM(0)}}, \tag{A12}$$

$$\mu_s(z) = C\sigma_{\mathrm{NM}}^{-1}e^{-\frac{z}{l_{\mathrm{NM}}}} + D\sigma_{\mathrm{NM}}^{-1}e^{\frac{z}{l_{\mathrm{NM}}}}. \tag{A13}$$

Here, $J_{\mathrm{sFM(0)}}$ and $J_{\mathrm{sNM(0)}}$ are spin currents originally generated by the SHE, *i.e.*, $\theta_{\mathrm{FM}}J_{\mathrm{c(FM)}}$ and $\theta_{\mathrm{NM}}J_{\mathrm{c(NM)}}$, respectively. Continuities of J_s and μ_s are assumed at the NM/FM interface ($z = 0$) as,

$$\frac{1}{el_{\mathrm{FM}}}(-A + B) + J_{\mathrm{sFM(0)}} = \frac{1}{el_{\mathrm{NM}}}(-C + D) + J_{\mathrm{sNM(0)}}, \tag{A14}$$

$$A\sigma_{\mathrm{FM}}^{-1} + B\sigma_{\mathrm{FM}}^{-1} = C\sigma_{\mathrm{NM}}^{-1} + D\sigma_{\mathrm{NM}}^{-1}. \tag{A15}$$

Zero J_s at the top and bottom interfaces ($z = t_{\mathrm{FM}}$ and $-t_{\mathrm{NM}}$) are assumed as,

$$\frac{1}{el_{\mathrm{FM}}}\left(-Ae^{-\frac{t_{\mathrm{F}}}{l_{\mathrm{FM}}}} + Be^{\frac{t_{\mathrm{F}}}{l_{\mathrm{FM}}}}\right) + J_{\mathrm{sFM(0)}} = 0, \tag{A16}$$

$$\frac{1}{el_{\mathrm{NM}}}\left(-Ce^{\frac{t_{\mathrm{N}}}{l_{\mathrm{NM}}}} + De^{-\frac{t_{\mathrm{N}}}{l_{\mathrm{NM}}}}\right) + J_{\mathrm{sNM(0)}} = 0. \tag{A17}$$

By solving Eq. (A14) – Eq. (A17), coefficients A and B are determined to be,

$$A = \frac{el_{\mathrm{NM}}\left(1 - \cosh\left({}^{t_{\mathrm{NM}}}/_{l_{\mathrm{NM}}}\right)\right)e^{-\frac{t_{\mathrm{FM}}}{l_{\mathrm{FM}}}}J_{\mathrm{sNM(0)}} - \frac{\sigma_{\mathrm{NM}}}{\sigma_{\mathrm{FM}}}el_{\mathrm{FM}}\sinh\left({}^{t_{\mathrm{NM}}}/_{l_{\mathrm{NM}}}\right)J_{\mathrm{sFM(0)}}}{\frac{2\sigma_{\mathrm{N}}}{\sigma_{\mathrm{F}}}\cosh\left({}^{t_{\mathrm{F}}}/_{\lambda_{\mathrm{F}}}\right)\sinh\left({}^{t_{\mathrm{N}}}/_{\lambda_{\mathrm{N}}}\right) + \frac{2\lambda_{\mathrm{N}}}{\lambda_{\mathrm{F}}}\cosh\left({}^{t_{\mathrm{N}}}/_{\lambda_{\mathrm{N}}}\right)\sinh\left({}^{t_{\mathrm{F}}}/_{\lambda_{\mathrm{F}}}\right)}e^{\frac{2t_{\mathrm{FM}}}{l_{\mathrm{FM}}}} + el_{\mathrm{FM}}e^{\frac{t_{\mathrm{FM}}}{l_{\mathrm{FM}}}}J_{\mathrm{sFM(0)}}, \tag{A18}$$

$$B = \frac{el_{\mathrm{NM}}\left(1 - \cosh\left({}^{t_{\mathrm{NM}}}/_{l_{\mathrm{NM}}}\right)\right)e^{-\frac{t_{\mathrm{FM}}}{l_{\mathrm{FM}}}}J_{\mathrm{sNM(0)}} - \frac{\sigma_{\mathrm{NM}}}{\sigma_{\mathrm{FM}}}el_{\mathrm{FM}}\sinh\left({}^{t_{\mathrm{NM}}}/_{l_{\mathrm{NM}}}\right)J_{\mathrm{sFM(0)}}}{\frac{2\sigma_{\mathrm{N}}}{\sigma_{\mathrm{F}}}\cosh\left({}^{t_{\mathrm{F}}}/_{\lambda_{\mathrm{F}}}\right)\sinh\left({}^{t_{\mathrm{N}}}/_{\lambda_{\mathrm{N}}}\right) + \frac{2\lambda_{\mathrm{N}}}{\lambda_{\mathrm{F}}}\cosh\left({}^{t_{\mathrm{N}}}/_{\lambda_{\mathrm{N}}}\right)\sinh\left({}^{t_{\mathrm{F}}}/_{\lambda_{\mathrm{F}}}\right)} - el_{\mathrm{NM}}\cosh\left({}^{t_{\mathrm{NM}}}/_{l_{\mathrm{NM}}}\right)\left(e^{\frac{t_{\mathrm{FM}}}{l_{\mathrm{FM}}}} - 1\right). \tag{A19}$$

Substituting Eq. (A18) and Eq. (A19) into Eq. (A10), and $z = 0$, Eq. (6-1) is obtained.

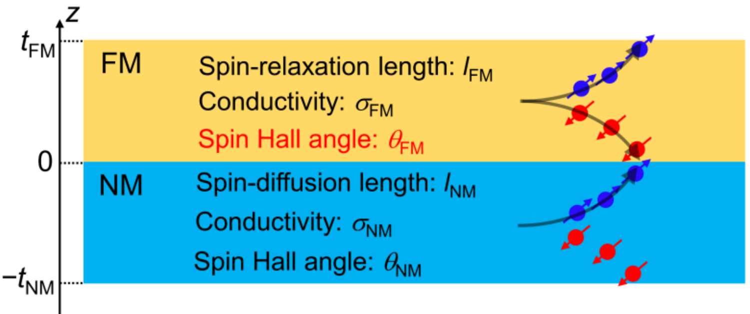

FIG. A5. A schematic of the model for calculation of spin-diffusion equation.

References

[1] G. E. Moore, Electronics **38**, 14 (1965).

[2] 宮崎照宣，土浦宏紀 (2013)，スピントロニクスの基礎　森北出版株式会社.

[3] E. H. Hall, Am. J. Math. **2**, 287 (1879).

[4] J. E. Hirsch, Phys. Rev. Lett. **83**, 1834 (1999).

[5] V. M. Edelstein, Solid State Commun. **73**, 233 (1990).

[6] J. C. Slonczewski, J. Magn. Magn. Mater. **159**, L1 (1996).

[7] Y. Kajiwara, K. Harii, S. Takahashi, J. Ohe, K. Uchida, M. Mizuguchi, H. Umezawa, H. Kawai, K. Ando, K. Takanashi, S. Maekawa, and E. Saitoh, Nature **464**, 262 (2010).

[8] L. Liu, C.-F. Pai, Y. Li, H. W. Tseng, D. C. Ralph, and R. a. Buhrman, Science **336**, 555 (2012).

[9] L. Landau and E. Lifshits, *Phys. Zeitsch. Der Sow.*, **8**, 153 (1935).

[10] T. L. Gilbert, IEEE Trans. Magn. **40**, 3443 (2004).

[11] C. Kittel, Phys. Rev. **73**, 155 (1948).

[12] S. Ikegawa, F. B. Mancoff, J. Janesky, and S. Aggarwal, IEEE Trans. Electron Devices **67**, 1407 (2020).

[13] M. Julliere, Phys. Lett. A **54**, 225 (1975).

[14] K.-S. Lee, S.-W. Lee, B.-C. Min, and K.-J. Lee, Appl. Phys. Lett. **102**, 112410 (2013).

[15] J. Z. Sun, Phys. Rev. B **62**, 570 (2000).

[16] S. Yuasa, K. Hono, G. Hu, and D. C. Worledge, MRS Bull. **43**, 352 (2018).

[17] H. Wu, A. Chen, P. Zhang, H. He, J. Nance, C. Guo, J. Sasaki, T. Shirokura, P. N. Hai, B. Fang, S. A. Razavi, K. Wong, Y. Wen, Y. Ma, G. Yu, G. P. Carman, X. Han, X. Zhang, and K. L. Wang, Nat. Commun. **12**, 6251 (2021).

[18] I. M. Miron, K. Garello, G. Gaudin, P. J. Zermatten, M. V. Costache, S. Auffret, S. Bandiera, B. Rodmacq, A. Schuhl, and P. Gambardella, Nature **476**, 189 (2011).

[19] Y. Wang, D. Zhu, Y. Wu, Y. Yang, J. Yu, R. Ramaswamy, R. Mishra, S. Shi, M. Elyasi, K.-L. Teo, Y. Wu, and H. Yang, Nat. Commun. **8**, 1364 (2017).

[20] L. Zhu, D. C. Ralph, and R. A. Buhrman, Phys. Rev. Appl. **15**, 024059 (2021).

[21] L. Liu, T. Moriyama, D. C. Ralph, and R. A. Buhrman, Phys. Rev. Lett. **106**, 036601 (2011).

[22] J. Sklenar, W. Zhang, M. B. Jungfleisch, H. Saglam, S. Grudichak, W. Jiang, J. E. Pearson, J. B. Ketterson, and A. Hoffmann, Phys. Rev. B **95**, 224431 (2017).

[23] C. O. Avci, K. Garello, M. Gabureac, A. Ghosh, A. Fuhrer, S. F. Alvarado, and P. Gambardella, Phys. Rev. B **90**, 224427 (2014).

[24] A. v. Ettingshausen and W. Nernst, Ann. Der Phys. Und Chemie **265**, 343 (1886).

[25] Y.-T. Liu, T.-Y. Chen, T.-H. Lo, T.-Y. Tsai, S.-Y. Yang, Y.-J. Chang, J.-H. Wei, and C.-F. Pai, Phys. Rev. Appl. **13**, 044032 (2020).

[26] L. Liu, C.-F. Pai, Y. Li, H. W. Tseng, D. C. Ralph, and R. A. Buhrman, Science **336**, 555 (2012).

[27] C.-F. Pai, L. Liu, Y. Li, H. W. Tseng, D. C. Ralph, and R. A. Buhrman, Appl. Phys. Lett. **101**, 122404 (2012).

[28] A. R. Mellnik, J. S. Lee, A. Richardella, J. L. Grab, P. J. Mintun, M. H. Fischer, A. Vaezi, A. Manchon, E. A. Kim, N. Samarth, and D. C. Ralph, Nature **511**, 449 (2014).

[29] N. H. D. Khang, Y. Ueda, and P. N. Hai, Nat. Mater. **17**, 808 (2018).

[30] D. MacNeill, G. M. Stiehl, M. H. D. Guimaraes, R. A. Buhrman, J. Park, and D. C. Ralph, Nat. Phys. **13**, 300 (2017).

[31] I. Shin, W. J. Cho, E. An, S. Park, H. Jeong, S. Jang, W. J. Baek, S. Y. Park, D. Yang, J. H. Seo, G. Kim, M. N. Ali, S. Choi, H. Lee, J. S. Kim, S. D. Kim, and G. Lee, Adv. Mater. **34**, 2101730 (2022).

[32] M. Harder, Y. Gui, and C. M. Hu, Phys. Rep. **661**, 1 (2016).

[33] X. F. Zhu, M. Harder, J. Tayler, A. Wirthmann, B. Zhang, W. Lu, Y. S. Gui, and C.-M. Hu, Phys. Rev. B **83**, 140402 (2011).

[34] A. Vansteenkiste, J. Leliaert, M. Dvornik, M. Helsen, F. Garcia-Sanchez, and B. Van Waeyenberge, AIP Adv. **4**, 107133 (2014).

[35] M. Oogane, T. Wakitani, S. Yakata, R. Yilgin, Y. Ando, A. Sakuma, and T. Miyazaki, Japanese J. Appl. Physics, Part 1 Regul. Pap. Short Notes Rev. Pap. **45**, 3889 (2006).

[36] S. P. Vernon, S. M. Lindsay, and M. B. Stearns, Phys. Rev. B **29**, 4439 (1984).

[37] C. Eyrich, W. Huttema, M. Arora, E. Montoya, F. Rashidi, C. Burrowes, B. Kardasz, E. Girt, B. Heinrich, O. N. Mryasov, M. From, and O. Karis, J. Appl. Phys. **111**, 109 (2012).

[38] M. W. Grinstaff, M. B. Salamon, and K. S. Suslick, Phys. Rev. B **48**, 269 (1993).

[39] S. M. Bhagat, L. L. Hirst, and J. R. Anderson, J. Appl. Phys. **37**, 194 (1966).

[40] A. Yamaguchi, T. Ono, S. Nasu, K. Miyake, K. Mibu, and T. Shinjo, Phys. Rev. Lett. **92**, 077205 (2004).

[41] C. O. Avci, K. Garello, A. Ghosh, M. Gabureac, S. F. Alvarado, and P. Gambardella, Nat. Phys. **11**, 570 (2015).

[42] C. O. Avci, J. Mendil, G. S. D. Beach, and P. Gambardella, Phys. Rev. Lett. **121**, 87207 (2018).

[43] I. V. Borisenko, V. E. Demidov, S. Urazhdin, A. B. Rinkevich, and S. O. Demokritov, Appl. Phys. Lett. **113**, (2018).

[44] K.-D. Lee, D.-J. Kim, H. Yeon Lee, S.-H. Kim, J.-H. Lee, K.-M. Lee, J.-R. Jeong, K.-S. Lee, H.-S. Song, J.-W. Sohn, S.-C. Shin, and B.-G. Park, Sci. Rep. **5**, 10249 (2015).

[45] A. Boehnke, M. Walter, N. Roschewsky, T. Eggebrecht, V. Drewello, K. Rott, M. Münzenberg, A. Thomas, and G. Reiss, Rev. Sci. Instrum. **84**, 063905 (2013).

[46] J. Weischenberg, F. Freimuth, S. Blügel, and Y. Mokrousov, Phys. Rev. B **87**, 060406 (2013).

[47] S. S. L. Zhang and G. Vignale, Phys. Rev. B **94**, 140411 (2016).

[48] J. Bass and W. P. Pratt, J. Phys. Condens. Matter **19**, 183201 (2007).

[49] C. Hahn, G. de Loubens, O. Klein, M. Viret, V. V. Naletov, and J. Ben Youssef, Phys. Rev. B **87**, 174417 (2013).

[50] S. Fukami, T. Anekawa, C. Zhang, and H. Ohno, Nat. Nanotechnol. **11**, 621 (2016).

[51] S. Fukami, T. Anekawa, A. Ohkawara, Chaoliang Zhang, and H. Ohno, Proc. 2016 IEEE Symp. VLSI Technology 1 (2016).

[52] H. Yoda, Y. Ohsawa, Y. Kato, N. Shimomura, M. Shimizu, K. Koi, S. Shirotori, T. Inokuchi, H. Sugiyama, S. Oikawa, B. Altansargai, M. Ishikawa, and A. Kurobe, J. Magn. **24**, 107 (2019).

[53] D. MacNeill, G. M. Stiehl, M. H. D. Guimarães, N. D. Reynolds, R. A. Buhrman, and D. C. Ralph, Phys. Rev. B **96**, 054450 (2017).

[54] L. Liu, C. Zhou, X. Shu, C. Li, T. Zhao, W. Lin, J. Deng, Q. Xie, S. Chen, J. Zhou, R. Guo, H. Wang, J. Yu, S. Shi, P. Yang, S. Pennycook, A. Manchon, and J. Chen, Nat. Nanotechnol. **16**, 277 (2021).

[55] A. Razavi, H. Wu, Q. Shao, C. Fang, B. Dai, K. Wong, X. Han, G. Yu, and K. L. Wang, Nano Lett. **20**, 3703 (2020).

[56] M.-G. Kang, J.-G. Choi, J. Jeong, J. Y. Park, H.-J. Park, T. Kim, T. Lee, K.-J. Kim, K.-W. Kim, J. H. Oh, D. D. Viet, J.-R. Jeong, J. M. Yuk, J. Park, K.-J. Lee, and B.-G. Park, Nat. Commun. **12**, 7111 (2021).

[57] T. Ikebuchi, T. Moriyama, Y. Shiota, and T. Ono, Appl. Phys. Express **11**, 053008 (2018).

[58] Y. Omori, E. Sagasta, Y. Niimi, M. Gradhand, L. E. Hueso, F. Casanova, and Y. Otani, Phys. Rev. B **99**, 014403 (2019).

[59] L. Leiva, S. Granville, Y. Zhang, S. Dushenko, E. Shigematsu, T. Shinjo, R. Ohshima, Y. Ando, and M. Shiraishi, Phys. Rev. B **103**, L041114 (2021).

[60] S. H. C. Baek, V. P. Amin, Y. W. Oh, G. Go, S. J. Lee, G. H. Lee, K. J. Kim, M. D. Stiles, B. G. Park, and K. J. Lee, Nat. Mater. **17**, 509 (2018).

[61] Z. Luo, Q. Zhang, Y. Xu, Y. Yang, X. Zhang, and Y. Wu, Phys. Rev. Appl. **11**, 064021 (2019).

[62] H. D. Arnold and G. W. Elmen, Bell Syst. Tech. J. **2**, 101 (1923).

[63] W. Zhang, W. Han, X. Jiang, S. H. Yang, and S. S. P. Parkin, Nat. Phys. **11**, 496 (2015).

[64] E. Sagasta, Y. Omori, M. Isasa, M. Gradhand, L. E. Hueso, Y. Niimi, Y. Otani, and F. Casanova, Phys. Rev. B **94**, 060412 (2016).

[65] N. Fukumoto, R. Ohshima, M. Aoki, Y. Fuseya, M. Matsushima, E. Shigematsu, T. Shinjo, Y. Ando, S. Sakamoto, M. Shiga, S. Miwa, and M. Shiraishi, Proc. Natl. Acad. Sci. **120**, 2017 (2023).

[66] T. Taniguchi, J. Grollier, and M. D. Stiles, Phys. Rev. Appl. **3**, 044001 (2015).

[67] S. Iihama, T. Taniguchi, K. Yakushiji, A. Fukushima, Y. Shiota, S. Tsunegi, R. Hiramatsu, S. Yuasa, Y. Suzuki, and H. Kubota, Nat. Electron. **1**, 120 (2018).

[68] V. P. Amin, J. Li, M. D. Stiles, and P. M. Haney, Phys. Rev. B **99**, 220405 (2019).

[69] A. Davidson, V. P. Amin, W. S. Aljuaid, P. M. Haney, and X. Fan, Phys. Lett. A **384**, 126228 (2020).

[70] H. Ochoa, R. Zarzuela, and Y. Tserkovnyak, J. Magn. Magn. Mater. **538**, 168262 (2021).

[71] M. Kimata, H. Chen, K. Kondou, S. Sugimoto, P. K. Muduli, M. Ikhlas, Y. Omori, T. Tomita, A. H. MacDonald, S. Nakatsuji, and Y. Otani, Nature **565**, 627 (2019).

[72] K. Kim and K. Lee, Phys. Rev. Lett. **125**, 207205 (2020).

[73] H. Hayashi, A. Musha, H. Sakimura, and K. Ando, Phys. Rev. Res. **3**, 013042 (2021).

[74] C.-F. Pai, Y. Ou, L. H. Vilela-Leão, D. C. Ralph, and R. A. Buhrman, Phys. Rev. B **92**, 064426 (2015).

[75] T. Valet and A. Fert, Phys. Rev. B **48**, 7099 (1993).

[76] E. M. Chudnovsky, Phys. Rev. B **80**, 153105 (2009).

[77] A. Sakai, Y. P. Mizuta, A. A. Nugroho, R. Sihombing, T. Koretsune, M. Suzuki, N. Takemori, R. Ishii, D. Nishio-Hamane, R. Arita, P. Goswami, and S. Nakatsuji, Nat. Phys. **14**, 1119 (2018).

[78] I. Belopolski, K. Manna, D. S. Sanchez, G. Chang, B. Ernst, J. Yin, S. S. Zhang, T. Cochran, N. Shumiya, H. Zheng, B. Singh, G. Bian, D. Multer, M. Litskevich, X. Zhou, S.-M. Huang, B. Wang, T.-R. Chang, S.-Y. Xu, A. Bansil, C. Felser, H. Lin, and M. Z. Hasan, Science **365**, 1278 (2019).

[79] I. Belopolski, G. Chang, T. A. Cochran, Z. J. Cheng, X. P. Yang, C. Hugelmeyer, K. Manna, J. X. Yin, G.

Cheng, D. Multer, M. Litskevich, N. Shumiya, S. S. Zhang, C. Shekhar, N. B. M. Schröter, A. Chikina, C. Polley, B. Thiagarajan, M. Leandersson, J. Adell, S. M. Huang, N. Yao, V. N. Strocov, C. Felser, and M. Z. Hasan, Nature **604**, 647 (2022).

[80] K. Sumida, Y. Sakuraba, K. Masuda, T. Kono, M. Kakoki, K. Goto, W. Zhou, K. Miyamoto, Y. Miura, T. Okuda, and A. Kimura, Commun. Mater. **1**, 89 (2020).

[81] K. Manna, Y. Sun, L. Muechler, J. Kübler, and C. Felser, Nat. Rev. Mater. **3**, 244 (2018).

[82] Y. Zhang, Y. Yin, G. Dubuis, T. Butler, N. V. Medhekar, and S. Granville, Npj Quantum Mater. **6**, 17 (2021).

[83] L. Xu, X. Li, L. Ding, T. Chen, A. Sakai, B. Fauqué, S. Nakatsuji, Z. Zhu, and K. Behnia, Phys. Rev. B **101**, 180404 (2020).

[84] T. Seki, Y. Lau, S. Iihama, and K. Takanashi, Phys. Rev. B **104**, 094430 (2021).

[85] W. Wang, T. Wang, V. P. Amin, Y. Wang, A. Radhakrishnan, A. Davidson, S. R. Allen, T. J. Silva, H. Ohldag, D. Balzar, B. L. Zink, P. M. Haney, J. Q. Xiao, D. G. Cahill, V. O. Lorenz, and X. Fan, Nat. Nanotechnol. **14**, 819 (2019).

[86] L. Zhu, D. C. Ralph, and R. A. Buhrman, Adv. Funct. Mater. **31**, 2103898 (2021).

[87] L. Zhu, X. S. Zhang, D. A. Muller, D. C. Ralph, and R. A. Buhrman, Adv. Funct. Mater. **30**, 2005201 (2020).

[88] Y. Du, R. Thompson, M. Kohda, and J. Nitta, AIP Adv. **11**, 025033 (2021).

[89] P. Swekis, A. S. Sukhanov, Y.-C. Chen, A. Gloskovskii, G. H. Fecher, I. Panagiotopoulos, J. Sichelschmidt, V. Ukleev, A. Devishvili, A. Vorobiev, D. S. Inosov, S. T. B. Goennenwein, C. Felser, and A. Markou, Nanomaterials **11**, 251 (2021).

[90] B. M. Ludbrook, B. J. Ruck, and S. Granville, Appl. Phys. Lett. **110**, 062408 (2017).

[91] S. Emori, T. Nan, A. M. Belkessam, X. Wang, A. D. Matyushov, C. J. Babroski, Y. Gao, H. Lin, and N. X. Sun, Phys. Rev. B **93**, 180402 (2016).

[92] F. Hellman, A. Hoffmann, Y. Tserkovnyak, G. S. D. Beach, E. E. Fullerton, C. Leighton, A. H. MacDonald, D. C. Ralph, D. A. Arena, H. A. Dürr, P. Fischer, J. Grollier, J. P. Heremans, T. Jungwirth, A. V. Kimel, B. Koopmans, I. N. Krivorotov, S. J. May, A. K. Petford-Long, J. M. Rondinelli, N. Samarth, I. K. Schuller, A. N. Slavin, M. D. Stiles, O. Tchernyshyov, A. Thiaville, and B. L. Zink, Rev. Mod. Phys. **89**, 025006 (2017).

[93] R. Kubo, J. Phys. Soc. Japan **12**, 570 (1957).

[94] H. Isshiki, Z. Zhu, H. Mizuno, R. Uesugi, T. Higo, S. Nakatsuji, and Y. Otani, Phys. Rev. Mater. **6**, 084411 (2022).

[95] K. Tang, Z. Wen, Y.-C. Lau, H. Sukegawa, T. Seki, and S. Mitani, Appl. Phys. Lett. **118**, 062402 (2021).

[96] R. Thompson, J. Ryu, G. Choi, S. Karube, M. Kohda, J. Nitta, and B.-G. Park, Phys. Rev. Appl. **15**, 014055 (2021).

[97] Y. Zhang, Y. Sun, H. Yang, J. Železný, S. P. P. Parkin, C. Felser, and B. Yan, Phys. Rev. B **95**, 075128 (2017).

[98] T. Nan, T. J. Anderson, J. Gibbons, K. Hwang, N. Campbell, H. Zhou, Y. Q. Dong, G. Y. Kim, D. F. Shao, T. R. Paudel, N. Reynolds, X. J. Wang, N. X. Sun, E. Y. Tsymbal, S. Y. Choi, M. S. Rzchowski, Y. B. Kim, D. C. Ralph, and C. B. Eom, Proc. Natl. Acad. Sci. U. S. A. **116**, 16186 (2019).

[99] K. Kondou, H. Sukegawa, S. Kasai, S. Mitani, Y. Niimi, and Y. Otani, Appl. Phys. Express **9**, 023002 (2016).

[100] S. Karimeddiny, J. A. Mittelstaedt, R. A. Buhrman, and D. C. Ralph, Phys. Rev. Appl. **14**, 024024 (2020).

[101] V. Tshitoyan, C. Ciccarelli, A. P. Mihai, M. Ali, A. C. Irvine, T. A. Moore, T. Jungwirth, and A. J. Ferguson,

Phys. Rev. B **92**, 214406 (2015).

[102] L. Zhu, L. Zhu, D. C. Ralph, and R. A. Buhrman, Phys. Rev. Appl. **13**, 034038 (2020).

[103] S. Yoshii, K. Kato, E. Shigematsu, R. Ohshima, Y. Ando, K. Usami, and M. Shiraishi, Phys. Rev. B **106**, 174414 (2022).

[104] L. Zhu, D. C. Ralph, and R. A. Buhrman, Phys. Rev. Lett. **123**, 57203 (2019).

[105] J. M. Shaw, H. T. Nembach, and T. J. Silva, Phys. Rev. B **85**, 054412 (2012).

[106] E. Montoya, P. Omelchenko, C. Coutts, N. R. Lee-Hone, R. Hübner, D. Broun, B. Heinrich, and E. Girt, Phys. Rev. B **94**, 054416 (2016).

Publication list

Papers in the peer-reviewed journals

1. M. Aoki, E. Shigematsu, M. Matsushima, R. Ohshima, S. Honda, T. Shinjo, M. Shiraishi, and Y. Ando, "In-plane spin-orbit torque magnetization switching and its detection using the spin rectification effect at subgigahertz frequencies", Physical Review B **102**, 174442 (2020).

2. M. Aoki, E. Shigematsu, M. Matsushima, R. Ohshima, S. Honda, T. Shinjo, M. Shiraishi, and Y. Ando, "Enhancement of low-frequency spin-orbit-torque ferromagnetic resonance signals by frequency tuning observed in Pt/Py, Pt/Co, and Pt/Fe", AIP Advances **11**, 025206 (2021).

3. M. Aoki, E. Shigematsu, R. Ohshima, T. Shinjo, M. Shiraishi, and Y. Ando, "Coexistence of low-frequency spin-torque ferromagnetic resonance and unidirectional spin Hall magnetoresistance", Physical Review B **104**, 094401 (2021).

4. M. Aoki, E. Shigematsu, R. Ohshima, T. Shinjo, M. Shiraishi, and Y. Ando, "Current-induced out-of-plane torques in a single permalloy layer with lateral structural asymmetry", Physical Review B **105**, 144407 (2022).

5. M. Aoki, E. Shigematsu, R. Ohshima, T. Shinjo, M. Shiraishi, and Y. Ando, "Anomalous sign inversion of spin-orbit torque in ferromagnetic/nonmagnetic bilayer systems due to self-induced spin-orbit torque", Physical Review B **106**, 174418 (2022).

6. M. Aoki, Y. Yin, S. Granville, Y. Zhang, N. V. Medhekar, L. Leiva, R. Ohshima, Y. Ando, and M. Shiraishi, "Gigantic anisotropy of self-induced spin-orbit torque in Weyl ferromagnet Co_2MnGa", Nano Letters, accepted.

7. K. Ohnishi, M. Aoki, R. Ohshima, E. Shigematsu, Y. Ando, T. Takenobu, and M. Shiraishi, "All-Electric Spin Device Operation Using the Weyl Semimetal, WTe_2, at Room Temperature", Advanced Electronic Materials **9**, 2200647 (2022).

8. N. Fukumoto, R. Ohshima, M. Aoki, Y. Fuseya, M. Matsushima, E. Shigematsu, T. Shinjo, Y. Ando, S. Sakamoto, M. Shiga, S. Miwa, and M. Shiraishi, "Observation of large spin conversion anisotropy in bismuth", Proceedings of the National Academy of Sciences (PNAS) **120**, e2215030120 (2023).

Abstracts at the international conferences

1. ○M. Aoki, S. Honda, R. Ohshima, Y. Ando, and M. Shiraishi, "Detection of in-plane magnetization switching using ferromagnetic resonance", New Perspective in Spin Conversion Science 2020, 11

(February 3, 2020, Kashiwa, Japan). [Poster]

2. ○M. Aoki, Y. Ando, R. Ohshima, E. Shigematsu, T. Shinjo, and M. Shiraishi, "Detection of in-plane magnetization switching of $Ni_{80}Fe_{20}$ layer by spin rectification effect", 65th Annual Conference on Magnetism and Magnetic Materials, M3-01 (November 5, 2020, Online). [Oral]

3. ○M. Aoki, S. Honda, R. Ohshima, E. Shigematsu, T. Shinjo, M. Shiraishi, and Y. Ando, "Sub-nanosecond magnetization switching induced by spin orbit torque", International Symposium on Creation of Advanced Photonic and Electronic Devices, A7 (March 10, 2021, Online). [Poster]

4. ○M. Aoki, Y. Ando, S. Honda, E. Shigematsu, R. Ohshima, Y. Ando, and M. Shiraishi, "DC voltage generated by the unidirectional spin Hall magnetoresistance in the spin torque ferromagnetic resonance spectrum", 2022 Joint MMM-Intermag Conference, GOH-06 (January 10-14, 2022, Online). [Oral]

5. ○M. Aoki, Y. Ando, R. Ohshima, E. Shigematsu, T. Shinjo, and M. Shiraishi, "Current-induced out-of-plane torque originating from geometry", International Symposium on Creation of Advanced Photonic and Electronic Devices 2022, P-46 (March 8, 2022, Online). [Poster]

6. ○M. Aoki, Y. Ando, R. Ohshima, E. Shigematsu, T. Shinjo, and M. Shiraishi, "Spin-dependent unidirectional spin Hall magnetoresistance detected with spin-torque ferromagnetic resonance", International Colloquium on Magnetic Film and Surfaces, Poster1-38 (July 12, 2022, Okinawa, Japan). [Poster]

7. ○M. Aoki, Y. Ando, R. Ohshima, E. Shigematsu, T. Shinjo, and M. Shiraishi, "Current-induced torque in a single permalloy layer with an asymmetric electrode structure", The 5th International Union of Materials Research Societies International Conference of Young Research on Advanced Materials, 2218 (August 6, 2022, Fukuoka, Japan). [Oral]

8. ○M. Aoki, E. Shigematsu, R. Ohshima, T. Shinjo, M. Shiraishi, and Y. Ando, "Analyzing Self-induced Spin-orbit Torque in a Nonmagnet/Ferromagnet Bilayer Systems", International Symposium on Creation of Advanced Photonic and Electronic Devices 2023, p21 (March 14, 2023, Kyoto, Japan). [Poster]

9. ○M. Aoki, E. Shigematsu, R. Ohshima, T. Shinjo, M. Shiraishi, and Y. Ando, "Observation of chare-to-spin conversion in ferromagnets by means of spin-orbit torque", 8th International Conference on Superconductivity and Magnetism, 436 (May 8, 2023, Fethiye, Turkey). [Oral, **Invited talk**]

10. ○M. Aoki, E. Shigematsu, R. Ohshima, T. Shinjo, M. Shiraishi, and Y. Ando, "Influence of the self-induced spin-orbit torque in spin-orbit torque measurements for nonmagnet/ferromagnet bilayer systems", 11th International Symposium on Metallic Multilayers, 0349 (July 25, 2023, Seoul, Korea). [Poster]

Abstracts at the domestic conferences

1. ○M. Aoki, Y. Aoki, R. Ohshima, T. Shinjo, and M. Shiraishi, "In-plane magnetization switching detected by spin torque ferromagnetic resonance", 第67回応用物理学会春季学術講演会, 14p-A501-2 (2020年3月14日, 上智大学). [Oral]

2. ○M. Aoki, Y. Ando, R. Ohshima, E. Shigematsu, T. Shinjo, and M. Shiraishi, "Measurement of magnetization switching using nonresonant spin rectification effect", 第81回応用物理学会秋季学術講演会, 10a-Z08-9 (2020年9月10日, オンライン開催). [Oral]

3. ○M. Aoki, E. Shigematsu, R. Ohshima, T. Shinjo, M. Shiraishi, and Y. Ando, "Highly sensitive detection of current induced magnetization switching using spin rectification effect", PASPS-25 第25回半導体におけるスピン工学と基礎の応用, 18-前2 (2020年11月18日, オンライン開催). [Poster]

4. ○M. Aoki, S. Honda, R. Ohshima, E. Shigematsu, T. Shinjo, M. Shiraishi, and Y. Ando, "Ultrafast spin orbit torque magnetization switching by using two current pulses", 第68回応用物理学会春季学術講演会, 17p-Z19-10 (2021年3月17日, オンライン開催). [Oral, **英語講演奨励賞**]

5. ○M. Aoki, Y. Ando, S. Honda, R. Ohshima, E. Shigematsu, T. Shinjo, and M. Shiraishi, "Material dependence of the spin rectification effect in nonmagnet/ferromagnet bilayers", 第68回応用物理学会春季学術講演会, 17p-Z19-9 (2021年3月17日, オンライン開催). [Oral]

6. ○M. Aoki, Y. Ando, E. Shigematsu, R. Ohshima, T. Shinjo, and M. Shiraishi, "Spin rectification signal induced by the unidirectional spin Hall magnetoresistance", 第82回応用物理学会秋季学術講演会, 10p-S302-16 (2021年9月10日, オンライン開催). [Oral, **講演奨励賞**]

7. ○M. Aoki, Y. Ando, E. Shigematsu, R. Ohshima, T. Shinjo, and M. Shiraishi, "Origin of the background signal in spin torque ferromagnetic resonance", 第69回応用物理学会春季学術講演会, 26p-E201-1 (2022年3月26日, 青山学院大学相模原キャンパス). [Oral, **Invited talk**]

8. ○M. Aoki, Y. Ando, E. Shigematsu, R. Ohshima, T. Shinjo, and M. Shiraishi, "Curremt-induced out-of-plane torque in a single permalloy layer controlled by geometry", 第69回応用物理学会春季学術講演会, 24p-P01-9 (2022年3月24日, 青山学院大学相模原キャンパス). [Poster]

9. ○青木基, 重松英, 大島諒, 新庄輝也, 白石誠司, 安藤裕一郎, "強磁性体中のスピンホール効果による自己誘起スピン軌道トルク", 「スピントロニクス学術研究基盤と連携ネットワーク」シンポジウム, P35 (2023 年 3 月 20 日, 京都大学宇治キャンパス). [Poster]

10. ◯青木基, 重松英, 大島諒, 新庄輝也, 白石誠司, 安藤裕一郎, “強磁性体/非磁性体 2 層構造における自己誘起スピン軌道トルクの観測”, 日本物理学会 2023 年春季大会, 22aC2-10 (2023 年 3 月 22 日, オンライン開催). [Oral]

11. ◯M. Aoki, E. Shigematsu, R. Ohshima, T. Shinjo, M. Shiraishi, and Y. Ando, “Self-induced spin-orbit torque in metallic bi-layer systems”, 第 84 回応用物理学会秋季学術講演会, in preparation (2023年9月, 熊本城ホール). [Oral]

12. ◯M. Aoki, Y. Yin, S. Granville, Y. Zhang, N. V. Medhekar, L. Leiva, R. Ohshima, Y. Ando, and M. Shiraishi, “Gigantic self-induced spin-orbit torque and its anisotropy in Weyl ferromagnet Co_2MnGa”, 第 84 回応用物理学会秋季学術講演会, in preparation (2023年9 月, 熊本城ホール). [Poster]

13. ◯青木基, 重松英, 大島諒, 新庄輝也, 白石誠司, 安藤裕一郎, “強磁性体中のスピンホール効果による自己誘起スピン軌道トルク”, 第 47 回日本磁気学会学術講演会, in preparation (2023 年 9 月, 大阪大学豊中キャンパス). [Oral]

List of Abbreviations

AHE	Anomalous Hall effect
AMR	Anisotropic magnetoresistance
ANE	Anomalous Nernst effect
BG	Background
CMG	Co_2MnGa
DL-SOT	Damping-like spin-orbit torque
EB	Electron beam
FL-SOT	Field-like spin-orbit torque
FM	Ferromagnetic material
FMR	Ferromagnetic resonance
IP	In-plane
LFST-FMR	Low-frequency spin-torque ferromagnetic resonance
LLG	Landau Lifshitz Gilbert
MOKE	Magneto optical microscope
MR	Magnetoresistance
MRAM	Magnetoresistive random access memory
MTJ	Magnetic tunnel junction
NM	Nonmagnetic material
nr-SRE	Non-resonant spin rectification effect
ONE	Ordinary Nernst effect
OOP	Out-of-plane
PHE	Planar Hall effect
PNE	Planar Nernst effect
REE	Rashba-Edelstein effect
SD-USMR	Spin-dependent unidirectional spin Hall magnetoresistance
SF-USMR	Spin-flip unidirectional spin Hall magnetoresistance
SHA	Spin Hall angle
SHC	Spin Hal conductivity
SHE	Spin Hall effect
SHH	Second harmonic Hall
SI-SOT	Self-induced spin-orbit torque
SOT	Spin-orbit torque
SP-ISHE	Spin pumping and inverse spin Hall effect
SRE	Spin-rectification effect
ST-FMR	Spin-torque ferromagnetic resonance
STT	Spin-transfer torque
TMD	Transition metal dichalcogenide

USMR	Unidirectional spin Hall magnetoresistance
XRD	X-ray diffraction

Acknowledgement

First, I would like to appreciate Prof. M. Shiraishi for providing me opportunity to research in a great environment, as well as giving me plenty of experiences that is needed to be a professional researcher. I was able to learn a lot from him about how a researcher should be. The vice advisors Prof. T. Ono, Assoc. Prof. I. Kakeya, and Assoc. Prof. T. Moriyama gave me priceless advises about not only physics but also about life as a researcher. Prof. Emeritsu T. Shinjo gave me a variety of helpful opinions based on his great experiences as a leading researcher in spintronics.

In the laboratory, first, Assoc. Prof. Y. Ando provided me original concept of my research, taught me a lot about how to proceed research project, and gave me plenty of advises about future career. Assist. Prof. R. Ohshima and Dr. E. Shigematsu discussed with me and helped me about my research in daily life in laboratory. Dr. E. Tamura gave me priceless lectures on basic physics that is difficult for me to learn if by myself. Of course, I would like to appreciate colleagues in the laboratory. Especially, Mr. T. Nishijima and Mr. S. Yoshii, who have spent long time with me until now, made a plenty of discussions and helped me quite a lot to when there was a difficulty in implementing experiment. Dr. M. Matsushima taught me how to carry out experiment in the beginning of my research life. Dr. L. Leiva taught me a lot about fabrication process, discussed with me on science, as well as worked out with me at Nishikyogoku park. Mr. S. Mae carefully revised this manuscript. Owing to him, a number of typos were found and corrected.

From the academic point of view, I would like to appreciate collaborators. Especially, Assoc. Prof. S. Honda helped me by his great micromagnetic simulations, Dr. S. Granville provided me high-quality material and gave me priceless advises on research analysis, and Dr. Y. Yin helped me by his first principles calculations and gave me advises based on his great experience as a theorist.

Next, I would like to appreciate Prof. S. Valenzuela for accepting me as an internship student and giving me an opportunity to research at ICN2 in Barcelona. All the researchers there are so excellent, kindful, and friendly. Especially, I would like to thank Dr. V. Zatko for teaching me everything that is needed for carrying out experiment there and lots of discussions on experimental results.

Of course, I would like to appreciate my parents for giving me a chance to challenge for being a researcher and supporting me financially and emotionally.

Finally, I would like to appreciate Japan Society for the Promotion of Science (JSPS) for accepting me as a JSPS Research Fellowship for Young Scientists and financial support to this study.